Array Decoupling and Self-Interference Reduction Techniques

By

Yuzhang Zang

A dissertation submitted in partial fulfillment of

the requirements for the degree of

Doctor of Philosophy

(Electrical Engineering)

at the

UNIVERSITY OF WISCONSIN-MADISON

2021

Date of final oral examination: 04/01/2021

The dissertation is approved by the following members of the Final Oral Committee:

Nader Behdad, Professor, Electrical and Computer Engineering

John H. Booske, Professor, Electrical and Computer Engineering

Susan C. Hagness, Professor, Electrical and Computer Engineering

Peter T. Timbie, Professor, Physics

Acknowledgements

First of all, I'd like to express my deepest gratitude to my advisor, Professor Nader Behdad, for his endless support, inspiration, and guidance throughout my Ph.D. study. He has always been there, with innovative and exciting research directions, allowing me to explore different ideas and learning from mistakes. I deeply appreciate his patience, tolerance, and trust.

Thanks to my thesis committee members, Professor John H. Booske, Professor Susan C. Hagness, and Professor Peter T. Timbie, for their suggestions, critiques, and helpful discussions in shaping the direction of this dissertation. Professor Daniel van der Weide served on my preliminary examination committee and provided me with valuable feedback that also helped in shaping the direction of this dissertation, I appreciate his time and efforts.

I am fortunate to work with many talented colleagues during my Ph.D. Dr. Hung Luyen guided me in the early stages of my Ph.D studies. He helped me a lot to build the basic skills to do research and write papers. I also thank Dr. Ruyu Ma and Dr. Kai Ren for their valuable advice in my research, career development, and life. I am grateful for the help and support from my fellow graduate students, including Dr. Elham Mohammadi, Dr. Mohammad Ranjbar Nikkhah, Dr. Meng Gao, Nathan D. Strachen, Ruben F. Delgado Castillo, Alex Bouvy, Zongtang Zhang, Jiahao Zhao, Jinkai Wu, and many others.

Apart from my colleagues, I have spent most of my spare time with my sincere friends: Dr. Xuan Wang, Dr. Xuan Zhang, Dr. Yue Gu, Xicheng Xiong, Jinuan Lin, and Chenxi Lyu.

Thanks for their spiritual support that accompanies me overcoming countless difficulties during my Ph.D. study. Besides, I want to express my special thanks to my beloved idol, Chinese actor Ge Hu, who has been accompanied me since I was 12 years old. Thanks for all the films and television works, treasured personal experiences and positive attitudes toward life he has shared with me during the years. Moreover, thanks to the Korean pop stars Donghae Lee and Hyukjae Lee, for their lovely smiles, passionate music and amazing performance. They accompanied me for the last three years of my Ph.D. study with love, hope and joy.

Last but not least, I would like to express my sincere gratitude to my parents Ligang Zang and Yansong Zhang, for their guidance, full support, and love, which has never left and will always be with me. I would also like to acknowledge my grandparents, Jing Yan and Weihai Zhang, who passed away in the year of 2019, before the completion of my education. I know they would be proud of me and I will forever be grateful for the love and values they instilled in me. Without my family's continuous support, constant love and encouragement, none of this would have been possible.

This work relates to Department of Navy award N00014-16-1-2098 issued by the Office of Naval Research and to the National Science Foundation award ECCS-144395. The United States Government has a royalty-free license throughout the world in all copyrightable material contained herein. Any opinions, findings, and conclusions or recommendations expressed in this material are those of the author and do not necessarily reflect the views of the Office of Naval Research or the National Science Foundation.

Contents

List of Figures

List of Tables

Abstract

Antenna arrays with multiple isolated ports are widely used in various wireless applications such as diversity reception, multiple-input multiple output (MIMO) communication, adaptive beamforming, and direction finding. For applications on in which limited platform size is available to accommodate the antenna, restrictions on the available space demand the use of an element spacing significantly smaller than $\lambda/2$. This is particularly the case at at low radio-frequency (RF) and microwave frequency bands (i.e., below 1 GHz) where the wavelength of electromagnetic waves is relatively large. The small element spacing introduces strong mutual coupling between the ports of the compact arrays. The strong coupling can cause significant system performance degradation. Thus, it is highly desirable to develop efficient methods for cancelling the mutual coupling.

In this dissertation, we discuss array decoupling and self-interference reduction techniques that are particularly relevant to low-frequency RF and microwave applications. These include developing simultaneous transmit and receive (STAR) antennas and synthesizing external matching and decoupling networks for multi-element antenna arrays. In Chapter 2, we design a compact, low-profile simultaneous transmit and receive antenna. The proposed STAR antenna architecture consists of a pair of capacitively-coupled, orthogonal half loops as the RX antenna, and a centrally located, top-hat monopole as the TX antenna. This approach involves a high transmit-receive isolation level and an omnidirectional radiation pattern in the azimuth plane. However, the proposed STAR antennas require multi array

elements with restrict symmetry in the alignment and phase shifters, which this technique can not be applied to an antenna array with only one transmit and one receive antenna. Thus, in Chapter 3, we present an analytic technique for synthesizing a decoupling and matching network (DMN) for symmetric two-element antenna arrays. Using this approach, we can determine the S-parameters of the DMN and use them to synthesize its coupling network. Then, this work was extended into designing the decoupling and matching networks for three-element antenna arrays as discussed in Chapter 4. In the previous two chapters, the designed DMNs are for stable antenna systems. However, in a varying environment, the performance cannot be maintained due to the change of the S-parameters of the antenna. Thus, in Chapter 5, a method for designing an adaptive matching and decoupling network (MDN) is proposed. The system can track the variation in the antennas impedances and update the tunable matching network, which can successfully perform the tasks of impedance matching and decoupling of an asymmetric two-element antenna system over a narrow bandwidth.

Chapter 1

Introduction and Background

1.1 Motivation

The rapid penetration of wireless systems has resulted in increased demand for high data rate, low latency systems to provide quality wireless access to the end user. Over the past decade, various techniques have been used to increase the throughput like multiple-input multiple-output (MIMO) and other multi-antenna techniques. Individual radio frequency (RF) signals at multi-antenna ports are decorrelated either by increasing the isolation between two antennas, or by using antennas with dissimilar radiation patterns. This results in spatial diversity and multiplexing, thus improving the channel capacity in MIMO transmission. Antenna arrays with multiple ports can also be used in space-time techniques like diversity reception, adaptive beamforming or nulling and direction finding. However, for a MIMO system with limited space for antennas, the mutual couplings among the antenna elements causes interference and so have serious effect on the performance. The goal of isolation is normally achieved by ensuring a sufficient inter-element spacing of at least $\lambda/2$ in order to inhibit the effects of mutual coupling. However, in the case of size-limited platforms like mobile applications, the required diversity can only be achieved if an element spacing significantly smaller than $\lambda/2$ is utilized. With such small element spacing mutual coupling is not any longer negligible [1, 2].

Moreover, in-band full-duplex (IBFD) transmission is an attractive solution for improving the link throughput and double the wireless capacity by simultaneously transmit and receive (STAR) signals using the same frequency band comparing to time or frequency division duplex systems [3]. In electronic warfare applications, full-duplex transmission techniques offer the possibility of jamming a frequency band, while monitoring it simultaneously. However, the primary challenge for STAR operation in a transceiver is the necessity to greatly reduce the level of self-interference (SI) generated through coupling of the transmitter's signal into the simultaneously active receiver operating at the same RF carrier frequency. To effectively discriminate the receive signals from the self-interference signals, the IBFD system needs to

achieve a high isolation between the transmit (TX) and receive (RX) channels [4, 5].

To achieve this level of isolation, multiple stages of separation and cancellation at the antenna, RF, analog, and digital levels are needed [6]. Toward that end, exploiting antennas capable of providing high isolation levels between the transmit and receive ports is critical as it alleviates the requirements of the subsequent self-interference cancellation stages. Hence, antenna isolation has been given significant attention in recent years due to its impact on decoupling multi-antenna elements. It is necessary and desirable to find techniques, which can reduce the mutual coupling.

Besides, majority of the existing proposed approaches for decoupling techniques are for steady environment. However, for low frequency applications, such as handset antenna system of a mobile device being held with different orientations at different distances from human body, or a vehicle-mounted antenna array experience changes in the surrounding environment during motion. Such changes in operating scenarios may cause substantial variations in the antennas impedance, degrading the impedance matching and detuning the frequency range for sufficient interelement isolation. Therefore, a method that tracks the antenna arrays impedance variation and provides adaptive matching and decoupling for the array elements is highly desirable for these application scenarios.

1.2 Literature Review

1.2.1 Simultaneous Transmit and Receive Antenna

In the antenna domain, several different techniques have been developed to enhance the isolation between the transmit and receive ports. These include spatial duplexing [7-8], polarization diversity [9-17], using a circulator or quasicirculators [18-25], near-field cancellation [26-32], and other hybrid approaches [33-34].

The receiving and transmitting antenna pairs behave orthogonal polarization performance in [9-17]. Under ideal circumstances, no signal will enter into the receiving port due

to the orthogonal polarization and such method has no requirement for antenna physical locations placement. Limitations of the integrated quasicirculators are insertion loss, return loss, low power efficiency, and limited isolation bandwidth. The near-field cancellation approach creates near-field nulls where the RX antenna(s) is placed, when TX signals from the designed phased array combine in space. When there are two array elements, although high isolation can be achieved, the far-field gain patterns of the TX phased array are usually different from the ones of the RX antenna. High isolation and similar radiation patterns can be achieved by using a circular array.

A number of circularly polarized (CP), unidirectional STAR antennas based on the four-arm spiral antenna topology were reported recently [26] [28], [29]. In [26], an antenna system with an eight-element TX monopole array distributed on a ring antenna and a centrally located RX monopole was designed. To decrease the coupling between each TX element and the RX antenna, the authors used a conductive cylinder to elevate the RX antenna. This makes the overall dimensions of the whole antenna system (excluding the ground plane) relatively large. The antenna system in [30] is combined with multiple stages of interference cancellation circuits and utilizes the space between the antennas to acquire the total isolation as much as 60 dB, where the antenna cancellation contributes 30 dB. But this system is complicated and its antennas occupy a large space. The STAR antennas presented in [31] and [32] have high isolation and are broadband or even ultra-wideband. However, these antennas are not low profile. Thus, a STAR antenna with more compacted size and good performance is desirable and proposed in this thesis.

1.2.2 Decoupling Networks for A Multi-element Antenna Array

In recent years, plenty of achievements have been made in reducing mutual coupling, especially between array elements with fairly small spacing. Various methods have been developed for accomplishing this, such as electromagnetic bandgap (EBG) [34-36], defected ground structure (DGS) [37-39], single negative (SNG) metamaterial [40], [41], neutralization line

[42], array-antenna decoupling surface [43], and decoupling network [44-48].

While the metamaterial and EBG structures are generally large in size, the spatial multiplexing method increases the circuit complexity and DC power consumption. Various EBGs were schemed out for the reducing mutual coupling between two-element arrays, but could not be applied to arrays with smaller spacing, as EBGs themselves occupied too much space. In [37], several slits were etched from the ground plane, and then the identical DGS was capable of alleviating mutual coupling between planar inverted-F antennas, monopoles, and patches, which could take effect for smaller separation on account of its resonant characteristic. However, the radiation patterns, in particular, the back radiation, could be execrably deteriorated when introducing DGSs [40-41]. [42-43] employed two types of SNG metamaterials to decouple two-element antenna arrays. Although the similar method could effectively improve isolation between smaller gap, the designing process was rather complex. However, the decoupling network exhibits its superiority in compliable designing principle and flexible element gap.

Various implementations of decoupling networks have been described in the literature [44-49]. In its simplest form, the decoupling network consists of reactive elements connected between neighboring array elements, which effectively cancels the external mutual coupling between them. An alternative approach to achieving port decoupling involves the use of a modal feed network, where isolation between the new input ports is achieved by exploiting the inherent orthogonality of the eigenmodes of the array [50-53]. Besides, there are also some decoupling network techniques using hybrid couplers, multi-layer networks or different coupling stages to decouple multi-element antenna arrays [91-92]. These techniques make the dimension of the system large and increase the complexity.

The previously reported methods are designed with only one solutions and single network topology or for a special application. Thus, in this thesis, we provide an analytic synthesizing method for decoupling network. The proposed procedure provides a system-level solution to precisely determine the element values of decoupling network and identify all

possible lumped-element network implementations, which can also satisfy various conditions for different applications.

1.2.3 Adaptive Matching and Decoupling Networks

At present, the commonly used approaches for tunable matching and decoupling antenna arrays include the followings. Some solutions use tunable electromagnetic band-gap structures or spatial multiplexing of local elements to reconfigure the operating frequency range over which good impedance matching and high isolation is achieved [34, 105-107]. However, due to the lack of impedance sensing and feed-back control system, these techniques can not be applied to provide an adaptive matching and decoupling.

External decoupling networks with tunable components are widely used in different literatures for adaptive matching and decoupling systems [54-58, 109-112]. The simplest method referred to as open loop utilizes a lookup table. While this addresses the multiband issues, it cannot provide accurate match tuning that accounts for component and environmental variation. The closed loop control approach most commonly used minimizes the input reflection or voltage standing-wave ratio (VSWR) of the matching network using a loop configuration [54-57]. The control unit is run iteratively until a best matching solution is achieved with the tuning trajectory controlled by an optimization algorithm. In [58], the adaptive tuning for compensating antenna mismatch based on conjugate match is carried out by using L-networks and associated impedance measurements. However, this adaptive tuner has considerable limitations since an L-network can only achieve a conjugate match over half of the Smith Chart. With finite tuning range, the region for the conjugate solution will be further significantly reduced. In [109-112], these networks consist of multiple electronic devices as switches, bias trees, amplifiers, mixers or diodes, which will increase the complexity of the circuits. Besides, some of the previously reported techniques also limit to symmetric antenna arrays.

Thus, it is desirable to develop an adaptive matching and decoupling networks for a two-

element antenna array, which can analytically determine the element values and with less complicated network topology.

1.3 Proposed Solutions

Chapter 2 presents a compact, low-profile simultaneous transmit and receive (STAR) antenna with monopole-like radiation characteristics. This approach involves a compact, vertically polarized STAR antenna with a high transmit-receive isolation level and an omnidirectional radiation pattern in the azimuth plane. The proposed STAR antenna consists of transmit (TX) and a receive (RX) antennas whose phase centers are collocated. The TX antenna is a monopole with top-hat loading, placed directly below the central point of the crossed loop. The RX antenna consists of a pair of orthogonal half loops, each capacitively fed at its both ends with a 180° phase difference. The four ports of the RX antenna are fed with the same amplitude and relative phase values of 0°, 90°, 180°, 270° to produce an omnidirectional radiation pattern and high isolation with the TX antenna. Simulation and experimental results are presented.

Chapter 3 covers an analytic technique for synthesizing the decoupling and matching network for a symmetric two-element antenna array. We first determine the 4×4 scattering matrix of DMN. Subsequently, we identify 13 different lumped-element networks that can be used to implement the DMN and present an analytic method for determining their element values from the DMNs S-matrix. This work is important because, for the first time, it offers a systematic method for determining all potential implementations of a two-element antenna array and precisely determining the DMNs element values. The detailed design, simulation and experiment results are presented with a good agreement.

Chapter 4 provides an analytic synthesis method for the decoupling network of a three-element antenna arrays. This method investigates a new procedure for analytically synthesizing an decoupling network for both the center-symmetric and the linear three-element an-

tenna array. Using the approach reported in this chapter, we can determine the S-parameters of the DMN that can simultaneously impedance match and decouple the antennas and use them to synthesize the network. The performance of the system was evaluated by both simulations and measurements. Measurement results confirmed the results obtained from simulations and verified the validity of the proposed synthesis technique.

Chapter 5 introduces a method for adaptive matching and decoupling network for a two-element antenna array. The system includes three sub-systems as impedance sensing, tunable matching network and fixed decoupling network. The impedance sensing sub-section can track and measure the antenna array's impedance matrix. The adaptive tuning section is designed to make the system symmetric and make the impedance matrix at the intended operating frequency relatively. A fixed decoupling network was designed using the method reported in Chap 3 to final match and decouple the system to 50 Ω loads. The design procedure, operating principle, simulations and experimental characterization of the system are included.

1.4 Overview of the dissertation

The organization of this dissertation is as follows:

Chapter 2 presents a compact, low-profile, vertically polarized simultaneous transmit and receive (STAR) antenna with monopole-like radiation characteristics. The proposed STAR antenna has a high transmit-receive isolation level and an omnidirectional radiation pattern in the azimuth plane.

Chapter 3 covers an analytic technique for synthesizing a decoupling and matching network for a two-element antenna array. Using this approach, we can determine the S-matrix of the DMN first and use it to synthesize its coupling network.

Chapter 4 provides a new procedure for synthesizing a decoupling and matching network for both center-symmetric and linear three-element antenna arrays. Using the procedure

reported in this chapter, we can determine S-matrix of the DMN that can simultaneously impedance match and decouple the antennas. Subsequently, this S-matrix will be used to synthesize the DMN.

Chapter 5 introduces a solution for designing an adaptive matching and decoupling network for a two-element antenna array. The proposed system can track the variations in the antenna array's impedance and update the network to re-match and re-decouple the antenna array.

Chapter 6, we conclude that the proposed methods are contributing to the array decoupling and self-interference techniques and discuss two possible future works.

Chapter 2

A Compact, Low-Profile Simultaneous Transmit And Receive (STAR) Antenna With Monopole-Like Radiation Characteristics

The full manuscript was published as:

D. Wu, Y. Zang, and H. Luyen, M. Li and N. Behdad, "A Compact, Low-Profile Simultaneous Transmit And Receive (STAR) Antenna With Monopole-Like Radiation Characteristics," *IEEE Antennas Wireless Propag. Lett.*, vol 18 , no 4 , Apr. 2019.

A compact, vertically polarized simultaneous transmit and receive (STAR) antenna with a high transmit-receive isolation level and an omnidirectional radiation pattern in the azimuth plane is presented. The proposed STAR antenna consists of transmit (TX) and a receive (RX) antennas whose phase centers are collocated. The TX antenna is a monopole with top-hat loading, placed directly below the central point of the crossed loop. The RX antenna consists of a pair of orthogonal half loops, each capacitively fed at its both ends with a 180° phase difference. The four ports of the RX antenna are fed with the same amplitude and relative phase values of 0°, 90°, 180°, 270° to produce an omnidirectional radiation pattern and high isolation with the TX antenna. The STAR antenna was designed for operation in the 2.45 GHz ISM band with electrical dimensions of $D \times H = 0.44\lambda \times 0.15\lambda$ (diameter $\times$ height). A prototype of this antenna was fabricated and experimentally characterized. Measurement results show that the antenna has a TX/RX isolation level better than 38 dB and maintains monopole-like patterns for both TX and RX modes over a bandwidth of 300 MHz centered at 2.45 GHz.

2.1 Introduction

In-band full-duplex (IBFD) wireless communication systems have the potential for enhancing the spectrum efficiency of next generation wireless communications systems [59]. For an IBFD system, signals can be transmitted and received simultaneously at the same frequency, hence doubling the spectral efficiency and system capacity [59]. One of the most challenging works in designing an IBFD system is to suppress self-interference (SI) between the transmit and receive chains to a level below the receiver's noise floor [3, 59]. For a typical ISM radio system transmitting at 20 dBm with a receiver noise floor of -90 dBm, an isolation level of more than 110 dB between the transmit (TX) and receive (RX) chains is required [3]. This high isolation can be realized in three different stages: antenna cancellation, RF interference cancellation, and digital baseband interference cancellation [60]. High isolation in antenna

cancellation stage could alleviate the burden of implementing the subsequent RF and digital cancellation stages.

Antenna cancellation for IBFD system can be realized by using spatial duplexing [9], polarization diversity [13, 28, 61-62], resonators placed between the antenna elements for decoupling [63-65], four-arm spiral antenna for ultra-wide band circular polarization [27, 29, 33], and near-field cancellation technique [26, 30, 66]. Among these techniques, the near-field cancellation technique is especially attractive as it allows TX and RX antennas to have not only high isolation but also similar radiation characteristics, especially the polarization and the shape of the radiation patterns along the direction(s) of maximum radiation. In [26], an antenna system with an eight-element TX monopole array distributed on a ring antenna and a centrally located RX monopole was designed for the 2.45 GHz ISM band. To decrease the coupling between each TX element and the RX antenna, the authors used a conductive cylinder with the dimensions of $D \times H = 0.84\lambda \times 0.62\lambda$, where λ is the free-space wavelength at 2.45 GHz, to elevate the RX antenna. This makes the overall dimensions of the whole antenna system (excluding the ground plane) relatively large as $D \times H = 2.68\lambda \times 0.87\lambda$ [66]. In [30], it is shown that the conductive cylinder in this design can be removed to make the antenna more compact with the dimensions of $D \times H = 0.74\lambda_{min} \times 0.25\lambda_{min}$, where λ_{min} is the wavelength at the lowest operating frequency of the antenna.

In this paper, a compact, low-profile, high-isolation simultaneous transmit and receive (STAR) antenna with omnidirectional radiation patterns is presented. The proposed antenna is designed at 2.45 GHz ISM band for the Vehicle-to-Vehicle communications applications [26] as well as military communications applications, which could offer the possibility of jamming a frequency band, while monitoring it simultaneously. Our proposed STAR antenna architecture consists of a pair of capacitively-coupled, orthogonal half loops as the RX antenna, and a centrally located, top-hat monopole as the TX antenna. The TX antenna is directly fed by a 50 Ω SMA connector. Each half loop of the RX antenna is differentially fed at its both ends. The four ports of the RX antenna are connected to a quardrifilar and

excited with the same amplitude and linear progressive phase of 90° to generate a near-field null at the location of the TX antenna. Hence, high isolation between TX and RX antenna can be achieved. Additionally, the horizontal portion of the cross loop is meandered to reduce the height and aperture area of the RX antenna while maintaining vertically-polarized radiation. The proposed STAR antenna is with a compact size of $\pi \times (0.22\lambda)^2 \times 0.15\lambda$. The volume occupied by this antenna is approximately 98.1% smaller than the volume of the STAR antennas operating at ISM band reported in while having the same overall bandwidth [26, 66]. The fabricated prototype exhibits more than 38 dB isolation between the TX and RX ports over the frequency range of 2.4 to 2.7 GHz, which covers the 2.45 GHz ISM band and maintains consistent, monopole-like patterns for both TX and RX modes over the entire band of operation.

2.2 Antenna Design

Fig. 2.1 shows the topology of the proposed STAR antenna that comprises a pair of orthogonal, capacitively-coupled half loops acting as the RX antenna and a top-hat loaded monopole acting as the TX antenna. The TX and RX antennas are mounted on a circular ground plane with a diameter of 123 mm and a thickness of 1.5 mm, as shown in Fig. 2.1(a). Figs. 2.1(b), 2.1(c), and 2.1(d) show the top view of the cross loop, side views of capacitively-coupled feed structure for the RX antenna, and the perspective view of the central TX monopole, respectively. Fig. 2.1(e) shows the layout of the feeding network of the RX antenna and a dashed rectangular box indicating the footprint of a commercial quadrifilar IC (RFMW RQF2500Q06),which is used to excite the four input ports of the RX antenna with equal amplitudes and phases of 0°, 90°, 180°, and 270°. Photographs of the fabricated prototypes of the STAR antenna and the feeding network of the RX antenna are shown in Figs. 2.1(f) and 2.1(g), respectively. The antenna was designed to work in the ISM frequency band. The physical dimensions of the proposed STAR antenna are provided in the caption of Fig. 2.1.

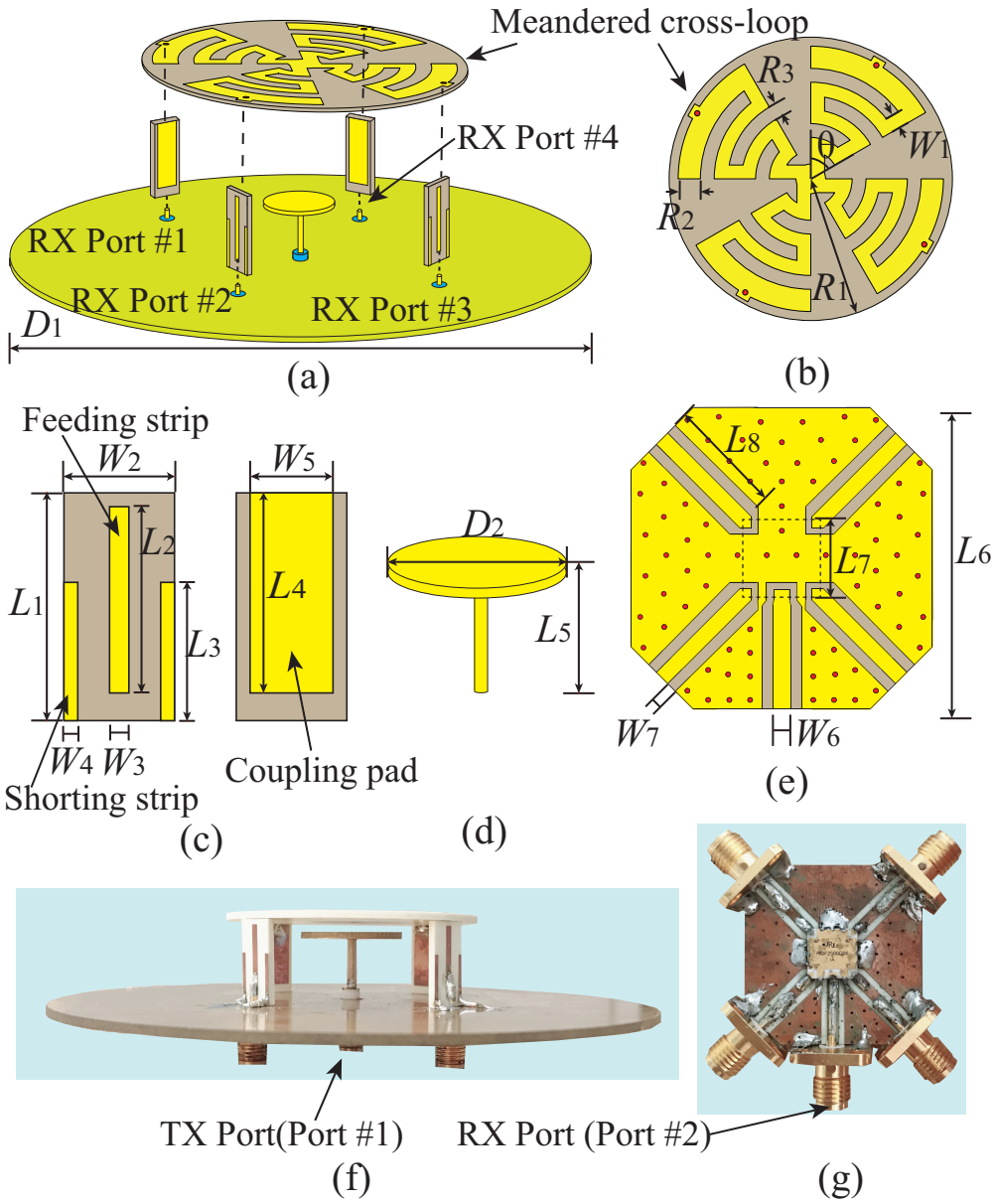

Figure 2.1: Geometry of the proposed STAR antenna. (a) 3-D view. (b) Top view of the horizontal portion of the RX antenna. (c) Vertical portion of the RX antenna. (d) The TX antenna. (e) The layout of the feeding network of the RX antenna. (f) Photograph of the fabricated STAR antenna. (g) Photograph of the fabricated feeding network used to feed the RX antenna. The physical dimensions of the proposed STAR antenna are listed as follows: $D_1 = 123.00$ mm, $R_1 = 26.29$ mm, $R_2 = 4.21$ mm, $R_3 = 2.61$ mm, $W_1 = 2.62$ mm, $\theta = 60°$, $L_1 = 16.48$ mm, $L_2 = 13.48$ mm, $L_3 = 10.00$ mm, $L_4 = 14.48$ mm, $W_2 = 8.00$ mm, $W_3 = 1.40$ mm, $W_4 = 1.00$ mm, $W_5 = 6.00$ mm, $D_2 = 22.00$ mm, $L_5 = 10.93$ mm, $L_6 = 29.00$ mm, $L_7 = 3.00$ mm, $L_8 = 11.38$ mm, $W_4 = 1.75$ mm, and $W_7 = 1.02$ mm.

2.2.1 TX antenna design

The TX antenna is a top-hat loaded monopole located at the center of the ground plane and aligned with the vertical symmetry axis of the RX antenna, as shown in Fig. 2.1(d). The top hat of the TX antenna not only reduces the profile of TX monopole antenna, but also contributes to the coupling path #2 to reduce the mutual coupling between each RX port and TX port, as shown in Fig. 2.2(a). The height of the monopole and diameter of the top hat were optimized in full-wave simulations that take into account the presence of the RX antenna to achieve good impedance matching for the TX antenna over the operating frequency range of $2.4 - 2.5$ GHz. The final dimensions for the diameter of the top hat and height of the monopole are 22 mm and 10.93 mm, respectively.

2.2.2 RX antenna design

The RX antenna consists of two orthogonal loops, as shown in Fig. 2.1(a). The total length of each loop, measured from RX port #1 to #3 or from RX port #2 to #4, is about one wavelength at 2.45 GHz. The four ports of the RX antenna are capacitively fed to make each port well matched to 50 Ω. The geometry of each capacitively-coupled feed structure is shown in Fig. 2.1(c), which consists of a central feeding strip and two grounding strips on one side of a dielectric substrate, and a coupling pad on the other side of the substrate. The central feeding strip is connected to the inner conductors of an SMA connector, and the coupling pad is directly connected to the meandered cross-loop. By using the two grounding strips, the impedance matching of each RX port could be further improved. The capacitive feed structures and meandered cross loop are implemented on Rogers RO4350B substrates, with a permittivity of 3.48 and a thickness of 1.524 mm.

The four ports of the RX antenna are fed with the same amplitudes and different phase values of 0°, 90°, 180°, 270°, respectively. The distance R_1 between each RX port to the center of the ground plane is 26.29 mm, equivalent to 0.22λ, where λ is the free-space wavelength

at 2.45 GHz. This distance is small enough to ensure a relatively omnidirectional radiation pattern can be obtained [43]. In addition, since the opposing ports of each loop are fed with the same amplitude and 180° phase difference, a near-field null is created on the central axis of the RX array where the TX monopole is placed. This helps achieve a high isolation level between the TX and RX antennas [39−43].

The horizontal portion of the cross loop is meandered to reduce the dimensions of the STAR antenna. As a result, the STAR antenna has a very compact volume of $D \times H =$ 52.6 mm $\times$ 18.5 mm, excluding the ground plane. Indeed, the volume of the proposed STAR antenna is about 98.1% smaller compared to that of a prominent STAR antenna design utilizing the near-field cancellation technique reported in [38, 39] while having similar bandwidth. The use of the meandered cross loop also allows for reducing the distances between the RX ports and hence, resulting in a more omnidirectional radiation pattern of the RX antenna [43]. For the proposed STAR antenna architecture, there are two mutual coupling paths between each RX port and TX port. Due to the rotational symmetry of the whole antenna, here we just show the two coupling paths from RX port #1 to the TX port, as shown in Fig. 2.2(a). Path #1 is the direct coupling path between the TX monopole and the vertical capacitively-coupled feed line of the RX antenna and path #2 is the coupling path via the top hat of the TX monopole and the horizontal meandered section of the RX antenna. The length difference between path #1 and path #2 is around half a wavelength at 2.45 GHz, resulting in destructive interference that reduces the mutual coupling between the TX port and each RX port. As a result, the transmission coefficient between the TX port and each RX port is well depressed, to be lower than −18.3 dB from 2.4 to 2.5 GHz as can be observed from Fig. 2.2(b). The low mutual coupling between the TX antenna and individual RX sections alleviates the requirements of the power handling of the quadrifillar IC.

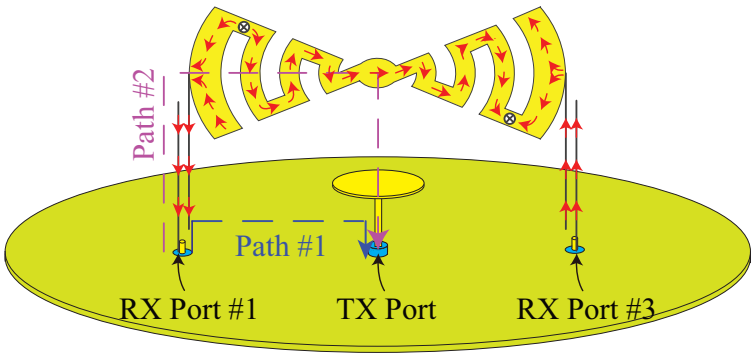

(a)

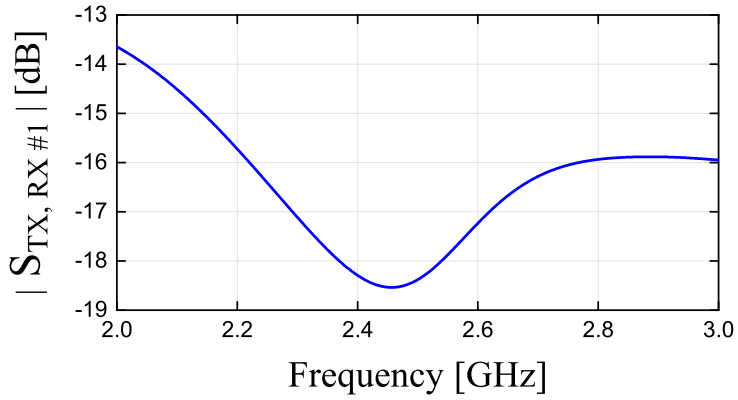

(b)

Figure 2.2: (a) Current distributions and mutual coupling paths when RX Port #1 and #3 are excited with differential signals, while TX Port is loaded with 50 Ω. (b) Mutual coupling between RX port #1 and TX port.

2.2.3 Feeding network for the RX antenna

A quadrifilar IC (RFMW RQF2500Q06) is used to excite the four ports of the RX antenna. The quadrifilar IC is suitable for ISM band and can provide excitation signals with four different phase states of 0°, 90°, 180°, and 270° at its four output ports. We soldered the quadrifilar IC on the feeding network (see Fig. 2.1(g)) and tested the phase and amplitude balance errors at the output ports of the feeding network. Measurement results show a maximum phase balance error of 7.1° and a maximum amplitude balance error of 0.9 dB over the frequency range of 2.4−2.6 GHz.

2.3 Simulation and Measurement Results

We conducted full-wave simulations of the STAR antenna using CST Microwave Studio to predict and optimize its performance. In the simulations, the TX antenna is excited with a waveguide port connected to the SMA connector at its input. The RX antenna is fed through four SMA connectors that are connected to the four outputs of a 5-port data block representing the measured S-parameters of the feeding network. The simulated scattering parameters of the RX antenna were evaluated at the input port of the 5-port data block for the feeding network (the RX port shown in Fig. 2.1(g)). The dimensions of the TX and RX antennas were tuned to achieve good impedance matching, a high TX-RX isolation level, and omnidirectional radiation patterns with a vertical polarization. The finalized dimensions are given in the caption of Fig. 2.1. Subsequently, we fabricated the STAR antenna as shown in Fig. 2.1(f). The RX antenna is connected to the feeding network by using four identical, 250 mm long coaxial cables. The input of the RX antenna is defined as the input port of the feeding network. A vector network analyzer (Agilent N5225A) was used to measure the scattering parameters of the STAR antenna. All measured S-parameters were obtained inside a laboratory in a multi-path environment.

Fig. 2.3 shows the simulated and measured scattering parameters of the TX and RX antennas of the fabricated prototype. The simulated results for the STAR antenna are obtained by combining the CST simulation results of the four-port RX antenna and the measured results of the feeding network. The measured impedance matching bandwidths (for $|S_{11}|$, $|S_{22}| \leq$ -10 dB) of both TX and RX antennas show an overlapping region from 2.3 to 2.6 GHz, which is large enough to cover the 2.45 GHz ISM frequency band. The overlapped impedance matching frequency range acquired from the measurements is slightly larger than the range of 2.4−2.6 GHz predicted in the simulations. The simulated isolation levels (as calculated from $|S_{21}|$ in Fig. 2.3) between the TX an RX antennas are more than 40 dB over of the frequency range from 2.43 to 2.66 GHz with a peak value of 43 dB at

2.56 GHz, while the measured values are higher than 40 dB over almost entire frequency range of 2.4−2.7 GHz with a peak value of 63 dB at 2.5 GHz. The small differences between the simulation and measurement results are mainly due to the fabrication tolerances of the antenna elements and feeding network made manually, imperfections of the four connecting coaxial cables, and the impact of multipath propagation in the measurement environment. It would be well reduced if the feeding network and the antenna ground plane are integrated together, replacing the four coaxial cables with vias, in automated production processes.

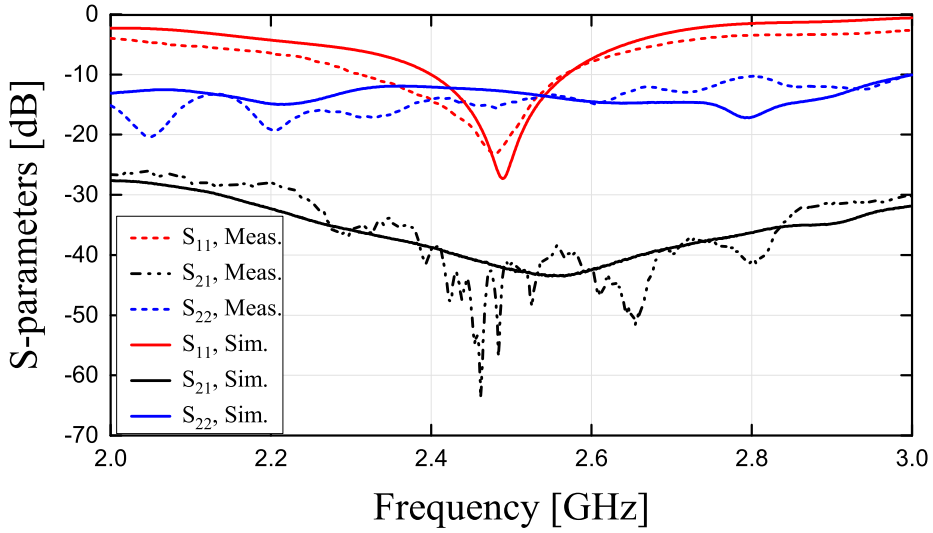

Figure 2.3: Simulated and measured S-parameters of the proposed STAR antenna.

The radiation patterns of the fabricated STAR antenna were measured using a multi-probe, spherical near-field measurement system over a frequency range of 2.0-3.0 GHz. When the RX antenna was measured, the input port of the TX antenna was terminated to 50 Ω, and vice versa. Due to rotational symmetry, the patterns of both the TX and RX antennas in the x-z and y-z planes are similar, and for brevity, the patterns in the y-z plane are not reported. Fig. 2.4 shows the simulation and measurement results for the normalized gain patterns of the TX and RX antenna in both azimuth (x-y plane) and elevation planes (x-z plane) at 2.45 GHz. It can be seen in Fig. 2.4(a) that the RX antenna shows good omnidirectional radiation with vertical polarization in the azimuth plane. The gain variation is less than 1.5

dB over $0° - 360°$ range of ϕ for the RX antenna at 2.45 GHz in the measurements. The RX antenna shows radiation towards the zenith direction, as shown in Fig. 2.4(b), which is mainly due to limited size of the ground plane. A far-field null in the zenith direction could be achieved if an infinitely large ground plane is used. The simulated and measured radiation patterns of the TX antenna are shown in Figs. 2.4(c) and 2.4(d). The TX antenna shows a typical monopole like radiation pattern with two axial nulls in the elevation plane and omnidirectional radiation patterns in the azimuth plane. The gain variation is smaller than 3.2 dB in the azimuth plane for the TX antenna at 2.45 GHz in the measurements. Overall, the simulation and measurement results agree reasonably well on the general shapes of the radiation patterns of both TX and RX antennas. The discrepancies in the normalized gain patterns between the simulated and measured results are mainly due to fabrication tolerances and measurement uncertainty. The simulated and measured realized peak gains of the TX and RX antennas are shown in Fig. 2.5. The reported gain values for both antennas include all of the losses in the feed network including the quadrifillar loss and the loss of coaxial cables used between the RX feed network and the input ports of the RX antenna. The simulation and measurement results show similar trends for the variation of the realized gain with respect to frequency for each antenna. Over the operating frequency range of 2.4-2.5 GHz, the measured realized peak gains of TX and RX antennas range from 0.8-1.8 and 3.2-3.3 dBi, respectively.

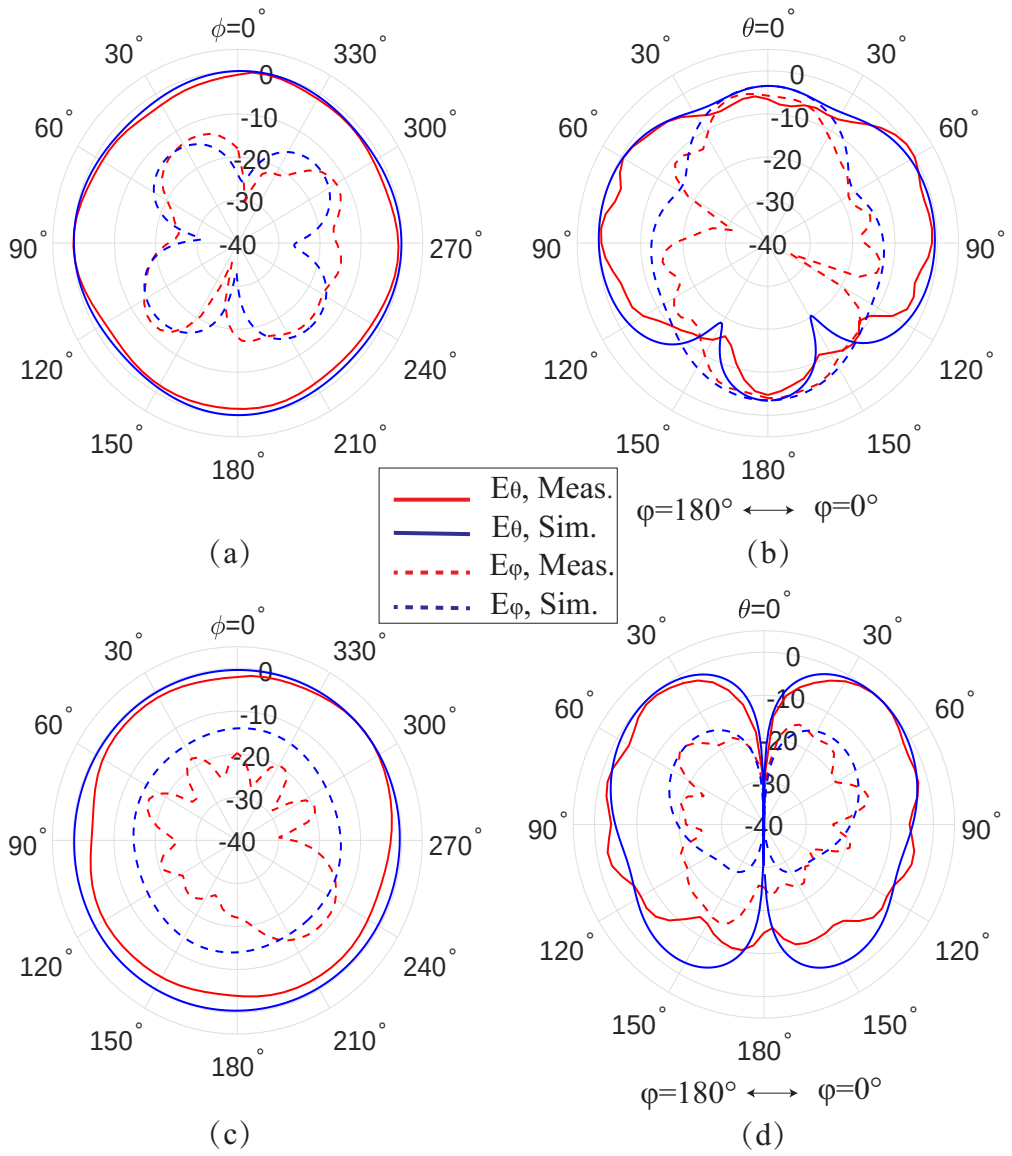

Figure 2.4: Simulated and measured normalized 2-D radiation patterns of the STAR antenna at 2.45 GHz. (a) RX antenna along the azimuth plane (the x-y plane). (b) RX antenna along the elevation plane (the x-z plane). (c) TX antenna along the azimuth plane (the x-y plane). (d) TX antenna along the elevation plane (the x-z plane).

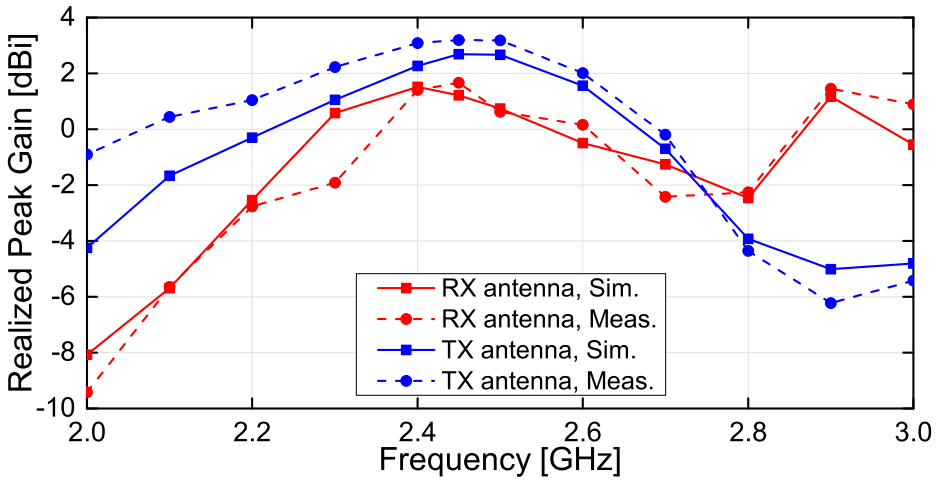

Figure 2.5: Simulated and measured realized peak gains of the TX and RX antennas.

2.4 Conclusions

A vertically-polarized STAR antenna with omnidirectional radiation in the azimuth plane was presented in this paper. The antenna system produces desirable radiation characteristics as well as a high TX-RX isolation level while being compact and low-profile. The RX antenna of this system is a capacitively fed, cross-loop and the TX antenna is a top-hat loaded monopole located at the center of the ground plane and aligned with the vertical symmetry axis of the RX antenna. The four ports of the RX antenna are fed with a quadrifilar IC to achieve a high TX-RX isolation level by utilizing the near-field cancellation technique. Meanwhile, we use the meandered horizontal strips of the cross loop of RX antenna to make the antenna compact and low profile while producing a good vertical polarization. A prototype of the proposed antenna was fabricated and experimentally characterized. The prototype achieves an isolation level better than 38 dB between the TX and RX ports from 2.4 to 2.7 GHz, which covers the 2.45 GHz ISM band. Moreover, the antenna maintains consistent, monopole-like patterns for both TX and RX modes over the entire band of operation.

Chapter 3

An Analytic Synthesis Method for Designing Decoupling and Matching Network for A Two-element Antenna Array

The full manuscript was published as:

Y. Zang, and H. Luyen, H. R. Bahrami and N. Behdad,"An Analytic Synthesis Method for Two-Element Biomimetic Antenna Arrays," *IEEE Trans. Antennas Propag.*, vol. 68, no. 4, pp. 2797-2809, Jan 2020.

An analytic technique for synthesizing the decoupling and matching network (DMN) for a two-element antenna arrays is presented. This method addresses the shortcomings of previous methods used to design decoupling networks with this architecture, which frequently designed with only one unique solution and have a single network topology. We first present an analytic method for determining all possible S-parameters that satisfy the requirements of the 4-port decoupling and matching network of a two-element antenna array. Subsequently, all possible lumped element implementations of the DMNs are presented. Finally, we present a method for determining the values of the reactive elements constituting the DMN from its S-matrix. We demonstrate the proposed design procedure for a two-element antenna array consisting of two 10.3 cm long monopole antennas separated by 5 cm. The design procedure is used to determine the reactive elements constituting the DMNs for two (out of infinity) S-matrices and 13 different DMN architectures. Two representative decoupling networks were also fabricated and the responses of the antenna system using them were characterized experimentally. Measurement results are found to be in good agreement with the simulations, verifying the validity of the proposed synthesis technique.

3.1 Introduction

Multiple-input-multiple-output (MIMO) antenna systems have been widely used in various modern wireless communication and direction finding systems. It is of great interest to reduce the dimensions of antenna arrays used in MIMO systems to meet the growing demands for wireless systems demanding higher mobility and throughputs [67]. As the elements of an antenna array are placed closer to each other, their mutual coupling increases, which can degrade the performance of the array [68]. Numerous multi-port external networks connecting antenna elements have been used to reduce unwanted inter-element coupling of antenna arrays to enhance radiation efficiency [69, 70], increase channel capacity [71 − 74], and minimize noise figures for power amplifiers [75].

Several analytic synthesis methods for designing decoupling networks for MIMO antennas have been presented in the literature [48, 82 − 86]. In [48, 82 − 83], the decoupling networks were synthesized by conditioning their impedance/admittance matrices for decoupling effects and solving the reactive element values for specific classes of network topologies. In [52 − 53, 84], the feed networks were designed to transform the S-matrices of the arrays to their diagonalized forms. Due to the orthogonality of the eigenmodes of the array, the input ports of the external feed networks are naturally decoupled and can be matched independently. The methods presented in these studies only provide a unique solution with one network topology. Using a specific coupling network topology may not yield element values that are easily realizable for the DMNs in all cases. Thus, it is valuable to develop a systematic method for determining all potential DMN topologies for a two-element antenna array and precisely calculating their element values.

In this paper, we identify all possible lumped-element network topologies of the DMN of the decoupling network for a two-element antenna array and present an analytic technique for precisely determining the element values of each DMN implementation. To the best of our knowledge, this work is the first such work that offers a systematic method for determining all potential implementations of DMN of a two-element antenna array and analytically calculating the element values. We first formulate and derive the S-matrix of a four-port network that can decouple and match the antenna array at the intended operating frequency. Subsequently, we examine all possible implementations of a lossless, symmetric, and reciprocal four-port coupling network that can be used to synthesize the desired S-matrix. We show that there are 13 unique topologies that can do this and present an analytic method for determining the values of the reactive elements constituting each network. This design procedure is applied to design the DMN for of a two-element antenna array that consists of two 10.3 cm long monopole antennas separated by 5 cm and operates at ∼625 MHz. The reactive elements of these 13 topologies were calculated using two different S-matrices for each topology. Comparison of the bandwidths in the differential mode of excitation across

different topologies and S-matrices shows that some topologies perform consistently better than others. Therefore, a high-performance DMN topology was selected and two versions of the coupling networks corresponding to the two different S-matrices were fabricated. These coupling networks were realized using lumped components and transmission lines. The responses of both networks were experimentally characterized. The measurement results for output reflection coefficients show a good agreement with the simulation results.

3.2 Synthesis Method

Figs. 3.1(a) and 3.1(b) show the network model of a two-element antenna array with the DMN. When illuminated with a plane wave coming from an oblique incidence angle, the array is excited with a linear combination of the common and differential modes. A lossless four-port DMN is designed to match the impedances of the two antennas to 50 Ω for both the common and the differential modes of excitation. This ensures that the maximum power is delivered to the loads when the array is in the receiving mode. The DMN can be analytically synthesized by deriving its S-matrix and subsequently calculating its reactive element values based on the S-matrix.

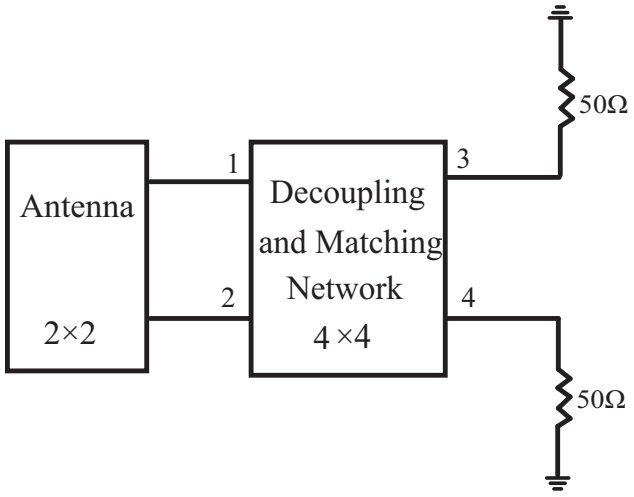

Figure 3.1: Network model of a two-element antenna array with its DMN.

3.2.1 Deriving the S-matrix of the decoupling and matching network

First, we formulate the S-matrix of the network with the following assumptions and conditions:

(C1) The network is lossless, symmetric, and reciprocal;

(C2) Maximum power is transferred from the sources to the loads when the network is excited in the common mode;

(C3) Maximum power is transferred from the sources to the loads when the network is excited in the differential mode;

While these three conditions guarantee the network can match and decouple the antenna array [95].

The S-matrix of the network satisfies the reciprocal condition $[S^T] = [S]$ and the lossless condition $[S][S^H] = [I]$, where $[S^T]$ and $[S^H]$ are the transpose and conjugate transpose of $[S]$, respectively. We express the S-matrix of the four-port coupling network as:

$$[S] = \begin{bmatrix} S_{11} & S_{12} & S_{13} & S_{14} \\ S_{12} & S_{11} & S_{14} & S_{13} \\ S_{13} & S_{14} & S_{33} & S_{34} \\ S_{14} & S_{13} & S_{34} & S_{33} \end{bmatrix}. \tag{3.1}$$

Here, due to symmetry $S_{22} = S_{11}$, $S_{44} = S_{33}$, $S_{42} = S_{13}$, and $S_{32} = S_{14}$. The impedance matrix of the two-element antenna array, which can be acquired via full-wave simulations or measurements, is:

$$[Z] = \begin{bmatrix} Z_{11} & Z_{12} \\ Z_{12} & Z_{11} \end{bmatrix}. \tag{3.2}$$

The coupling network is designed to transform the load impedances to conjugate match the impedances of the antenna array in the common and differential modes of excitation. Therefore, the input impedances, seen at the input of the network when the outputs are connected to 50 Ω, in the common mode ($Z_{in,c}$) and the differential mode ($Z_{in,d}$) can be expressed as:

$$Z_{in,c} = (Z_{11} + Z_{12})^*, \tag{3.3}$$

$$Z_{in,d} = (Z_{11} - Z_{12})^*, \tag{3.4}$$

where the superscript * indicates complex conjugate. Thus, the input reflection coefficients of the equivalent circuits of the network in both modes of excitation can be written in terms of the input impedances and reference impedance (Z_0):

$$\Gamma_{in,c} = \frac{Z_{in,c} - Z_0}{Z_{in,c} + Z_0} = S_{11} + S_{12}, \tag{3.5}$$

$$\Gamma_{in,d} = \frac{Z_{in,d} - Z_0}{Z_{in,d} + Z_0} = S_{11} - S_{12}. \tag{3.6}$$

The values of S_{11} and S_{12} can be calculated from (3.5) and (3.6). With the lossless condition of the network ($[S][S^H] = [I]$), this leaves us with eight unknowns, consisting of the real and imaginary parts of the remaining four scattering parameters (S_{13}, S_{14}, S_{33}, and S_{34}), and only six equations. Thus, we have two degrees of freedom to introduce another two constraints for calculating the whole S-matrix of the DMN, which will be used in the next stage for deriving network element values. Details of the equations used to calculate these parameters and their derivations are provided in Appendix A.

3.2.2 Network topologies and element values

From the derived 4×4 S-matrix, we can express the two S-matrices of the equivalent two-port networks of the common and differential modes as:

$$[S_{comm}] = \begin{bmatrix} S_{11}+S_{12} & S_{13}+S_{14} \\ S_{13}+S_{14} & S_{33}+S_{34} \end{bmatrix}, \tag{3.7}$$

$$[S_{diff}] = \begin{bmatrix} S_{11}-S_{12} & S_{13}-S_{14} \\ S_{13}-S_{14} & S_{33}-S_{34} \end{bmatrix}. \tag{3.8}$$

Since each element of the S-matrices has both real and imaginary parts, there are eight equations for each mode of excitation, adding up to 16 equations in total, if we want to use the S-matrices to solve for the reactance values of the network elements directly. It is not trivial to find the number of independent equations among the 16 equations. However, if we transform the S-matrices to transmission matrices using the equations provided in [87] (page 192), each parameter in the transmission matrices is either real or imaginary for a passive, lossless network. By using the transmission matrices to reduce the number of parameters/equations to eight, it is more convenient to calculate the element values of the network.

After examining all eight parameters of the two transmission matrices (in the common and differential modes), it can be shown that there are only six independent parameters (three for each mode), resulting in six independent equations that need to be solved to match the elements of the transmission matrices. Hence, we must have at least six reactive elements in the coupling network to realize the transmission matrices. The six elements can be chosen from ten possible positions in a generalized, symmetric four-port DMN shown in Fig. 3.2. Fig. 3.2 shows this general coupling network that uses only lumped reactive elements. Additionally, we deducted five rules for choosing the network element positions that can guarantee the uniqueness of the network topology as well as the existence of solutions

for the element values given the characteristics of the two transmission matrices.

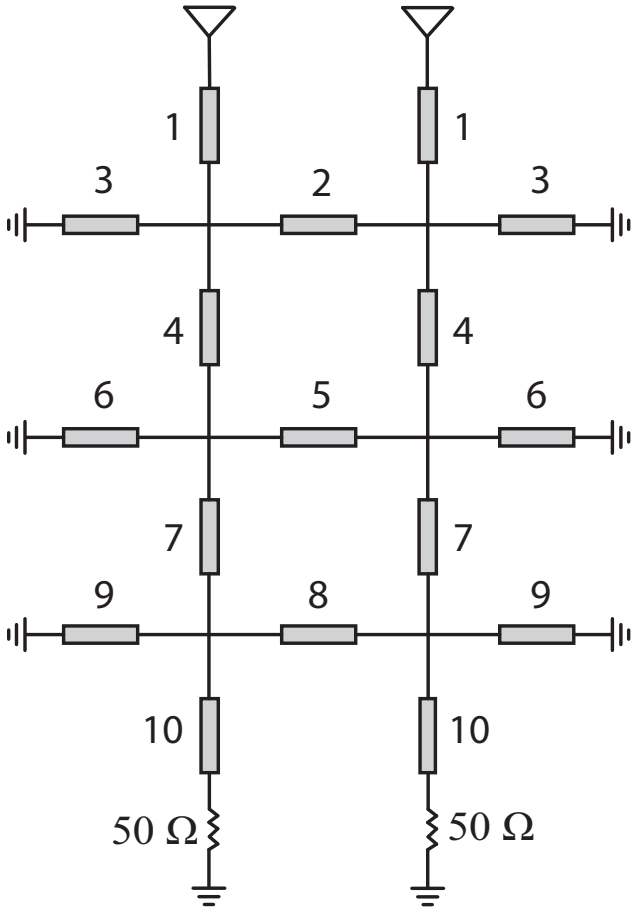

Figure 3.2: A generalized symmetric four-port decoupling and matching network for a symmetric two-element antenna array. This circuit shows the possible positions for the six elements (minimum) needed to synthesize the DMN for a two-element symmetric antenna array.

The five rules are listed as follows (see Appendix B for more detailed discussions of these rules):

(R1) An element in position 1 or 10 must be chosen before choosing one in position 2 or 8, respectively.

(R2) At least two elements from three positions of 2, 5, and 8 must be picked.

(R3) No two elements can be in series/parallel without another parallel/series element added in between.

(R4) The equivalent circuit of the network in the common mode must contain a section that is a Π or a T network.

(R5) An element in position 7 must be chosen if any position from 8, 9, and 10 is to be picked.

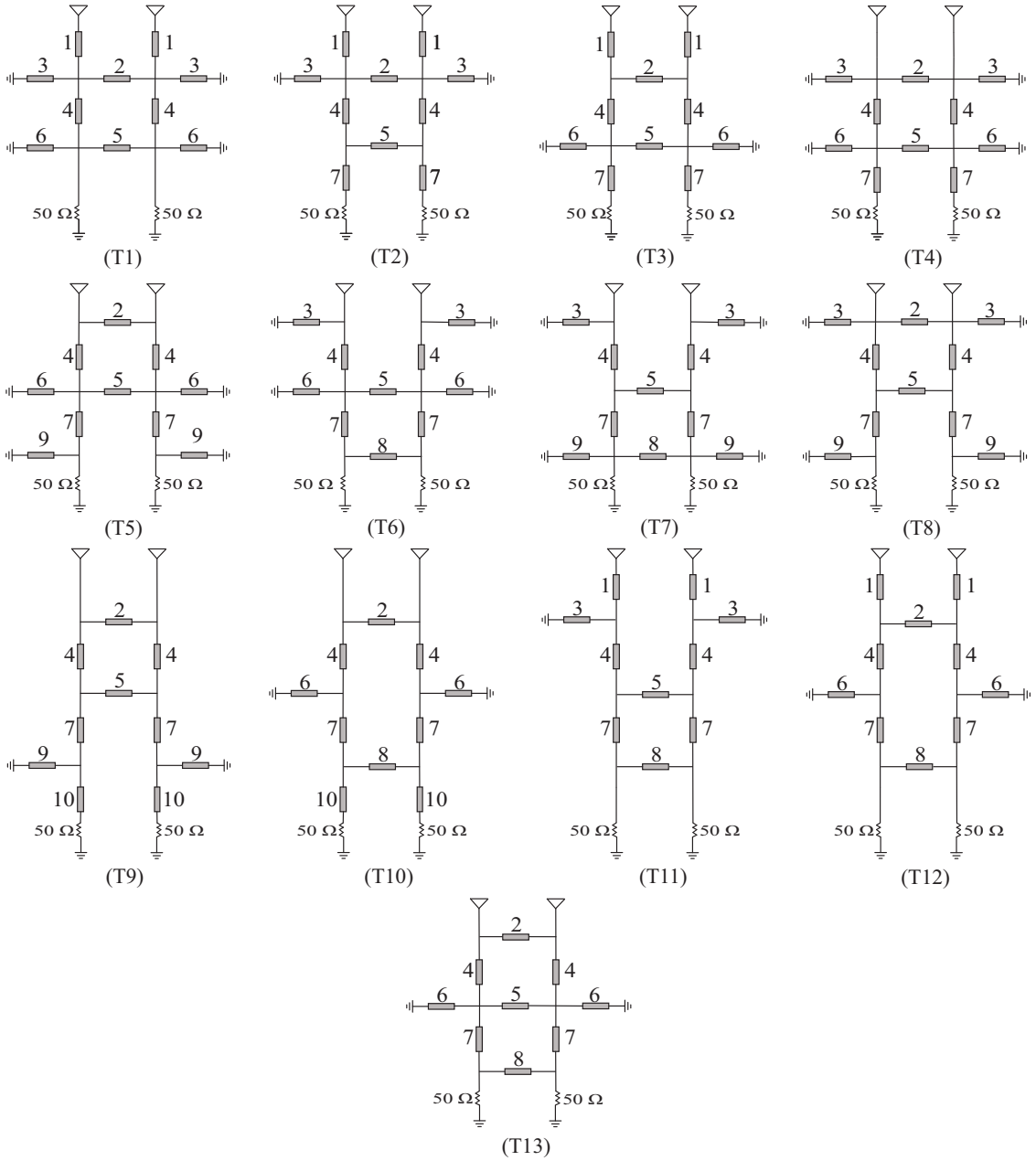

Figure 3.3: 13 unique topologies for implementing DMN for a symmetric two-element antenna array.

Applying all these rules in choosing the network element positions yields a total of 13 unique topologies for the DMN of a symmetric two-element antenna array. These topologies are all shown in Fig. 3.3. For each of these 13 possible topologies, the six reactance values can be determined to produce the exact common- and differential-mode transmission matrices that were derived in the previous steps (see Appendix C for detailed steps for calculating the reactance values).

After choosing the topology of the network, we express the transmission matrices of the equivalent two-port networks in both modes of excitation in terms of the reactance values of the network elements. The reactance values can be solved by matching these two transmission matrices with the two transmission matrices transformed from (3.7) and (3.8) previously (see Appendix C). Subsequently, the calculated reactance values are translated to corresponding inductance and capacitance values.

We summarize the whole synthesis process in the flowchart shown in Fig. 3.4. The first step of the synthesis procedure is to derive an S-matrix for the coupling network. The S-matrix can be calculated when the network is designed with the three conditions (C1)-(C3) and another two arbitrarily added constraints. The next step is to transform the S-matrix to two transmission matrices in the common and differential modes. Subsequently, the network topology is chosen and the transmission matrices in both modes of excitation are expressed in terms of the reactance values of the network elements. The reactance values are derived by solving a system of six equations matching the parameters of the transmission matrices. Eventually, the calculated reactance values are translated to corresponding inductance and capacitance values.

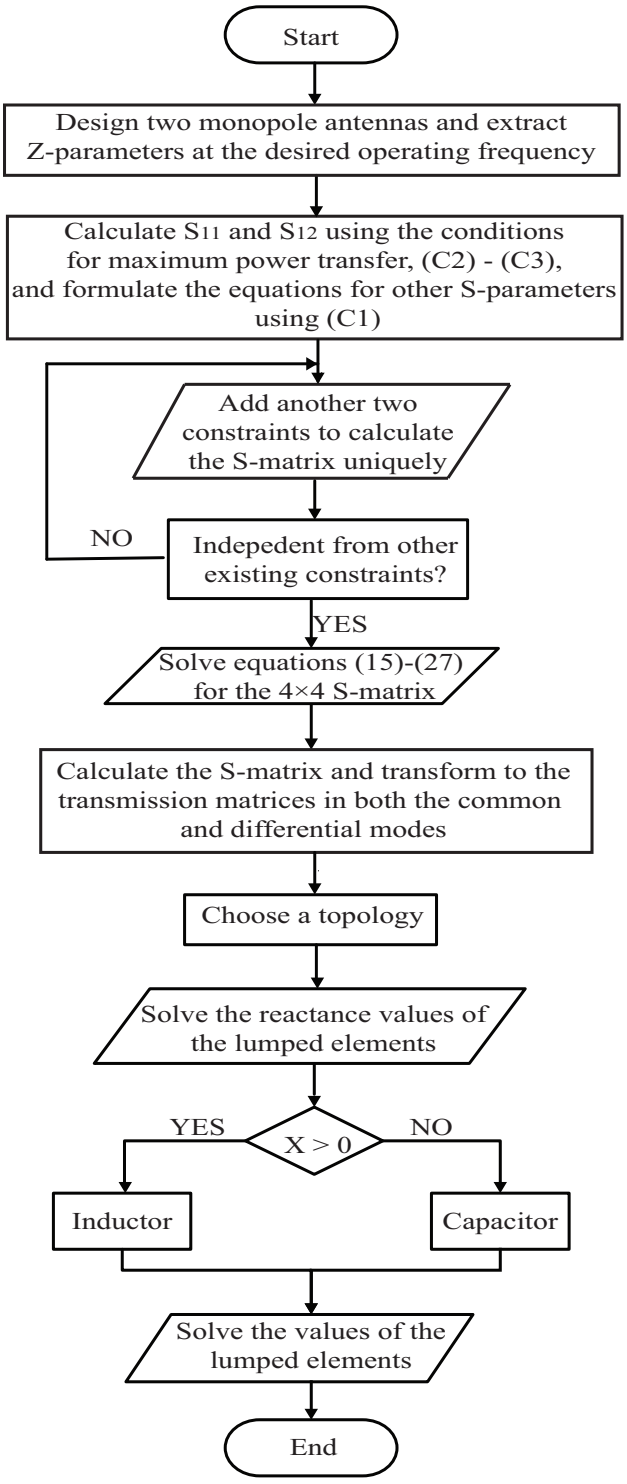

Figure 3.4: Flow chart demonstrating the synthesis procedure of the DMN.

3.3 Design Examples

We applied the synthesis procedure presented in the previous section to design a DMN for a symmetric two-element antenna array intended to operate at 625 MHz. The array consists of two monopole antennas that are 10.3 cm long, separated by 5 cm, and placed above a ground plane with an area of 30 cm × 30 cm. We simulated the antenna array in CST Microwave Studio to extract its two-port impedance matrix at 625 MHz, which will be used for calculation of the S-matrix of the DMN. The derived impedance matrix (where the impedances are in Ω) of the antenna array is:

$$[Z] = \begin{bmatrix} 32.37 + j14.86 & 29.82 + j3.69 \\ 29.82 + j3.69 & 32.37 + j14.86 \end{bmatrix}. \tag{3.9}$$

According to (3.3) and (3.4), we can calculate the input impedances, seen at the inputs of the equivalent circuits of the coupling network, in the common mode as $Z_{in,c} = 62.19 +$ j18.55 Ω and in the differential mode as $Z_{in,d} = 2.55 +$ j11.17 Ω. Using (3.5) and (3.6), we can determine S_{11} and S_{12}:

$$S_{11} = \frac{Z_{in,c}Z_{in,d} - Z_0^2}{(Z_{in,c} + Z_0)(Z_{in,d} + Z_0)} = -0.344 - j0.265, \tag{3.10}$$

$$S_{12} = \frac{(Z_{in,c} - Z_{in,d})Z_0}{(Z_{in,c} + Z_0)(Z_{in,d} + Z_0)} = 0.477 + j0.122. \tag{3.11}$$

Besides conditions (C1) to (C3), we add another two constraints: (1) the phase difference between the output voltages in the common and differential modes is 90°; (2) the phase of S_{21} in the common mode equals to 90°. The first condition is inspired by a previous work in our group [81]. This condition can provide the antenna array with a greater angular phase sensitivity and can find applications in direction finding systems. The added conditions are arbitrary and added to obtain an analytic solution for the S-matrix of the DMN. Since this

condition is arbitrary, one can come up with an infinite number of S-matrices that can satisfy the conditions needed to design a DMN for two-element antenna arrays and find different applications. After introducing this condition, we have eight equations to solve for the real and imaginary parts of S_{13}, S_{14}, S_{33}, and S_{34} (see Appendix A). The calculated S-matrix of the four-port network is shown in (3.12). Subsequently, we transformed the S-matrix to two transmission matrices in the common and differential modes, which are shown in (3.13) and (3.14), respectively. We chose Topology T12 (shown in Fig. 3.3) to demonstrate this new synthesis process. The equivalent circuit model of the two-element antenna array along with the coupling network in both the common and differential modes are shown in Fig. 3.5.

$$[S] = \begin{bmatrix} -0.34-j0.27 & 0.48+j0.12 & -0.15+j0.50 & 0.27+j0.47 \\ 0.48+j0.12 & -0.34-j0.27 & 0.27+j0.47 & -0.15+j0.50 \\ -0.15+j0.50 & 0.27+j0.47 & 0.46-j0.20 & -0.29+j0.31 \\ 0.27+j0.47 & -0.15+j0.50 & -0.29+j0.31 & 0.46-j0.20 \end{bmatrix}. \tag{3.12}$$

$$[ABCD_{comm}] = \begin{bmatrix} -9.149 \times 10^{-6} & -j58.190 \\ -j0.0172 & 0.256 \end{bmatrix}, \tag{3.13}$$

$$[ABCD_{diff}] = \begin{bmatrix} -0.499 & j44.170 \\ -j0.025 & 4.659 \end{bmatrix}. \tag{3.14}$$

Table 3.1: Reactance values for the components of the DMN shown in Fig.3.5 (in Ω).

X_1	-22.749
X_2	23.273
X_4	-35.442
X_6	58.190
X_7	-43.276
X_8	333.250

The transmission matrices in both modes of excitation were written as functions of six reactive elements, X_1, X_2, X_4, X_6, X_7, and X_8. We calculated the transmission matrices for both modes using the equivalent circuit model in Fig. 3.5 by the equations provided in [87] (pp. 190). By matching the rewritten matrices to the ones shown in (3.13) and (3.14), we

arrived at a nonlinear system of six independent equations with six variables (see Appendix C for the detailed procedure for calculating the reactance values). Solving these equations yields the reactance values for the coupling networks, which are listed in Table I. We solved these equations by using the equations and systems solver in MATLAB.

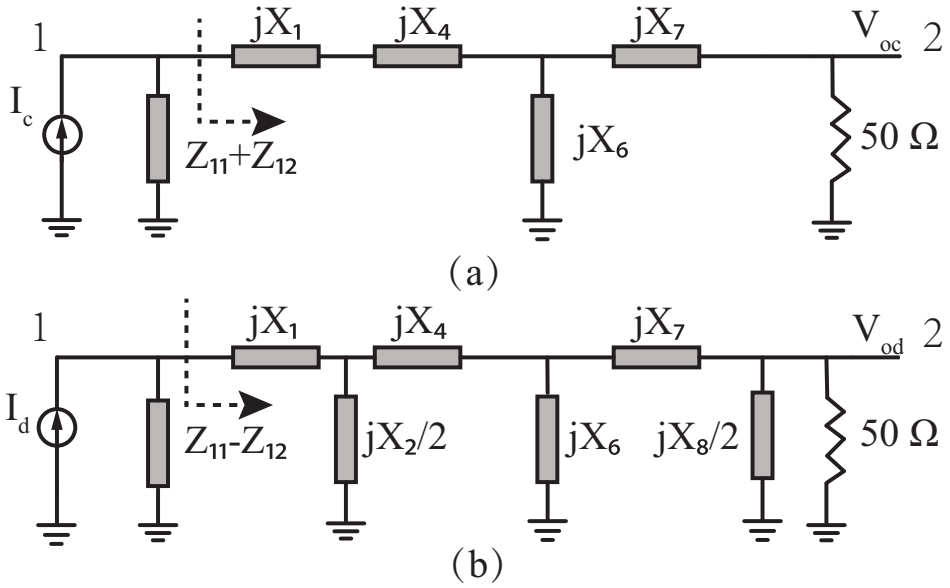

Figure 3.5: The equivalent circuit model of DMN using Topology 12 in the (a) common mode and (b) differential mode of excitation.

Ideal capacitors and inductors corresponding to the calculated reactance values were used in a circuit simulation software to predict the performance of the synthesized DMN. These circuit simulations take into account the Z-parameters and the equivalent short-circuit currents of the two-element antenna array, which were extracted previously from the full-wave simulations of the antenna array, to compute the output reflection coefficients and output phase differences. Since we add the constraint of a enhanced phase difference between two output ports, the results of output phase responses are also simulated and compared. Fig. 3.6(a) shows the output reflection coefficients seen at the output ports (Ports 3 and 4) of the equivalent circuits of the system assuming that Ports 1 and 2 are connected to the two-element monopole array discussed earlier. From the results, we can see the antenna array is decoupled and matched at 625 MHz.

Fig. 3.6(b) shows the simulated phase difference of the signals at the two output ports of the system as a function of the angle of incidence. The result for the two-monopole array without the coupling network, is plotted in the same figure for direct comparison. The phase enhancement factor is defined as $\eta = s/s_0$, where s_0 and s are the slopes of the output phase difference curves at boresight ($\theta = 0°$) of the antenna array with and without the DMN, respectively. For the results shown in Fig. 3.6(b), the phase enhancement factor of the antenna array with DMN is 5.6.

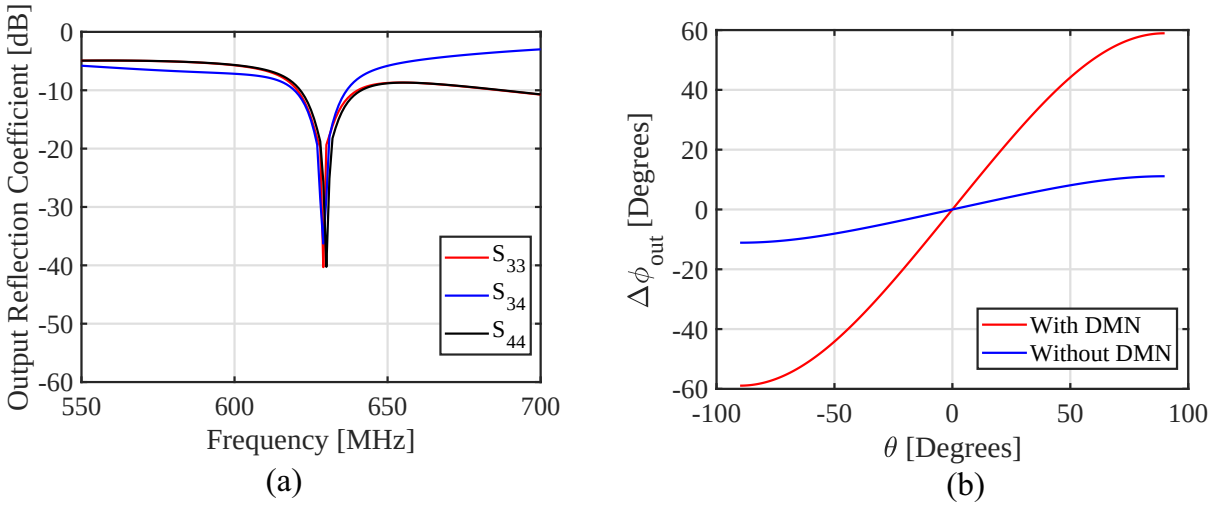

Figure 3.6: (a) Output reflection coefficients of the two-element antenna array with the DMN discussed in Section III. (b) Phase difference between the voltages at the two outputs of the antenna array.

3.4 Impacts of the ECN Topology and S-Matrix Constraints

As discussed in the previous section, there are infinite S-matrices that can decouple and match the antenna array. Moreover, there are 13 unique topologies that can be used to implement the DMN. Thus, there are an infinite number of DMN implementations for a given two-element antenna array. While an exhaustive investigation of the choice of S-matrix or the coupling element on the performance of the DMN is beyond the scope of this article, we

nonetheless briefly examine this subject in this section. Specifically, we pick two different constraints as the added eighth condition needed to analytically determine the S-matrix values. For each S-matrix, 13 different unique DMNs were designed and simulated and the performances of the antenna system using them in terms of differential-mode bandwidth were compared among all 13 topologies since the overall impedance bandwidth of the DMN is mostly limited by the bandwidth of the differential mode. The phase enhancement factors were also compared between the two S-matrices at the operating frequency. First, we fabricated a two-element monopole array consisting of two 10.3 cm long monopole antennas separated by 5 cm. The monopole antennas are made of solid copper tubes with a circular cross-section with the radius of 3 mm and mounted on a brass ground plane with physical dimensions of 30 cm $\times$ 30 cm. We measured the scattering parameters of the two-port antenna array using a vector network analyzer (Agilent N5225A). We observed that the resonant frequency of the two-element antenna array is around 610 MHz and extracted its impedance matrix at this frequency to design the DMN. The measured S-parameters of the two-element antenna array were used to calculate the S-matrices of the DMNs.

The first S-matrix was calculated by using equations (A.1)-(A.9) given in Appendix A using the added constraint that $\angle S_{21} = 90^\circ$ in the common mode (equation (A.11) in Appendix A) at 610 MHz. The second constraint was determined by minimizing the variance of the absolute value of the derivative of the output reactances in the differential mode with respect to frequency from 605 to 615 MHz (see equation (A.13) in Appendix A). Each of these additional constraints allows for analytically determining a distinctive S-matrix for the DMN. Using each of these two S-matrices, we synthesized the element values for the 13 topologies shown in Fig. 3.3. The measured frequency-dependent S-parameters of the two-element antenna array were used along with ideal capacitors and inductors representing the DMN's lumped elements to generate the differential-mode impedance matching bandwidths of the antenna system in circuit simulations. Table II shows the simulation results for the bandwidths in the differential mode of the antenna array with these different coupling

Table 3.2: Differential-mode bandwidths (in MHz) for the antenna array using different DMNs (discussed in section IV) corresponding to two S-matrices and 13 topologies.

Topology	S-matrix 1	S-matrix 2
T1	9.2	9.2
T2	8.2	7.7
T3	8.3	8.1
T4	5.8	8.8
T5	7.9	7.7
T6	8.5	7.9
T7	8.3	8.1
T8	7.2	7.7
T9	7.8	7.7
T10	5.0	8.6
T11	8.2	7.9
T12	9.2	9.3
T13	9.2	9.0

networks. The simulation results show that, across different topologies, the largest and smallest bandwidths are 9.2 and 5.0 MHz for the first S-matrix, and 9.3 and 7.7 MHz for the second S-matrix, respectively. We observed that some topologies are superior to others according to the impedance-matching bandwidth in the differential mode. For some of the DMN topologies (e.g, topology T1, T12, and T13), the influence of different S-matrices on the bandwidth is insignificant. The second S-matrix seems to outperform the first one as it provides larger bandwidths for most of the topologies. Additionally, the bandwidth is also less sensitive to the choices of the network topology for the second S-matrix.

Fig. 3.7 shows the simulated output phase differences of the antenna array using different DMNs as functions of the angle of incidence and compares with the original antenna array. The results were generated for the antenna array two DMNs (both of Topology 1 but with different S-matrices). It should be noted that the phase enhancement factor is determined by the S-matrix of the DMN regardless of the network topology[1]. Therefore, at the operating frequency, different network topologies have the same output phase responses as long as they

[1]This statement is valid for an ideal coupling network consisting of lumped elements and ignores the parasitics involved in implementing the DMN.

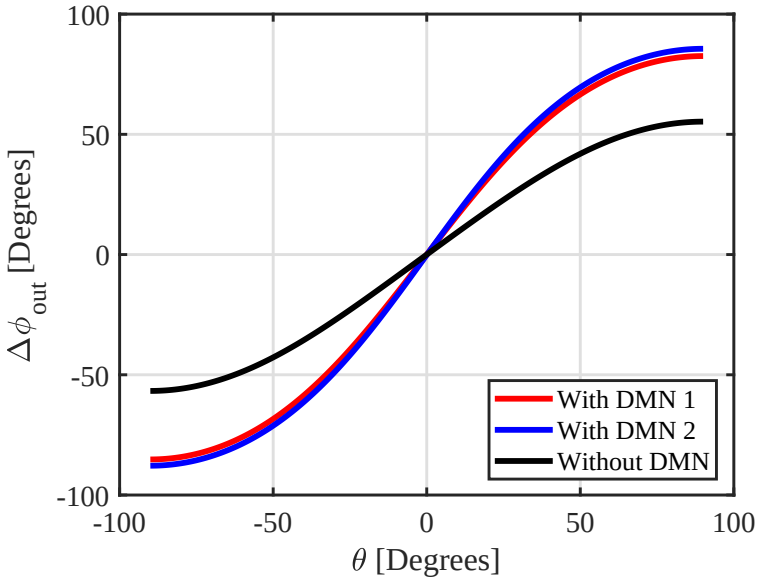

Figure 3.7: Simulated output phase responses of the two-element antenna arrays with and without the DMNs discussed in Section IV.

have the same S-matrix. From Fig. 3.7, the slopes of the output phase difference curves are 1.73 and 1.77 for the antenna array using the DMN with the first and second S-matrix, respectively, and 0.93 for without the DMN. The corresponding phase enhancement factors of the two antenna system are 1.87 and 1.91, respectively. These phase enhancement factors are smaller than that of the antenna system shown in the previous section. This is due to the fact that the results in this section are generated using the measured S-parameters of the fabricated prototype of the two-element antenna array while the result in the previous section is produced using the simulated S-parameters extracted from full-wave simulations of the antenna array. There seems to be no obvious difference on the impact of the two S-matrices on the phase enhancement factor at 610 MHz since they both satisfy the condition that the output-voltage phasors in the common and differential modes being orthogonal at boresight, which was shown to allow the maximum possible phase enhancement factor for the antenna system in [95].

3.5 Experiments

We chose Topology 1 (T1), which along with Topologies 12 and 13 seem to provide better bandwidths compared to the other topologies, and fabricated two versions of the coupling networks corresponding to the two S-matrices as mentioned in Section IV. Figs. 3.8(a) and 3.8(b) show the photographs of the fabricated antenna array and DMNs, respectively. The DMNs were implemented on Rogers RO4003C substrates with a dielectric constant of $\epsilon_r = 3.55$ and thickness of 0.508 mm. The reactive elements of the DMN were realized using lumped capacitors and inductors as well as transmission lines. The values of the lumped elements used in these DMN are provided in Table III and the lengths and characteristic impedances of the different transmission lines are listed in Table IV.

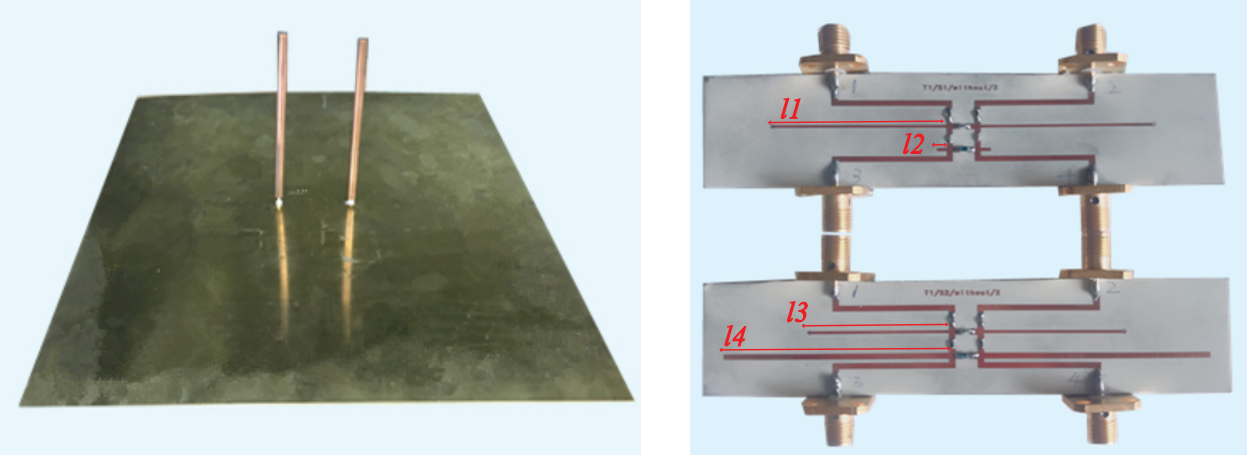

(a) (b)

Figure 3.8: Photographs of the fabricated prototype. (a) The two element monopole antenna array. (b) Two-input two-output DMN.

We connected the monopoles to input ports of the corresponding coupling network and measured its scattering parameters at the two output ports of the DMN using the vector network analyzer. To characterize the output phase responses of the fabricated antenna system, we followed a procedure consisting of several steps of measurements and data post-processing. First, we used a spherical near-field antenna measurement system to characterize the radiation patterns of the antenna array without a coupling network. The radiation

Table 3.3: Values of the lumped elements used in the fabricated DMN.

Position	S_1	S_2
1	2.5 pF	2.3 pF
2	1.5 pF	1.6 pF
3	TL(l_1)	TL(l_3)
4	2.4 pF	5.6 pF
5	180 nH	82 nH
6	TL(l_2)	TL(l_4)
TL: Transmission line		

Table 3.4: Lengths and characteristic impedances (Z_0) of the different transmission lines used in the fabricated DMN.

Transmission Line	Length (mm)	Width (mm)	Z_0 (Ω)
l_1	34.56	0.55	75
l_2	0.84	1.14	50
l_3	27.55	0.55	75
l_4	43.74	1.14	50

patterns of the monopole antennas in the horizontal plane were used to extract the equivalent short-circuit current sources, acting as the input sources for the antenna array, as the angle of incidence changes from $-90°$ to $90°$. Subsequently, the extracted input current sources and the measured S-parameters of the antenna array with and without DMNs were used to generate the measurement results for the output phase responses of the antenna system.

Figs. 3.9(a)-(c) show the measured and simulated output reflection coefficients of the antenna array with the DMN 1. Figs. 3.9(d)-(f) show the measured and simulated output reflection coefficients of the antenna array with the DMN 2. From the results, we can see the antenna array is decoupled and matched at around 600 MHz for both DMNs. The center frequencies of impedance-matching bandwidth and the decoupling are shifted in the measurement results compared to the simulation results by about 10 MHz. There are several reasons contributing to these frequency shifts. These include fabrication tolerances (e.g, inductors and capacitors have respectively tolerances of 2% and 8%), slight asymmetry of the precise dimensions of the two monopoles, small differences between the SMA adapters

used to connect the two-element monopole array to the DMN, and the tolerances of the exact values of the dielectric constant and loss tangent of the substrate used to implement the DMN. Furthermore, simulation and measurement uncertainties are potential additional factors that may contribute to the differences observed between the predicted and measured responses. Additionally, the short transmission line sections that connect the lumped elements of the DMN were not considered in the simulations. These short transmission lines add parasitic reactances, causing the operating frequencies of the network to change. Despite these frequency shifts, the measured responses of the antenna array with the DMNs agree well with the values predicted in the simulations.

Figs. 3.10(a) and 3.10(b) show the measured and simulated output phase differences of the antenna array with two DMNs as functions of the incident angle. The measured and simulated results without the DMN are also shown for comparison. In general, the measured output phase differences show a good agreement with the values predicted by the simulations. The simulated phase enhancement factors are 2.61 and 2.78 for the antenna array with two DMNs, respectively, while the measured phase enhancement factors are 1.92 for both. The measured phase enhancement factors for the two antenna systems are lower than the values predicted in the simulations. These discrepancies are commensurate with the noticeable difference between the measurement and simulation output phase response of the original antenna array without the DMNs as can be seen in Figs. 3.10(a) and 3.10(b), which can be primarily attributed to a slight asymmetry of the two monopoles as well as the fact that a finite ground plane was used in the measurements while an infinite ground plane was used in the simulations.

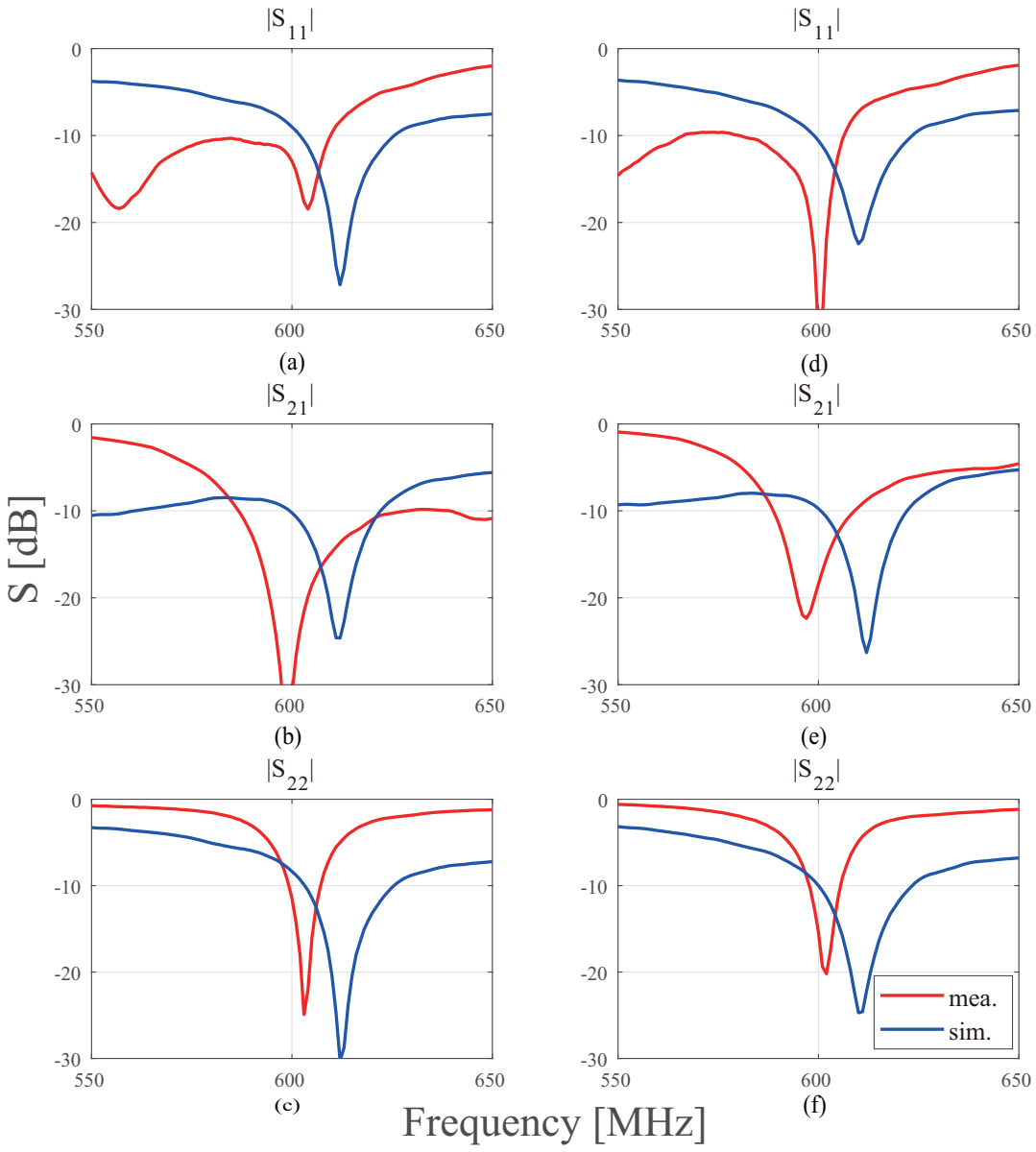

Figure 3.9: Measured and simulated output reflection coefficients of the antenna array with two fabricated DMNs (a)-(c) DMN 1 and (d)-(f) DMN 2.

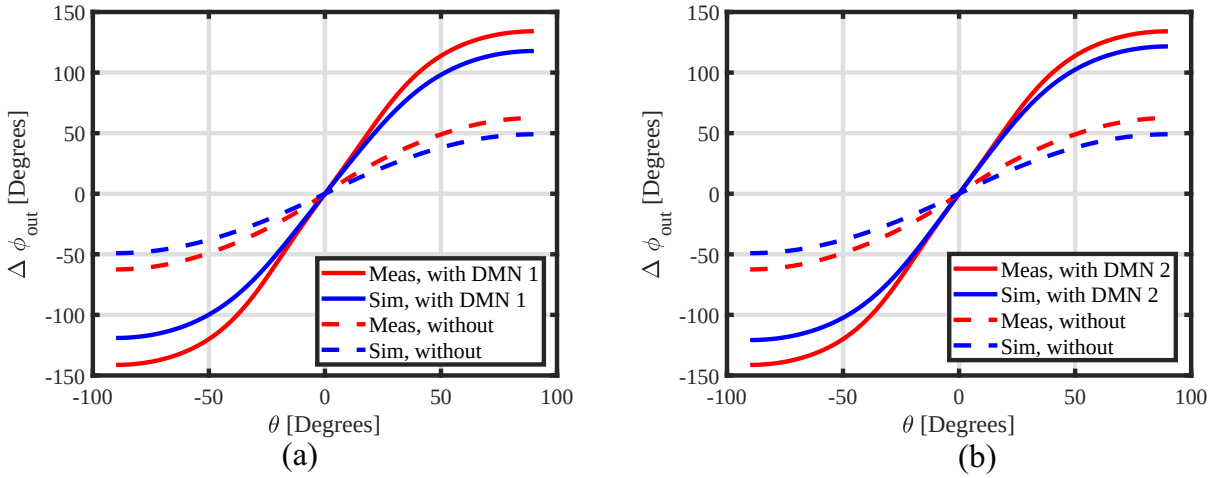

Figure 3.10: Measured and simulated output phase responses as functions of the angle of incidence of (c) antenna array with DMN 1 and (d) antenna array with DMN 2.

3.6 Conclusions

We presented a new procedure for analytically synthesizing the decoupling and matching network for a symmetric, two-element antenna array. Using this approach, we can determine the S-parameters of the DMN and use them to synthesize its coupling network. The synthesis procedure starts with formulating and deriving a specific S-matrix for the DMN. Subsequently, the transmission matrices of the equivalent circuits of the network in the common and differential modes are calculated from the S-matrix and used to solve for the reactive element values of the network. By using the transmission matrices, we can reduce the number of equations and deduce that the network needs at least six reactive elements to realize these transmission matrices. We investigated all possible options for a symmetric four-port coupling network consisting of lumped reactive elements from a generalized topology and identified 13 unique topologies that can be used to implement the DMN. The facts that an infinite number of S-matrices exist that decouple and match the antenna array and 13 unique DMN topologies can be used, result in infinite design varieties. We conducted a small scale investigation by examining the differences between the performances of DMNs using

two different S-matrices and 13 different network topologies. These results suggest that some S-matrix choices and topologies may have advantages over others in terms of bandwidth or simplicity of implementation. Our limited-scale simulation results show that some topologies consistently provide wider differential-mode impedance matching bandwidths compared to the others. A topology with a good simulated performance was chosen for fabrication of two prototypes of the DMN corresponding to the two different S-matrices. Measurement results for the output reflection coefficient and the phase enhancement factors of the antenna array with two fabricated DMN confirmed the results obtained from simulations.

Chapter 4

An Analytic Synthesis Method for Designing Decoupling and Matching Network for A Three-element Antenna Array

4.1 Introduction

Multi-input-multi-output (MIMO) antenna systems have been widely adopted in modern mobile communications to increase the data throughput. However, as the number of antenna elements increases in a compact wireless device, the electrical distances between the antenna elements decrease, and the mutual coupling as well as pattern correlation increase [88]. In a MIMO system, strong mutual couplings between the antenna elements results in significant deterioration of the overall performance of the system. Furthermore, the channel capacity can be greatly affected in a highly correlated channel. These drawbacks limit the benefits of a MIMO system in such situations. Therefore, it is important that a simple but effective decoupling technique is developed for a multiple antenna system.

Very few existing decoupling techniques can effectively deal with a decoupling problem of a compact array with more than two elements. The most obvious method is to apply conventional two-element decoupling techniques to every pair of elements in the array. Such techniques include using electromagnetic band gap (EBG) structures [34], defected ground structures [89], [90], and inserted transmission lines network changing the characteristic admittance between elements [48]. But these methods will lead to complex circuitry when applied to a multi-element array. There are also some techniques have already been applied in decoupling multi-element antenna array. Most of the methods involve mode-decomposition that diagonalizes the S-parameters of a coupled array [52 − 53, 91 − 92]. In these references, they have different coupling sections, serval hybrid couplers or multi-layer networks, which make the dimensions of the network large and increase the complexity as well. These methods can only be applied to smaller arrays due to the complexity as well.

Inspired by our previous work in Chap 3, we developed an analytical method for synthesizing a decoupling and matching network (DMN) for both a center-symmetric and a linear three-element antenna array, as shown in Fig. 4.1. Using the approach reported in this chapter, we can determine the scattering parameters (S-parameters) of the DMN that can

simultaneously impedance match and decouple the antennas. Subsequently, this S-parameter matrix will be used to synthesize the DMN itself.

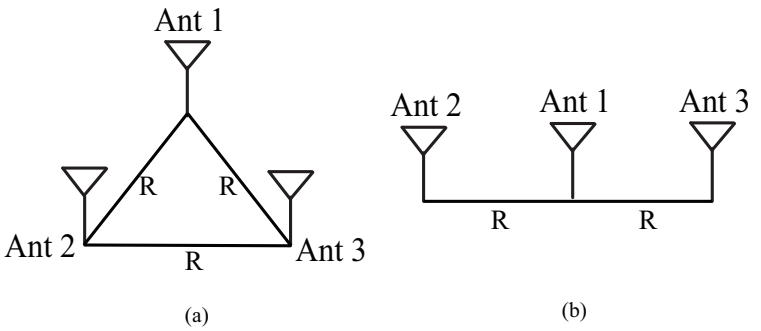

Figure 4.1: (a) Center-symmetric antenna array. (b) Linear three-element antenna array.

For the center-symmetric case, the synthesis procedure starts with formulating and deriving a specific S-matrix for the DMN to provide the desired performance, including maximum power extraction in different modes. Subsequently, the transmission matrices of the equivalent circuits of the network in two different modes are calculated from the S-matrix and used to solve for the reactive element values of the network. Besides, we investigate all possible options for a symmetric six-port decoupling network consisting of lumped reactive elements from a generalized topology that can be used to implement the decoupling network for a three-element antenna array.

As a proof of concept demonstration, we examine a system with a three-element antenna array consisting of three monopole antennas, which operate at 600 MHz. The antennas are positioned on the corners of an equilateral triangle whose side length is 5 cm. All three monopoles are identical. The representative DMN was also fabricated and the response of the system was characterized experimentally. Measurement results are found to be in good agreement with the simulations, verifying the validity of the proposed synthesis technique.

For the linear case, the analysis exploits singular value decomposition (SVD) of the scattering parameter matrix of the antenna and that of the matching network. Using this process, we derive a specific S-matrix for the DMN to provide port decoupling and impedance match the antenna at the desired frequency of operation. We can synthesize the network

as a six-branched star network with capacitors and inductors. The element values can be calculated by transforming the S-matrix of the DMN to the admittance matrix (Y-matrix). To verify our approach, we simulated a linear three-element antenna with 110 mm long monopoles, separated by 5 cm, which are placed on a ground plane with a radius of 40 cm in CST Microwave Studio. Then, we proposed detailed procedures to design a decoupling network for the antenna array at 600 MHz. The desired decoupling and matching performances are shown in the simulation results.

4.2 Decoupling and Matching Network Design for A Center-symmetric Three-element Antenna Array

4.2.1 Modal analysis of the system

Fig. 4.2(a) shows the block diagram of a three-element, center-symmetric antenna array with decoupling and matching network. A three-input-three-output DMN, which takes the input signals received at the antenna terminals (labeled as V_{i1}, V_{i2}, and V_{i3}) and converts them to the output signals measured at the outputs of the DMN (labeled as V_{o1}, V_{o2}, and V_{o3}).

Considering reciprocity and symmetry, the frequency-dependent impedance matrix, [Z], characterizes the self and mutual impedances of the different elements of the array can be represented as:

$$[Z] = \begin{bmatrix} Z_{11} & Z_{12} & Z_{12} \\ Z_{12} & Z_{11} & Z_{12} \\ Z_{12} & Z_{12} & Z_{11} \end{bmatrix}. \tag{4.1}$$

In the eigenmode analysis, the antenna system has three linearly independent eigenmodes identified as Modes A, B and C. The eigenvalues of the impedance matrix (modal admittances) as described in [93] and [94] are:

$$Z_A = R_A + jX_A = Z_{11} + 2Z_{12},$$
$$Z_B = Z_C = R_B + jX_B = Z_{11} - Z_{12}. \tag{4.2}$$

with orthogonal unit eigenvectors $[\hat{1}, \hat{1}, \hat{1}], [\hat{-1}, \hat{0}, \hat{1}]$, and $[\hat{2}, \hat{-1}, \hat{-1}]$. In the modal analysis, the decoupling network decouples the ports of the array by matching all the mode-impedances. Such a network with three independent inputs has three linearly independent modes of excitation, which form a set of orthogonal basis functions. For an arbitrary excitation, the response of the circuit can be represented in terms of a linear combination of the responses of the circuit for each basis function. In this analysis, however, we choose the eigenvectors of the antenna array as the independent modes of excitations to simplify the subsequent circuit analysis steps. Based on this assumption for these orthogonal vectors, the response of the array for a general incoming wave in terms of (V_{iA}, V_{iB}, and V_{iC}) for different modes can be decomposed as shown in Fig. 4.2 (b)-(d). The networks have output voltages labeled as $\bar{V}_{oA}$, $\bar{V}_{oB}$, and $\bar{V}_{oC}$, respectively.

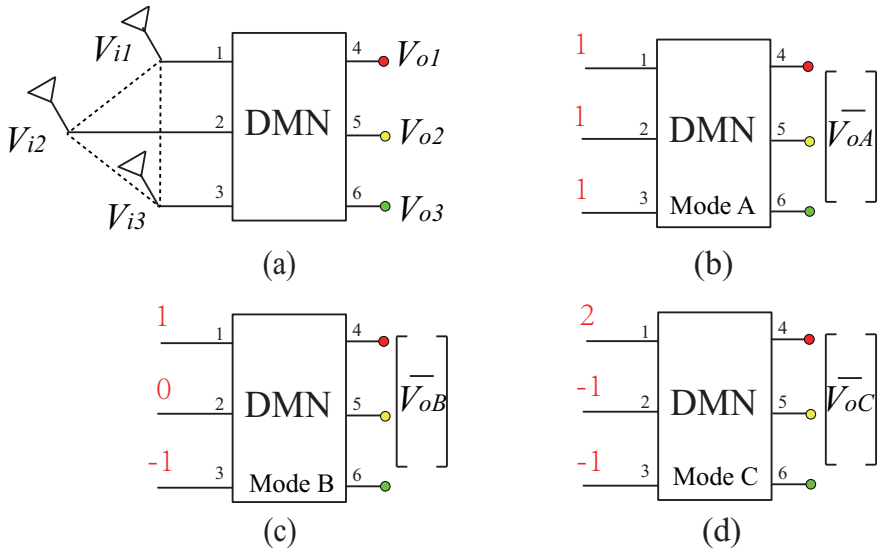

Figure 4.2: (a) Generic model of a three-element antenna array with a 3×3 DMN. The antenna system is considered to be rotationally symmetric when rotated by 120°. This array has three linearly independent modes of excitation identified here as Modes A, B, and C. (b-d) Equivalent circuit model of the antenna array and its simplified DMN for each specific mode of excitation.

4.2.2 Deriving the S-matrix of the decoupling and matching network

First, we formulate the S-matrix of the network with the assumptions that it is lossless, symmetric, and reciprocal. The network can match and decouple the three-element antenna array and maximum power is transferred from the sources to the loads when the network is excited in different modes of excitation.

The S-matrix of the network satisfies the reciprocal condition $[S^T] = [S]$ and the lossless condition $[S][S^H] = [I]$, where $[S^T]$ and $[S^H]$ are the transpose and conjugate transpose of $[S]$, respectively. We express the S-matrix of the six-port coupling network as:

$$[S] = \begin{bmatrix} S_{11} & S_{12} & S_{12} & S_{14} & S_{15} & S_{15} \\ S_{12} & S_{11} & S_{12} & S_{15} & S_{14} & S_{15} \\ S_{12} & S_{12} & S_{11} & S_{15} & S_{15} & S_{14} \\ S_{14} & S_{15} & S_{15} & S_{44} & S_{45} & S_{45} \\ S_{15} & S_{14} & S_{15} & S_{45} & S_{44} & S_{45} \\ S_{15} & S_{15} & S_{14} & S_{45} & S_{45} & S_{44} \end{bmatrix}. \tag{4.3}$$

Here, due to symmetry, $S_{11} = S_{22} = S_{33}$, $S_{44} = S_{55} = S_{66}$, $S_{12} = S_{13} = S_{23}$, $S_{14} = S_{25} = S_{36}$, $S_{15} = S_{16} = S_{25}$, and $S_{45} = S_{46} = S_{56}$.

The coupling network is designed to transform the load impedances to conjugate match the impedances of the antenna array in different eigenmodes of excitation. Therefore, the input impedances, seen at the input of the network when the outputs are connected to 50 Ω, when the system is excited in Modes A, B, and C can be expressed as:

$$Z_{in,\ A} = (Z_{11} + 2Z_{12})^*, \tag{4.4}$$

$$Z_{in,\ B} = Z_{in,\ C} = (Z_{11} - Z_{12})^*, \tag{4.5}$$

where the superscript * indicates complex conjugate. Thus, the input reflection coefficients of the equivalent circuits of the network in all modes of excitation can be written in terms of the input impedances and reference impedance (Z_0):

$$\Gamma_{in,\ A} = \frac{Z_{in,\ A} - Z_0}{Z_{in,\ A} + Z_0} = S_{11} + 2S_{12}, \tag{4.6}$$

$$\Gamma_{in,\ B} = \Gamma_{in,\ C} = \frac{Z_{in,\ B} - Z_0}{Z_{in,\ B} + Z_0} = S_{11} - S_{12}. \tag{4.7}$$

The values of S_{11} and S_{12} can be calculated from (4.6) and (4.7). With the lossless condition of the network ($[S][S^H] = [I]$), this leaves us with eight unknowns, consisting of the real and imaginary parts of the remaining four scattering parameters (S_{14}, S_{15}, S_{44}, and S_{45}), and only seven equations. Thus, we have one degree of freedom to introduce another constraint for calculating the whole S-matrix of the decoupling network, which will be used in the next stage for deriving network element values.

4.2.3 Decoupling and matching network topologies and element values

From the derived 6×6 S-matrix, we can express the two S-matrices of the equivalent two-port networks of mode A and B shown in Fig. 4.2(b) and 4.2(c)as:

$$[S_{mode,\ A}] = \begin{bmatrix} S_{11} + 2S_{12} & S_{14} + 2S_{15} \\ S_{14} + 2S_{15} & S_{44} + 2S_{45} \end{bmatrix}, \tag{4.8}$$

$$[S_{mode,\ B}] = \begin{bmatrix} S_{11} - S_{12} & S_{14} - S_{15} \\ S_{14} - S_{15} & S_{44} - S_{45} \end{bmatrix}. \tag{4.9}$$

The next step should be to find the implementation of the network, which the S-matrices of the network in Mode A and B are the same as what we calculated in (4.8) and (4.9). If we

want to match the S-matrices directly, we will end up solving a non-linear equations system with 16 equations. Because each element of the S-matrices has both real and imaginary parts, there are eight equations for each mode of excitation, which will add up to 16 equations in total. But the equation system can not be solved since it is not trivial to find the number of independent equations among the 16 equations. However, if we transform the S-matrices in (4.8) and (4.9) to transmission matrices using the equations provided in [87] (page 192), the number of equations will reduce to eight since each parameter in the transmission matrices is either real or imaginary for a passive, lossless network. By using the transmission matrices to reduce the number of parameters/equations to eight, it is more convenient to calculate the element values of the network.

From Section 3.2.2, we noticed that one must have at least six reactive elements in the network to realize the transmission matrices. The six elements can be chosen from ten possible positions in a generalized, symmetric six-port external coupling network shown in Fig. 4.3. Additionally, after applying all the rules in Section 3.2.2 in choosing the network element positions yields a total of 13 unique topologies for the DMN. These topologies are all shown in Fig. 4.4. For each of these 13 possible topologies, the six reactance values can be determined to produce the exact different modes of the transmission matrices (Mode A and Mode B) that were derived in the previous steps (see (E.1) to (E.11) in Appendix E for detailed steps for calculating the reactance values).

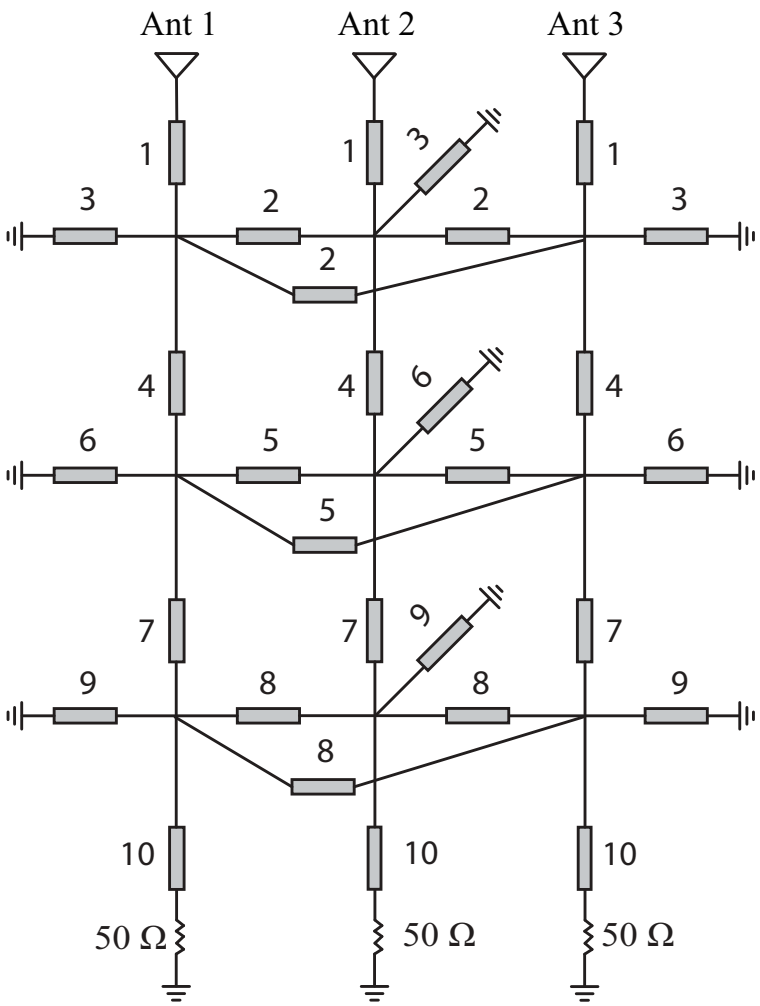

Figure 4.3: A generalized symmetric six-port DMN for a three-element antenna array. This circuit shows the possible positions for the six elements (minimum) needed to synthesize the DMN for a three-element antenna array.

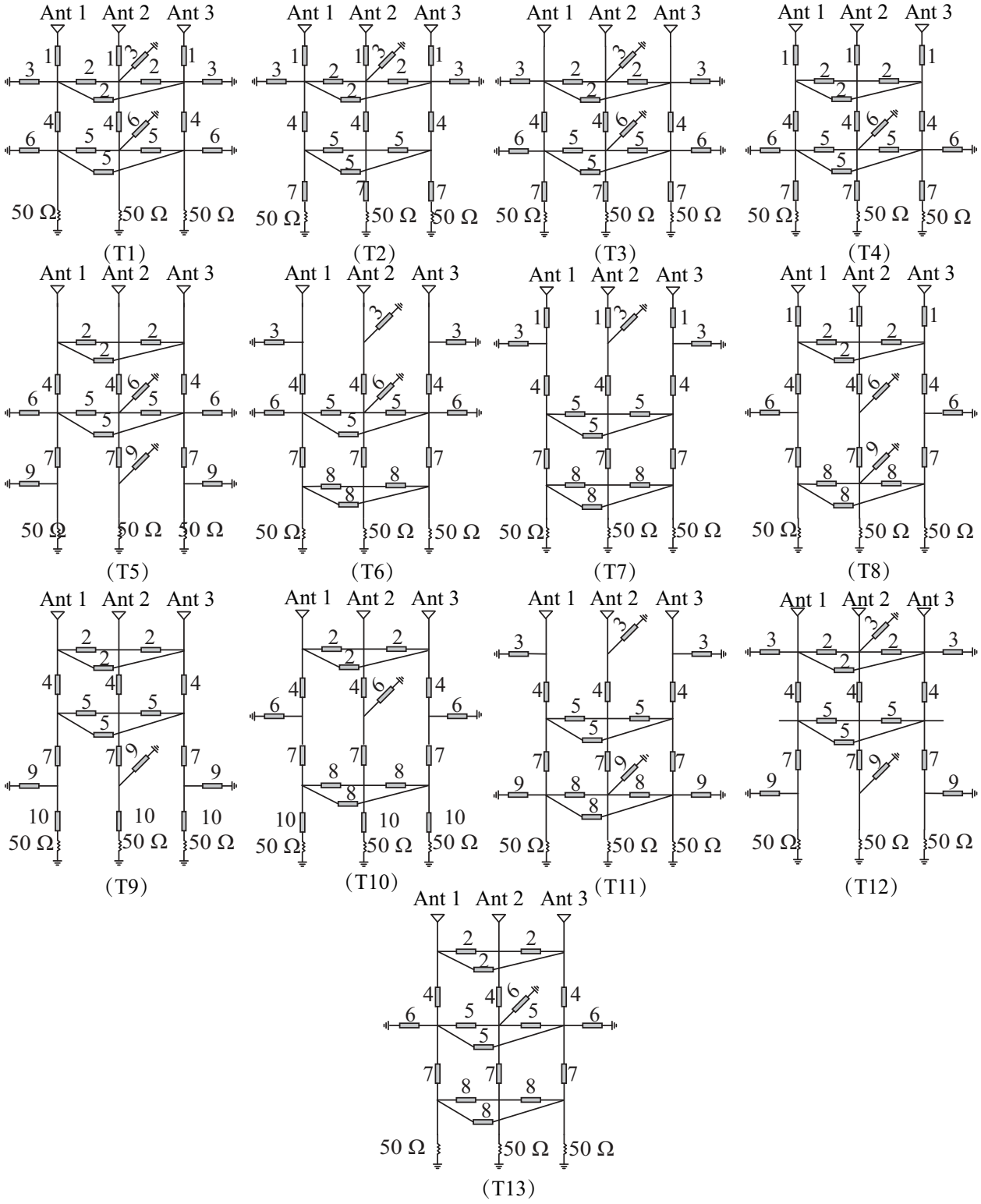

Figure 4.4: 13 unique topologies for implementing the DMN for a three-element antenna array. These topologies have the minimum number of reactive elements (six) needed to satisfy the DMN design conditions.

4.2.4 Design Example

First, we fabricated a three-element monopole array consisting of three 110 mm long monopole antennas positioned at the corners of an equilateral triangle whose side length is 5 cm as shown in Fig. 4.5. The monopole antennas are made of solid copper tubes with a circular cross section with the radius of 3 mm and mounted on a brass ground plane with physical dimensions of 43 cm $\times$ 43 cm.

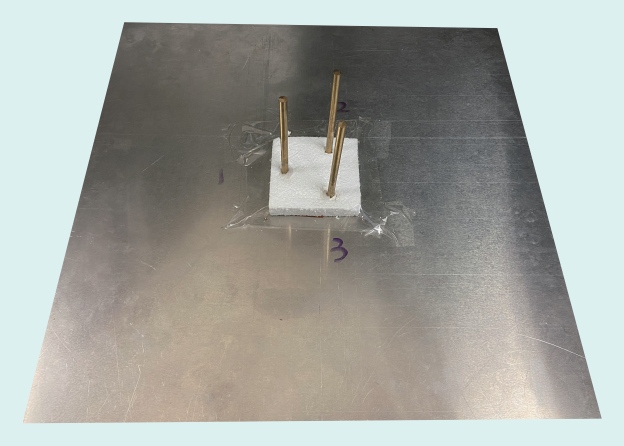

Figure 4.5: Photographs of the fabricated three-element center-symmetric monopole antenna array.

We measured the scattering parameters of the three-port antenna array using a vector network analyzer (Agilent N5225A). We observed that the resonant frequency of the antennas in the array is around 600 MHz and extracted the impedance matrix of the array at this frequency to design the external matching and decoupling network. The impedance matrix of the array, measured through this process is:

$$[Z] = \begin{bmatrix} 20.062 + j2.728 & 16.686 - j28.89 & 17.173 - j29.623 \\ 16.686 - j28.89 & 20.208 + j2.272 & 17.144 - j29.833 \\ 17.144 - j29.623 & 17.144 - j29.832 & 21.235 + j1.318 \end{bmatrix}. \tag{4.10}$$

where the numbers are in units of Ohms (Ω). According to (4.4) and (4.5), we can calculate the input impedances, seen at the inputs of the equivalent circuits of the coupling network,

in the common mode as $Z_{in,A}$ = 54.48+j56.79 Ω and in the differential mode as $Z_{in,B}$ = 3.51-j31.55 Ω by averaging the value of Z_{11} and Z_{12}. Using (4.6) and (4.7), we can determine S_{11} and S_{12}:

$$S_{11} = \frac{1}{3} \cdot \frac{3Z_{in,\ A}Z_{in,\ B} - Z_{in,\ A}Z_0 + Z_{in,\ B}Z_0 - 3Z_0^2}{(Z_{in,\ A} + Z_0)(Z_{in,\ B} + Z_0)} = -0.171 - j0.411, \tag{4.11}$$

$$S_{12} = \frac{2}{3} \cdot \frac{(Z_{in,\ A} - Z_{in,\ B})Z_0}{(Z_{in,\ A} + Z_0)(Z_{in,\ B} + Z_0)} = 0.216 + j0.406. \tag{4.12}$$

Besides the lossless condition and maximum power transfer condition, we need to add another constraint to this system of equations because as it stands the system is under-determined (i.e., we have more variables than constraints). Therefore, we choose an additional constraint and select the phase difference between the output voltages in Mode A and Mode B equals to 45° as $\angle V_{oa} - \angle V_{ob} = 45°$. This is an arbitrary condition and is added to allow for solving the system of 7 equations 8 unknowns. This way, the element values of the scattering matrix of the DMN can be calculated analytically. After introducing this condition, we have eight equations to solve for the real and imaginary parts of S_{14}, S_{15}, S_{44}, and S_{45}, which can be solved by MATLAB directly. The calculated S-matrix of the six-port network is shown in (4.13). To verify that the DMN matches and decouples the antenna array, we calculate the S-parameters of the three-port network after cascading the antenna array with the DMN according to (4.10), (4.13), and (4.17) to (4.21). The S-matrix of the antenna array $[S_{antenna}]$ can be transformed from the Z-matrix as shown in (4.10). $[S_{total}]$ ends up being equal to zero, which means that the DMN we calculated in the previous steps can match and decouple the antenna array.

$$[S] = \begin{bmatrix} -0.171-j0.411 & 0.216+j0.406 & 0.216+j0.406 & 0.263+j0.509 & 0.116+j0.108 & 0.116+j0.108 \\ 0.216+j0.406 & -0.171-j0.411 & 0.216+j0.406 & 0.116+j0.108 & 0.263+j0.509 & 0.116+j0.108 \\ 0.216+j0.406 & 0.216+j0.406 & -0.171-j0.411 & 0.116+j0.108 & 0.116+j0.108 & 0.263+j0.509 \\ 0.263+j0.509 & 0.116+j0.108 & 0.116+j0.108 & 0.0646+j0.452 & -0.171-j0.421 & -0.171-j0.421 \\ 0.116+j0.108 & 0.263+j0.509 & 0.116+j0.108 & -0.171-j0.421 & 0.0646+j0.452 & -0.171-j0.421 \\ 0.116+j0.108 & 0.116+j0.108 & 0.263+j0.509 & -0.171-j0.421 & -0.171-j0.421 & 0.0646+j0.452 \end{bmatrix}. \quad (4.13)$$

$$\begin{aligned} [S_{total}] &= \begin{bmatrix} S_{44} & S_{45} & S_{45} \\ S_{45} & S_{44} & S_{45} \\ S_{45} & S_{45} & S_{44} \end{bmatrix} + \begin{bmatrix} S_{14} & S_{15} & S_{15} \\ S_{15} & S_{14} & S_{15} \\ S_{15} & S_{15} & S_{14} \end{bmatrix} \times ([S_{antenna}]^{-1} - \begin{bmatrix} S_{11} & S_{12} & S_{12} \\ S_{12} & S_{11} & S_{12} \\ S_{12} & S_{12} & S_{11} \end{bmatrix})^{-1} \times \begin{bmatrix} S_{14} & S_{15} & S_{15} \\ S_{15} & S_{14} & S_{15} \\ S_{15} & S_{15} & S_{14} \end{bmatrix} \\ &= [0]. \end{aligned} \quad (4.14)$$

Subsequently, we calculated the S-matrix of Mode A and Mode B separately and transformed the S-matrix to two transmission matrices using the equations provided in [23] (page 192), which are shown in (4.15) and (4.16), respectively. We chose topology T2 (shown in Fig. 4.4) to demonstrate this new synthesis process for convenience, since its is compact and easy to fabricate. The equivalent circuit model of the three-element antenna array along with the DMN in Mode A and Mode B are shown in Fig. 4.6.

$$[ABCD_{mode,\ A}] = \begin{bmatrix} 1.187 & -j46.49 \\ -j0.0005 & 0.0959 \end{bmatrix}, \quad (4.15)$$

$$[ABCD_{mode,\ B}] = \begin{bmatrix} -1.302 & -j100.59 \\ -j0.0478 & 2.292 \end{bmatrix}. \quad (4.16)$$

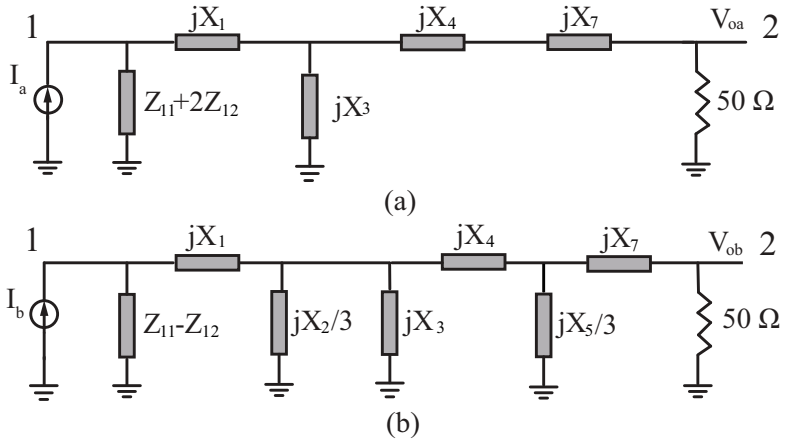

Figure 4.6: The equivalent circuit model of the DMN for the three-element antenna array using the coupling network of Topology 2 in the (a) Mode A and (b) Mode B of excitation.

The transmission matrices in both modes of excitation were written as functions of six reactive elements, X_1, X_2, X_3, X_4, X_5, and X_7 (See (E.1) to (E.11) in Appendix E for details). We calculated the transmission matrices for both modes using the equivalent circuit model in Fig. 4.6 by the equations provided in [97] (pp. 190). By matching the rewritten matrices to the ones shown in (4.15) and (4.16), we arrived at a nonlinear system of six independent equations with six variables. Solving these equations yields the reactance values for the coupling networks, which are listed in Table 4.1. All these values are for the ideal DMN without any connecting transmission lines and other influences. We solved these equations by using the equations and systems solver in MATLAB.

Table 4.1: Reactance values for the components of the external coupling network shown in Fig. 4.6 (in Ω).

X_1	-9.813
X_2	-116.698
X_3	52.457
X_4	-76.966
X_5	83.339
X_7	29.538

4.2.5 Experiments and Measurement Results

We fabricated the DMN corresponding to the S-matrix as calculated in Section 4.2.3. The simulated layout of the DMN is shown in Fig. 4.7. The front of the board shown in Fig. 4.7(a) shows the structure of the DMN, which includes the lumped elements and the connecting transmission lines. Port 1 to Port 3 are the input ports of the DMN connected to the antenna array, while Port 4 to Port 6 are the output ports. Furthermore, in order to connect the DMN to the output ports of the circuit and simply the layout of the whole circuit, we used three 50 Ω coplanar waveguide in the back of the board as shown in Fig. 4.7(b) from point A to point B. And point B is connected to the the output ports by 50 Ω transmission lines. Both of the coplanar waveguide and the transmission lines with a characteristics impedance of 50 Ω will not influence the output reflection coefficients.

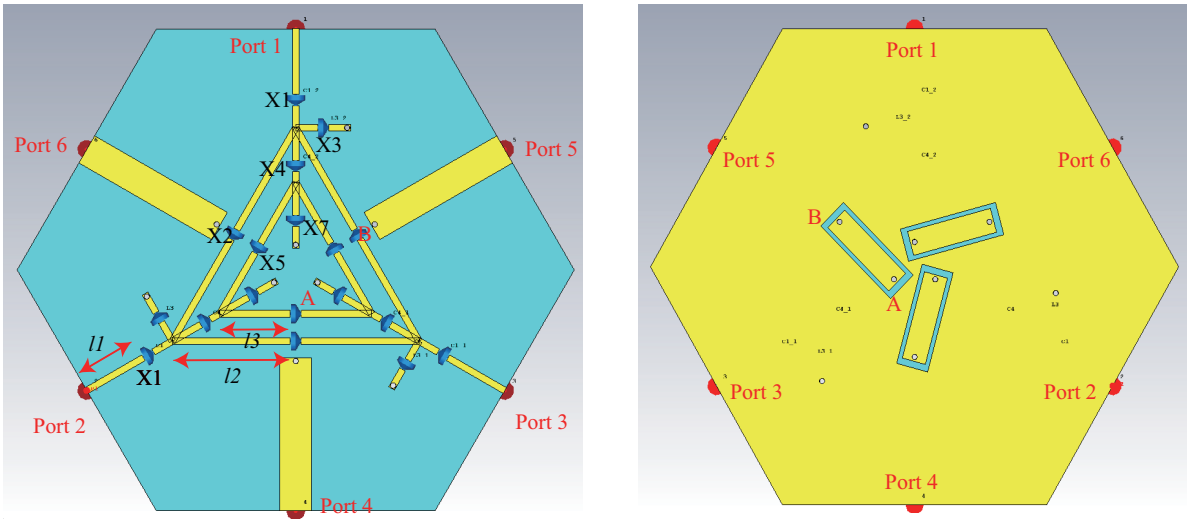

Figure 4.7: The simulated DMN model in CST studio (a) Front (b) Back.

Besides, when calculating the realistic lumped element values for the fabrication, we took the the series inductance and shunt capacitance of the transmission lines into consideration by using its generalized lumped-element model. All the transmission lines are modeled in this way, especially the three sets of transmission lines, which are the connecting transmission

lines for X1, X2, and X5, labeled as l_1 to l_3, respectively (See Appendix E for details). Furthermore, the generalized lumped-element model is not accurate enough and we found the simulation results still have some frequency shift. Thus, we tuned all the calculated lumped element values by 20% and optimized in CST solver in order to finalize the set of values which will minimize the influence of all the transmission lines. The original calculated values, the after-tuned values and the closet commercial available values chosen in the fabrication are shown in Table 4.2. The DMN was implemented on FR4 substrates with a dielectric constant of $\epsilon_r = 4.4$ and thickness of 0.6 mm. The fabricated board is shown in Fig. 4.8.

Table 4.2: Values of the lumped elements calculated, after-tuned and used in the fabrication.

Position	Calculated	After-tuned	Used
X_1	16.36 pF	13.13 pF	13 pF
X_2	1.415 pF	1.14 pF	1.1 pF
X_3	10.121 nH	11.22 nH	11 nH
X_4	3.06 pF	3.9 pF	3.8 pF
X_5	13.56 nH	15.3 nH	15 nH
X_7	4.39 nH	3.98 nH	3.9 nH

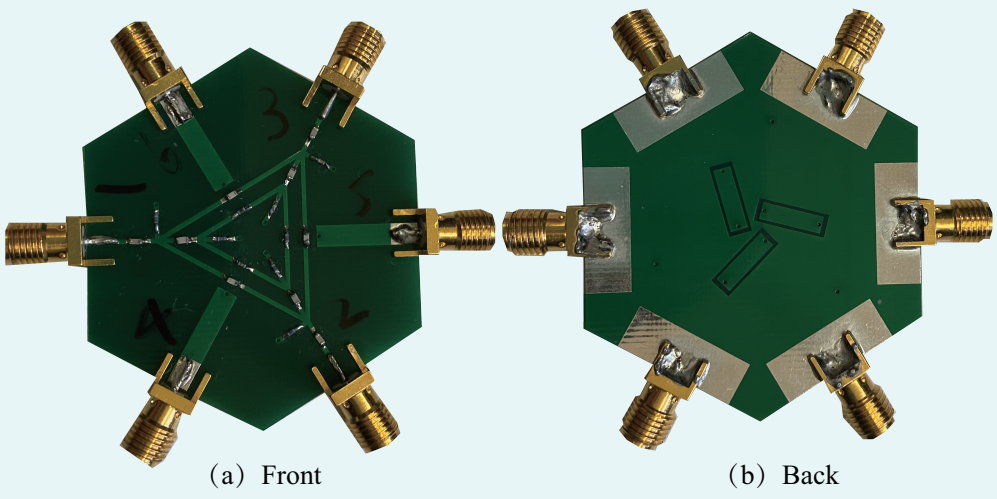

Figure 4.8: Photographs of the fabricated three-input three-output DMN.

Fig. 4.9 shows the S-parameters of the antenna array without the DMN compared with the measured and simulated S-parameters of the system with the DMN for all the three output ports separately. From the results we can see the DMN matched and decoupled the

original antenna array as desired. The center frequency of the resonance is shifted up in the measurement results compared to the simulation results by about 8 MHz. There are several reasons contributing to these frequency shifts. These include the fabrication tolerances of lumped elements and dielectric constant and loss tangent of the substrate. Besides, the slight asymmetry of the precise dimensions of the three monopoles in fabrication, small differences between the SMA adapters used to connect the three-element monopole array to the DMN also cause the shift. Additionally, the transmission line sections that connect the lumped elements of the decoupling networks which we calculated its influence by the RLC model are not 100% accurate. Despite these frequency shifts, the measured bandwidths agree quite well with the values predicted in the simulations.

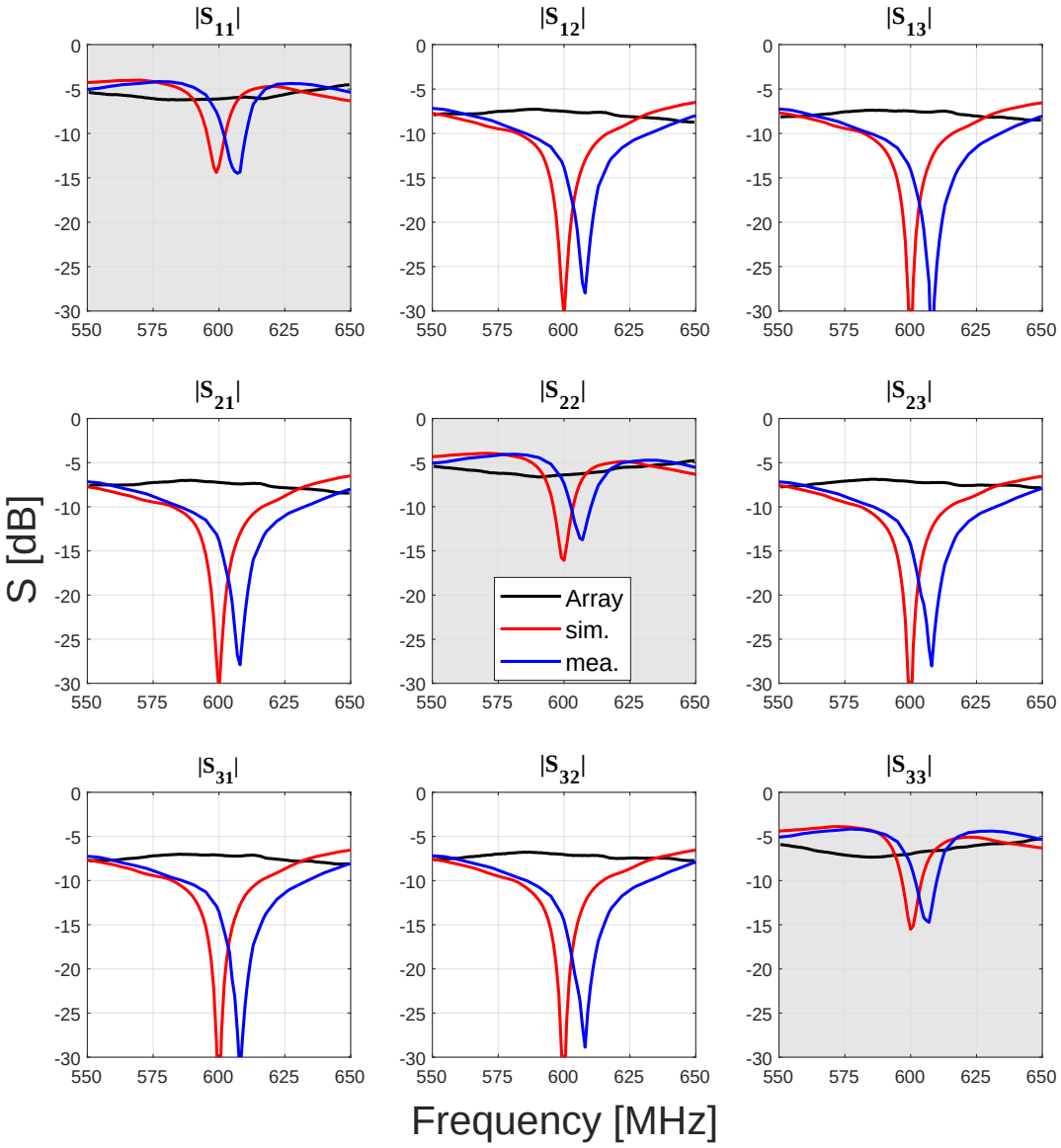

Figure 4.9: Measured and simulated output reflection coefficients of the antenna system.

4.3 Decoupling and Matching Network Design for A Linear Three-element Antenna Array

4.3.1 Deriving the S-matrix of the decoupling and matching network

Fig. 4.10 shows the block diagram of the system, which contains a three-element linear antenna array and an external decoupling and matching network. The voltages and currents on each of the ports of the DMN are decomposed into inward ($\bar{a}$) and outward ($\bar{b}$) traveling waves that satisfy the relation $\bar{b} = [S]\bar{a}$, where $[S]$ is the S-matrix of the DMN.

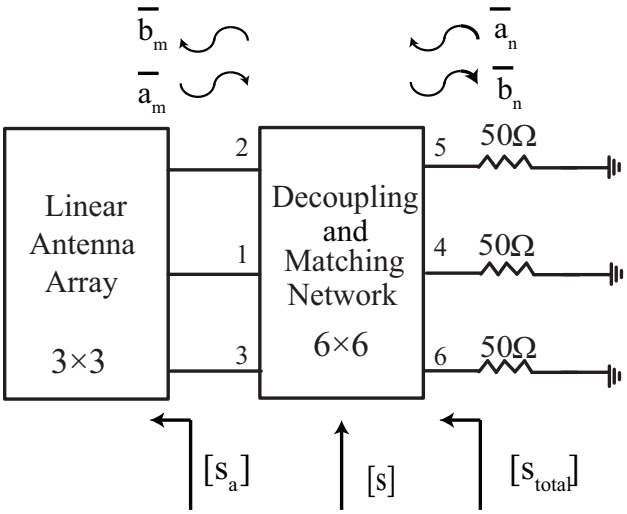

Figure 4.10: Network model of the three-element linear antenna array system

First, we formulate the S-matrix of the network with the assumptions that it is lossless, symmetric, and reciprocal. The S-matrix of the network satisfies the reciprocal condition $[S^T] = [S]$ and the lossless condition $[S][S]^H = [I]$, where $[S^T]$ and $[S^H]$ are the transpose and conjugate transpose of $[S]$, respectively. And the S-matrix of the network can be simply expressed in the form of submatrices as:

$$[S] = \begin{bmatrix} S_{mm} & S_{mn} \\ S_{nm} & S_{nn} \end{bmatrix}, \tag{4.17}$$

where m = 1, 2, 3, and n = 4, 5, 6, which represent the input and the output ports of the DMN, respectively. Thus, the relation $\bar{b} = [S]\bar{a}$ can be expended as:

$$\begin{bmatrix} \bar{b}_m \\ \bar{b}_n \end{bmatrix} = \begin{bmatrix} S_{mm} & S_{mn} \\ S_{nm} & S_{nn} \end{bmatrix} \times \begin{bmatrix} \bar{a}_m \\ \bar{a}_n \end{bmatrix}, \tag{4.18}$$

$\bar{a}_m$ and $\bar{b}_m$ can be related together using $\bar{a}_m = [S]\bar{b}_m$ where $[S_a]$ is the coupled S-parameter matrix measured at the antenna input ports.

From (4.18), we can have:

$$\bar{b}_m = [S_{mm}] \times \bar{a}_m + [S_{mn}] \times \bar{a}_n, \tag{4.19}$$

$$\bar{b}_n = [S_{nm}] \times \bar{a}_m + [S_{nn}] \times \bar{a}_n. \tag{4.20}$$

Then, we can calculate the $[S_{total}]$ based on $[S_a]$ and $[S]$ which represents the total S-matrix of the whole system after the DMN by combining (4.19) and (4.20):

$$\begin{aligned} [S_{total}] &= \frac{\bar{b}_n}{\bar{a}_n}|_{\bar{a}_m=0} \\ &= [S_{nn}] + [S_{nm}] \times ([S_a]^{-1} - [S_{mm}])^{-1} \times \ [S_{mn}]. \end{aligned} \tag{4.21}$$

By satisfying the decoupling and matching conditions, $[S_{total}]$ should be equal to [0].

Since the DMN is connected to a set of uncoupled identical loads of impedance Z_0, so that $\bar{a}_n = 0$ and the reflection coefficient from the input ports of the DMN is equal to $[S_{mm}]$. If we collapse the matching network and load network into a single network block, then our equivalent network is replaced by the collapsed network with input reflection coefficient $[S_{mm}]$. Based upon our work above and since the matching network is lossless, we know that

all available power will be transferred to the loads if and only if $[S_{mm}] = [S_a^H]$ [95].
If the whole system is matched and decoupled, $[S_{total}]$ should equal to [0]. Thus we can have:

$$[S_{nn}] = -[S_{nm}] \times ([S_a^{-1}] - [S_{mm}])^{-1} \times [S_{mn}]. \tag{4.22}$$

Thus, the sub-matrices of $[S]$, $[S_{nn}]$ can be expressed by $[S_{mm}]$, $[S_{mn}]$ or $[S_{nm}]$), these matrices can be calculated by applying the lossless condition of the network using singular value decomposition (SVD).

The SVD of the S-parameter matrices facilitates analysis and provides a useful interpretation for calculation the S-matrix of the DMN. This decomposition is given by $[S] = [U][\Lambda]^{1/2}[V]^H$, where $[U]$ and $[\Lambda]$ are unitary matrices of singular vectors, $[\Lambda]^{1/2}$ is a diagonal matrix of corresponding ordered singular values (largest to smallest), and $\{\cdot\}^H$ is the conjugate transpose operation. We may therefore write the S-matrix relation $\bar{b} = [S]\bar{a}$ as:

$$[U]^H\bar{b} = [\Lambda]^{1/2}[V]^H\bar{a}. \tag{4.23}$$

Using the lossless condition of the network ($[S][S]^H = [I]$), we have:

$$\begin{aligned}
&[S_{mm}]^H [S_{mm}] + [S_{nm}]^H[S_{nm}] = [I],\\
&[S_{mm}]^H[S_{mn}] + [S_{nm}]^H[S_{nn}] = [0],\\
&[S_{mn}]^H[S_{mn}] + [S_{nn}]^H[S_{nn}] = [I].
\end{aligned} \tag{4.24}$$

Substitution of the SVD of the subblocks $[S] = [U][\Lambda]^{1/2}[V]^H$ into (22) yield:

$$\begin{aligned}
&[V_{nm}]\,[\Theta_{nm}] = [V_{mm}]\\
&[\Lambda_{nm}] = [I] - [\Lambda_{mm}],\\
&[V_{mn}][\Theta_{mn}] = [V_{nn}],\\
&[\Lambda_{mn}] = [I] - [\Lambda_{nn}].
\end{aligned} \tag{4.25}$$

where $[\Theta_{nm}]$ and $[\Theta_{mn}]$ are diagonal phase shift matrices with arbitrary complex elements of unit magnitude. Equation (4.24) and (4.25) are used from [95] and are provided here for completeness of the calculation steps.

To make the calculation easier, we make $[\Theta_{nm}] = [I]$, thus $[V_{nm}] = [V_{mn}]$. Due to the symmetry and reciprocal conditions of the DMN, the sub-matrix $[S_{nm}]$ can be expressed as:

$$[S_{nm}] = \begin{bmatrix} S_{14} & S_{24} & S_{24} \\ S_{15} & S_{25} & S_{26} \\ S_{15} & S_{26} & S_{25} \end{bmatrix}. \tag{4.26}$$

Here, due to symmetry $S_{15} = S_{16}$, $S_{24} = S_{34}$, $S_{26} = S_{35}$, and $S_{25} = S_{36}$. Therefore, $[U_{nm}]$ can be chosen as any unitary matrices of singular vectors that follow the same symmetry and reciprocal conditions of $[S_{nm}]$. Thus, we can calculate $[S_{nm}]$ by choosing a $[U_{nm}]$ and using the existing values of $[\Theta_{nm}]$, and $[V_{nm}]$ as:

$$[S_{nm}] = [U_{nm}][\Theta_{nm}]^{1/2}[V_{nm}]^{H}. \tag{4.27}$$

4.3.2 Calculation example

We applied the calculation procedure presented in the previous section to calculate the S-matrix of a DMN for a three-element linear antenna array. The array consists of three monopole antennas that are 110 mm long, separated by 5 cm, and placed above a ground plane with a radius of 40 cm. We simulated the antenna array in CST Microwave Studio to extract its three-port S-matrix at 600 MHz, which will be used for calculation of the S-matrix of the external coupling network. The derived S-matrix of the antenna array is:

$$[S_a] = \begin{bmatrix} -0.464 + j0.256 & 0.409 - j0.129 & 0.409 - j0.129 \\ 0.409 - j0.129 & -0.27 + j0.271 & 0.0611 - j0.274 \\ 0.409 - j0.129 & 0.0611 - j0.274 & -0.27 + j0.271 \end{bmatrix}. \tag{4.28}$$

Based upon our work above, since the DMN is a matching network, $[S_{mm} = [S_a]^H$. The SVD of $[S_{mm}]$ can be expended as:

$$[U_{mm}] = \begin{bmatrix} -0.688 - j0.394 & 0 & -0.500 - j0.349 \\ 0.414 + j0.122 & 0.652 + j0.273 & -0.521 - j0.206 \\ 0.414 + j0.122 & -0.652 - j0.273 & -0.521 - j0.206 \end{bmatrix}, \tag{4.29}$$

$$[\Lambda_{mm}] = \begin{bmatrix} 0.993 & 0 & 0 \\ 0 & 0.4067 & 0 \\ 0 & 0 & 0.0672 \end{bmatrix}, \tag{4.30}$$

$$[V_{mm}] = \begin{bmatrix} 0.793 & 0 & -0.601 \\ -0.420 - j0.0995 & -0.572 + j0.416 & -0.545 - j0.129 \\ -0.420 - j0.0995 & 0.572 - j0.416 & -0.545 - j0.129 \end{bmatrix}. \tag{4.31}$$

Afterwards, we can calculate $[\Lambda_{nm}]$ and $[V_{nm}]$ based on the matrices above,

$$[\Lambda_{nm}] = [I] - [\Lambda_{mm}] = \begin{bmatrix} 0.007 & 0 & 0 \\ 0 & 0.5933 & 0 \\ 0 & 0 & 0.9328 \end{bmatrix}, \tag{4.32}$$

$$[V_{nm}] = [V_{mm}]. \tag{4.33}$$

In order to calculate the value of $[S_{nm}]$ from (4.27), we need to find a $[U_{nm}]$. $[U_{nm}]$ can be chosen as any unitary matrices of singular vectors that follow the same symmetry and reciprocal conditions of $[S_{nm}]$. Thus, we decompose a simple S-matrix as $[S_{svd}]$ as shown in (4.34) and use the SVD of it as the as the unitary matrices of singular vectors $[U_{nm}]$.

$$[S_{svd}] = \begin{bmatrix} 1+j2 & 2+j3 & 2+j3 \\ 3+j4 & 4+j5 & 5+j6 \\ 3+j4 & 5+j6 & 4+j5 \end{bmatrix}. \tag{4.34}$$

After the decomposition, $[U_{nm}]$ can be expressed as:

$$[U_{nm}] = \begin{bmatrix} -0.166-j0.286 & 0 & 0.833+j0.444 \\ -0.397-j0.537 & 0.617+j0.346 & -0.217-j0.0862 \\ -0.397-j0.537 & 0.617+j0.346 & -0.217-j0.0862 \end{bmatrix}. \tag{4.35}$$

Thus, we can calculate $[S_{nm}]$ by using the existing values of $[U_{nm}]$, $[\Lambda_{nm}]$, and $[V_{nm}]$ as:

$$\begin{aligned} [S_{nm}] &= [U_{nm}] \times [\Theta_{nm}]^{1/2} \times [V_{nm}]^H \\ &= \begin{bmatrix} -0.166-j0.286 & 0 & 0.833+j0.444 \\ -0.397-j0.537 & 0.617+j0.346 & -0.217-j0.0862 \\ -0.397-j0.537 & 0.617+j0.346 & -0.217-j0.0862 \end{bmatrix} \times \begin{bmatrix} 0.007 & 0 & 0 \\ 0 & 0.5933 & 0 \\ 0 & 0 & 0.9328 \end{bmatrix}^{1/2} \\ &\times \begin{bmatrix} 0.793 & 0 & -0.601 \\ -0.420-j0.0995 & -0.572+j0.416 & -0.545-j0.129 \\ -0.420-j0.0995 & 0.572-j0.416 & -0.545-j0.129 \end{bmatrix}^H \\ &= \begin{bmatrix} -0.501-j0.281 & -0.486-j0.121 & -0.486-j0.121 \\ 0.102+j0.0151 & -0.0177-j0.316 & 0.305+j0.384 \\ 0.102+j0.0151 & 0.305+j0.384 & -0.0177-j0.316 \end{bmatrix}. \end{aligned} \tag{4.36}$$

Since the whole system is decoupled and matched ($[S_{total}] = 0$), then we can calculate $[S_{nn}]$ using (4.22) as:

$$
\begin{aligned}
[S_{nn}] &= -[S_{nm}] \times ([S_a]^{-1} - [S_{mm}])^{-1} \times [S_{mn}] \\
&= \begin{bmatrix} -0.215 + j0.025 & 0.0795 + j0.233 & 0.0795 + j0.233 \\ 0.0795 + j0.233 & 0.184 + j0.734 & -0.0158 + j0.128 \\ 0.0795 + j0.233 & -0.0158 + j0.128 & 0.184 + j0.734 \end{bmatrix}.
\end{aligned} \tag{4.37}
$$

Thus, the S-matrix of the DMN can be combined as:

$$
\begin{aligned}
[S] &= \begin{bmatrix} S_{mm} & S_{mn} \\ S_{nm} & S_{nn} \end{bmatrix} \\
&= \begin{bmatrix} -0.464-j0.256 & 0.409+j0.129 & 0.409+j0.129 & -0.501-j0.281 & 0.102+j0.0151 & 0.102+j0.0151 \\ 0.409+j0.129 & -0.27-j0.271 & 0.0611+j0.274 & -0.486-j0.121 & -0.0177-j0.316 & 0.305+j0.384 \\ 0.409+j0.129 & 0.0611+j0.274 & -0.27-j0.271 & -0.486-j0.121 & .305+j0.384 & -0.0177-j0.316 \\ -0.501-j0.281 & -0.486-j0.121 & -0.486-j0.121 & -0.215+j0.025 & 0.0795+j0.233 & 0.0795+j0.233 \\ 0.102+j0.0151 & -0.0177-j0.316 & 0.305+j0.384 & 0.0795+j0.233 & 0.184+j0.734 & -0.0158+j0.128 \\ 0.102+j0.0151 & 0.305+j0.384 & -0.0177-j0.316 & 0.0795+j0.233 & -0.0158+j0.128 & 0.184+j0.734 \end{bmatrix}.
\end{aligned} \tag{4.38}
$$

The S-matrix of a matching and decoupling network for a three-element linear antenna array can be analytically calculated by following all these steps above.

4.3.3 Decoupling and matching network synthesis

After obtaining the S-matrix of the DMN, by using the multi-port conversions between S and Y parameters [96], [97]:

$$
[Y] = [G_0]^{-1} \cdot ([S][Z_0] + [Z_0]^*)^{-1} \cdot ([I] - [S]) \cdot [G_0], \tag{4.39}
$$

with

$$
\begin{aligned}
[G_0] &= diag\{g_1, ..., g_n, ..., g_N\}, \\
[Z_0] &= diag\{Z_1, ..., Z_n, ..., Z_N\},
\end{aligned} \tag{4.40}
$$

and $[I]$ is the identity matrix. $[G_0]$ and $[Z_0]$ are diagonal matrices (terms outside the diagonal are zero) where each term is related to a port reference impedance $[Z_n]$ as:

$$[G_n] = \frac{1}{\sqrt{|Re\{[Z_n]\}|}}, \tag{4.41}$$

where $Re\{[Z_n]\}$ represents the real part of $[Z_n]$. In our case, $[Z_n] = 50\ \Omega$ and we can get the Y-matrix of the DMN as:

$$[Y] = \begin{bmatrix} -0.0704j & 0.0357j & 0.0357j & -0.0076j & -0.0019j & -0.0019j \\ 0.0357j & -0.0701j & -0.0449j & -0.0546j & 0.0061j & 0.0246j \\ 0.0357j & -0.0449j & -0.0701j & -0.0546j & 0.0246j & 0.0061j \\ -0.0076j & -0.0546j & -0.0546j & -0.0765j & 0.0233j & 0.0233j \\ -0.0019j & 0.0061j & 0.0246j & 0.0233j & 0.0047j & -0.004j \\ -0.0019j & 0.0246j & 0.0061j & 0.0233j & -0.004j & 0.0047j \end{bmatrix}. \tag{4.42}$$

where the admittances are in Siemens (S). The admittance matrix $[Y]$ can be converted to an actual realization of the DMN in terms of capacitors and inductors. The admittance matrix can be input to solve the matrix form of Ohm's law, $[Y] * [V] = [I]$. In this instance V is a vector of the voltage at each node and I is the vector of corresponding currents. To realize the diagonal elements of $[Y]$, which are called the self-admittances at the nodes as $Y_{ij}|_{i=j}$, a shunt element at each port is necessary. The value of the ith shunt element is the sum over the ith row of $[Y]$, which means the sum of all the admittances terminating on the node identified by the repeated subscripts. The other off-diagonal element of $[Y]$ are the mutual admittances of the nodes as $Y_{ij}|_{i\neq j}$, and each equals the negative of the sum of all admittances connected directly between the nodes identified by the double subscripts. The topology of the DMN is depicted in Fig. 4.11. The network consists of 21 elements of capacitors and inductors. The values of the lumped elements are shown in the Table 4.3.

Table 4.3: Values of the lumped elements calculated in the DMN.

Port No.	1	2	3	4	5	6
1	2.74 pF	9.46 pF	9.46 pF	35.08 nH	141.00 nH	141.00 nH
2	9.46 pF	27.40 pF	5.90 nH	4.86 nH	1.62 pF	6.51 pF
3	9.46 pF	5.90 nH	27.40 pF	4.86 nH	6.51 pF	1.62 pF
4	35.08 nH	4.86 nH	4.86 nH	38.93 pF	6.18 pF	6.18 pF
5	141.00 nH	1.62 pF	6.51 pF	6.18 pF	4.70 nH	680.53 nH
6	141.00 nH	6.51 pF	1.62 pF	6.18 pF	680.53 nH	4.70 nH

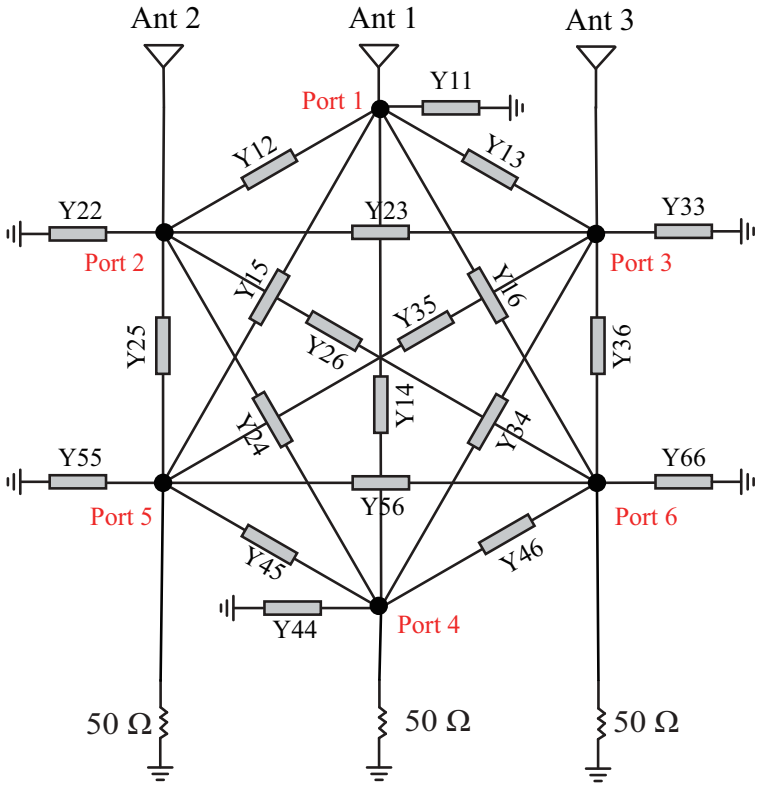

Figure 4.11: Topology of the DMN. Thick lines correspond to individual reactance.

We simulated this network in ADS with the ideal calculated lumped element values. Ports 1 to 3 are connected to the antenna array, which are the input ports of the network. Fig. 4.12 shows the simulated reflection coefficients seen at the output ports of the system (Ports 4, 5, and 6) with and without connecting to the DMN. Since the system is linearly symmetric and reciprocal, we only show four S-parameters out of 9 to represent its performance. Decoupling and matching are achieved simultaneously, albeit over a narrow band with a center frequency

at 600 MHz. The admittance matrix of the network will change a lot when the frequency shifts, which makes the network incapable of matching and decoupling the antenna array on a wide bandwidth based on our previous calculation.

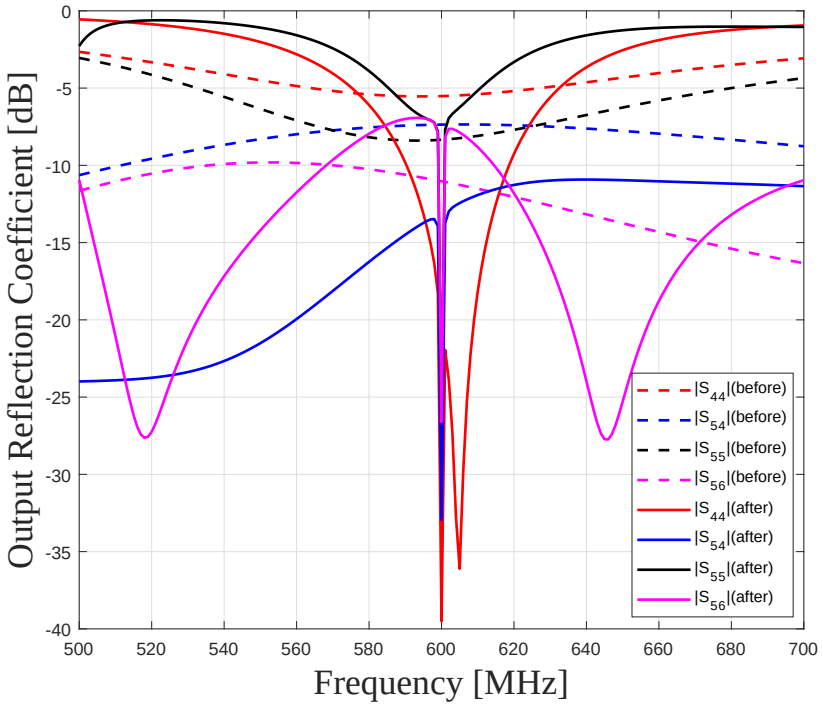

Figure 4.12: The S-parameters of the antenna array before and after using the decoupling network.

4.4 Conclusions

We presented a new procedure for synthesizing a decoupling and matching network for both center-symmetric and linear three-element antenna arrays. Using the approach reported in this chapter, we can determine the S-parameters of the DMN that can simultaneously impedance match and decouple the antennas and use them to synthesize the network.

For the center-symmetric case, the synthesis procedure starts with formulating and deriving a specific S-matrix for matching and decoupling the antenna array. Subsequently, the transmission matrices of the equivalent circuits of the network in the different eigenmodes

are calculated from the S-matrix and used to solve for the reactive element values of the network. By using the transmission matrices, we can reduce the number of equations and deduce that the network needs at least six reactive elements to realize these transmission matrices. We investigated all possible options for a symmetric six-port decoupling network consisting of lumped reactive elements from a generalized topology and identified 13 unique topologies that can be used to implement the DMN. A representative DMN prototype for a three-element, center-symmetric antenna array was designed, fabricated, and experimentally characterized. The performance of the system was evaluated by both simulations and measurements. Measurement results confirmed the results obtained from simulations and verified the validity of the proposed synthesis technique.

For the linear case, the analysis exploits singular value decomposition (SVD) of the scattering parameter matrix of the antenna and that of the matching network, this method is presented comprehensively in [95]. Using this process, we derive a specific S-matrix for the DMN to provide port decoupling and impedance match the antenna at the desired frequency of operation. We synthesized the network as a six-branched star network with capacitors and inductors. The elements values can be calculated by transforming the S-matrix of the DMN to the admittance matrix (Y-matrix). An antenna array with three 110 mm long monopoles, linearly separated by 5 cm, was simulated in CST Microwave Studio. Then, a detailed procedure to design a decoupling network for the antenna array at 600 MHz was presented. The simulation results show the network matches and decouples the antenna array and verified the synthesis method.

Chapter 5

Adaptive Matching and Decoupling Network for A Two-element Antenna Array

In this chapter, we will present a method for designing an adaptive matching and decoupling network (MDN) for a two-element antenna array. In doing so, we will use the analytic synthesis procedure for designing matching and decoupling networks that was presented in Chapter 3. The proposed adaptive matching and decoupling network includes a tunable matching network and a fixed decoupling network. The tunable matching network subsystem tracks the antenna impedance variations, and changes and adapts the element values of the impedance matching network to convert the input impedance of each antenna port to the same fixed impedance at a single frequency. This way, a fixed impedance matching and decoupling network can be used to match the overall system impedance to 50 Ω and decouple the two antenna ports. Such a system can successfully perform the tasks of impedance matching and decoupling of a two-element antenna system over a narrow bandwidth.

As a proof of concept demonstration, we examine a system with an asymmetric two-element antenna array consisting of one monopole antenna with a length of 225 mm and a top-hat loaded monopole antenna with a length of 140 mm, which is loaded with a circular shaped top hat with a diameter of 30 mm. The two monopoles are separated by 20 cm, and placed above a ground plane with dimensions of 60 cm $\times$ 60 cm. The two antennas were designed to operate at 300 MHz. A prototype of the antenna and that of the adaptive MDN were fabricated and experimentally characterized. Measurement results of the system show the capability of this adaptive MDN to perform antenna matching and decoupling in a changing antenna environment.

5.1 Introduction

Mutual coupling between elements has been a serious problem for multi-antenna systems. The antennas are usually supposed to be isolated from each other and considered as independent radiating elements. For arrays, mutual coupling may have adverse influence on the input impedance, gain, sidelobe level, and radiation pattern shape.

Antenna decoupling can be realized at two stages: propagation path and feed networks. Placing metallic partitions between antennas is a classical shielding method mentioned in electromagnetic compatibility text books [98], [99]. Following this idea, artificial magnetic conductors and electromagnetic bandgap surfaces are used to reduce the mutual coupling by setting up obstacles in the propagation path [100], [101]. Unfortunately, a very large metallic screen is required to achieve a high isolation ratio. Unlike the shielding idea, decoupling networks use feedback signal to cancel the coupling signal [102-104]. In this method, a higher isolation ratio is realized and space occupation is reduced. Although fairly good isolation is achieved, the methods reported are almost static, which means in a varying environment, they cannot maintain the same performance. This ideal operation condition is not met in many practical scenarios, such as a handset antenna system of a mobile device being held with different orientations at different distances from human body, or a vehicle-mounted antenna array experiencing changes in the surrounding environment during motion. Such changes in operating scenarios may substantially change the impedance matrix of the antenna system. This in turn will degrade the performances of the fixed MDNs resulting in the deterioration of the impedance matching and decreasing of the isolation levels. Therefore, a method that tracks the antenna array's impedance variation and provides adaptive matching and decoupling for the array elements is highly desirable for these application scenarios.

A few solutions have been presented to provide tunable decoupling for frequency reconfigurable mobile terminal antennas. These solutions rely on using tunable electromagnetic band-gap structures or spatial multiplexing of local elements to reconfigure the operating frequency range over which good impedance matching and high interelement isolation is achieved [34, 105-107]. These techniques are not readily applicable to provide the prescribed adaptive matching and decoupling operation due to the lack of impedance sensing and feedback control mechanism. Among different technology candidates existing in the literature for antenna decoupling, external decoupling networks are a sensible choice to be integrated with such adaptive systems. Moreover, for the previously reported adaptive matching net-

works [54-55, 57, 109], they only work with a single antenna and cannot be used to decouple the antenna array. In [58], the adaptive tuning for compensating antenna mismatch based on conjugate match is carried out by using L-networks and associated impedance measurements. However, this adaptive tuner has considerable limitations since an L-network can only achieve a conjugate match over half of the Smith chart even if the tuning ranges of the adjustable components cover all possible values of inductors and capacitors. In addition, the conjugate match in [58] limits flexibility in the antenna used with this adaptive tuning approach. In [109]-[112], these existing adaptive decoupling systems for two-element antenna arrays require multiple electronic devices as switches, bias trees, amplifiers, mixers or diodes, which will increase the complexity of the circuits. Besides, some techniques are also limit to symmetric antenna arrays. Thus it is desirable to develop an approach for designing decoupling networks with less complexity in implementation and avoiding the intermediate tuning states.

In this chapter, we present an adaptive matching and decoupling network (MDN) for two-element antenna arrays using an automatic impedance tuning circuit in conjunction with a fixed decoupling network. The system can track the variation in the antennas' impedances and update the matching network to maintain relatively constant impedances seen at the input of the decoupling network at the operating frequency. As a result, the two output ports of the decoupling network are matched to 50 Ω and decoupled regardless of the changes in the impedances of the antennas. The adaptive impedance tuning system consists of an impedance sensing unit connected to a control unit which feeds control signals to a tunable matching network. The impedance matrix of the two-element antenna array is derived from its transmission matrix which is calculated using the measured transmission signal voltages and currents at the input and output ports of the matching network. The complex input-to-output voltage ratio is measured by using a closed-loop system consisting of logarithmic amplifiers, voltage comparators, phase detectors and a microcontroller. The measured magnitude and phase values are digitized and sent to a microprocessor, which uses

the acquired data to calculate the antennas impedances and changes the control signals for adjusting the components' values in the tunable matching network. The two-port network seen at the output of the adaptive tuning section is symmetric and has a relatively constant impedance matrix at the intended operating frequency regardless of the antennas' input impedances. We used the method reported in Chap 3 to synthesize the fixed matching and decoupling network stage of the proposed adpative MDN. More details on the system design, simulations and experimental characterization of the proposed adaptive MDN will be shown and discussed in the following sections.

5.2 System Description

The block diagram of the proposed adaptive matching and decoupling network system is shown in Fig. 5.1. The system consists of an impedance sensing system, a tunable matching network, and a fixed decoupling network.

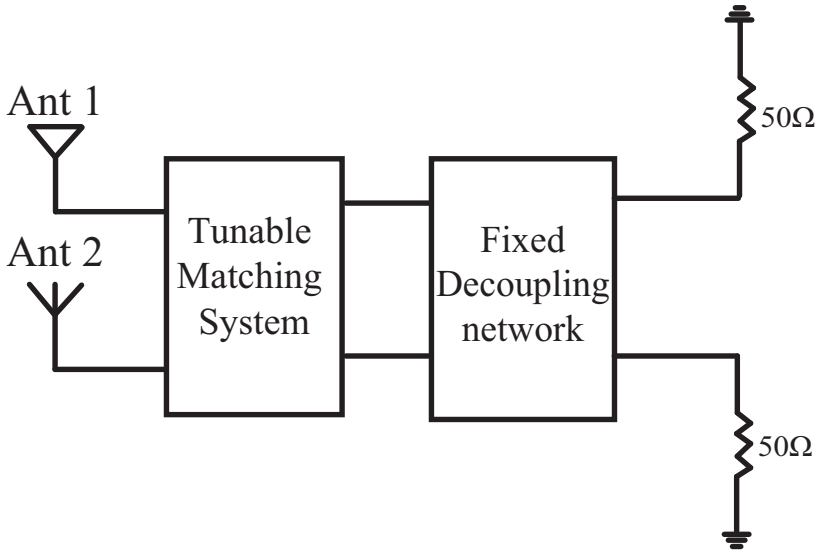

Figure 5.1: Block diagram of the adaptive MDN system.

The impedance sensing system consists of capacitive voltage dividers, phase and gain detectors (PGD) and a mircocontroller connecting to the computer. The block diagram is

shown in Fig. 5.2. The input impedance of the log amplifiers must be high enough to limit the power losses at the input and output ports of the tunable matching network. This may be implemented by using a high input impedance operational amplifier or a high impedance passive divider.

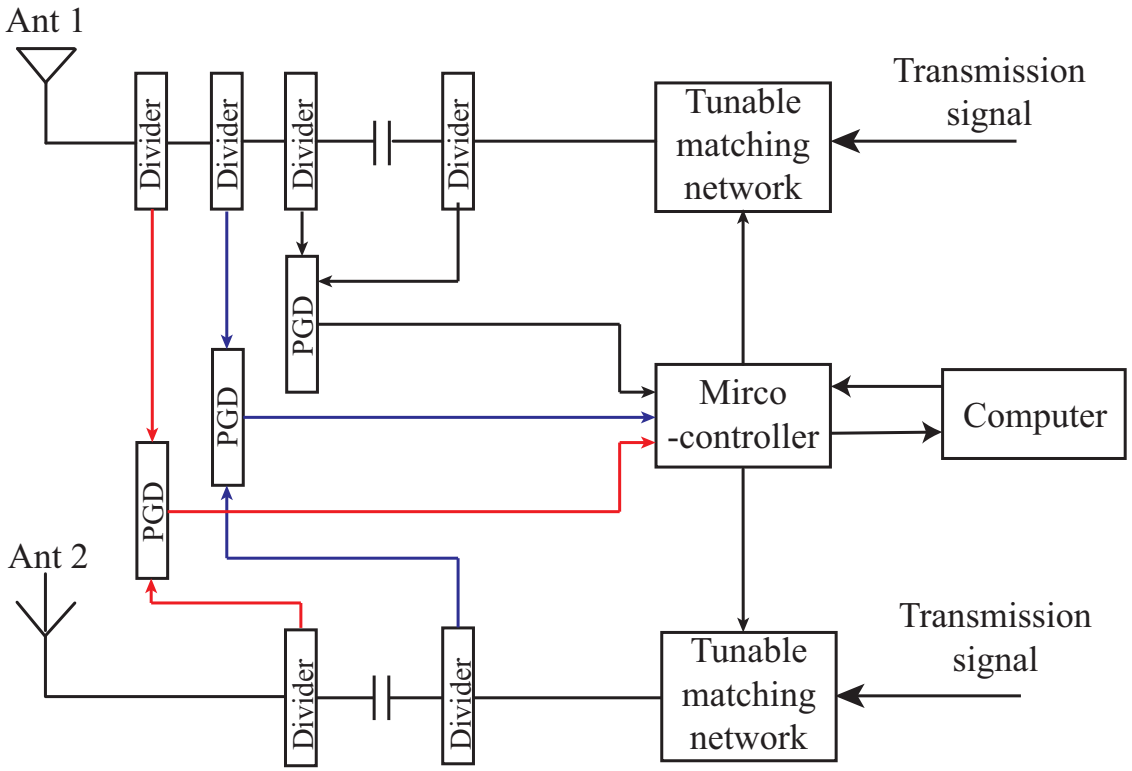

Figure 5.2: Block diagram of the adaptive impedance sensing sub-system of the proposed adaptive matching and decoupling network.

The Z-matrix of the antenna array can be transformed from its transmission matrix, which calculated by measuring transmission signal voltages and currents at the antenna ports. Fig. 5.3(a) shows the detailed measurement circuits consists of two capacitors as C1 and C2 and three PGDs. From the circuit by using the definition of transmission matrix, we can have:

$$\begin{bmatrix} V_{out2} \\ I_2 \end{bmatrix} = \begin{bmatrix} A & B \\ C & D \end{bmatrix} \begin{bmatrix} V_{out1} \\ I_1 \end{bmatrix}. \tag{5.1}$$

where A, B, C, and D is the transmission parameters of the antenna array. V_{out1} and V_{out2}

are the voltages at the two antenna ports. Then we normalized the matrix to V_{out1} and get:

$$\begin{bmatrix} \frac{V_{out2}}{V_{out1}} \\ \frac{I_2}{V_{out1}} \end{bmatrix} = \begin{bmatrix} A & B \\ C & D \end{bmatrix} \begin{bmatrix} 1 \\ \frac{I_2}{V_{out1}} \end{bmatrix}. \tag{5.2}$$

where I_1 and I_2 are the currents at the two antenna ports. From Ohm's law, we can have $I_1 = \frac{V_{in1}-V_{out1}}{Z_1}$ and $I_2 = \frac{V_{in2}-V_{out2}}{Z_2}$, where Z_1 and Z_1 are the impedances of C1 and C2 respectively. After the normalization, we can have:

$$\begin{bmatrix} \frac{V_{out2}}{V_{out1}} \\ \frac{\frac{V_{in2}}{V_{out1}} - \frac{V_{out2}}{V_{out1}}}{Z_2} \end{bmatrix} = \begin{bmatrix} A & B \\ C & D \end{bmatrix} \begin{bmatrix} 1 \\ \frac{\frac{V_{in1}}{V_{out1}} - 1}{Z_1} \end{bmatrix}. \tag{5.3}$$

The input to output complex voltage ratio $\frac{V_{in2}}{V_{out1}}$ and $\frac{V_{in1}}{V_{out1}}$, the output to output complex voltage ratio $\frac{V_{out2}}{V_{out1}}$ can be measured by using log amplifiers, a voltage comparator, and a phase detector, as depicted on Fig. 5.3(b). The measured magnitude and phase are then digitized and sent to a microcontroller for computations. The function of the ADC is to acquire data from PGD, transform the analog signal to digital, which is an integrated part of the microcontroller. The mircocontroller sends the data to computer using serial communications for computation.

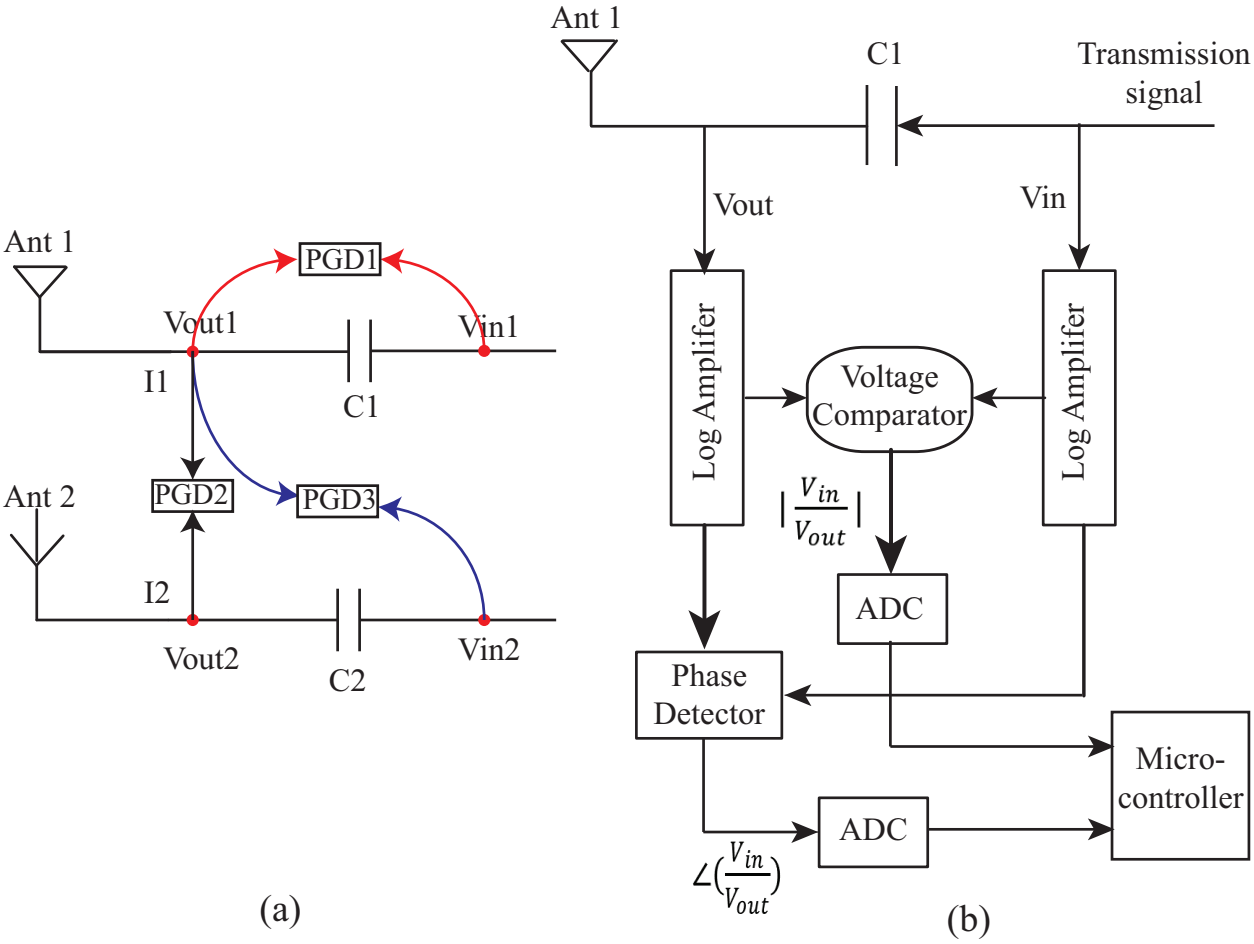

Figure 5.3: (a) Impedance measurement circuits. (b) Voltage acquisition connection.

The adaptive matching network consist of two tunable matching networks, each of which is in the form of a π-shaped circuit as shown in Fig 5.4. An ideal tunable low-pass π-network topology is shown in Fig. 5.4(a) using a tunable inductor and two tunable capacitors. These two networks convert the asymmetric 2×2 Z-matrix of the antenna array to a symmetric 2 Z-matrix seen at the outputs of the adaptive impedance matching sections.

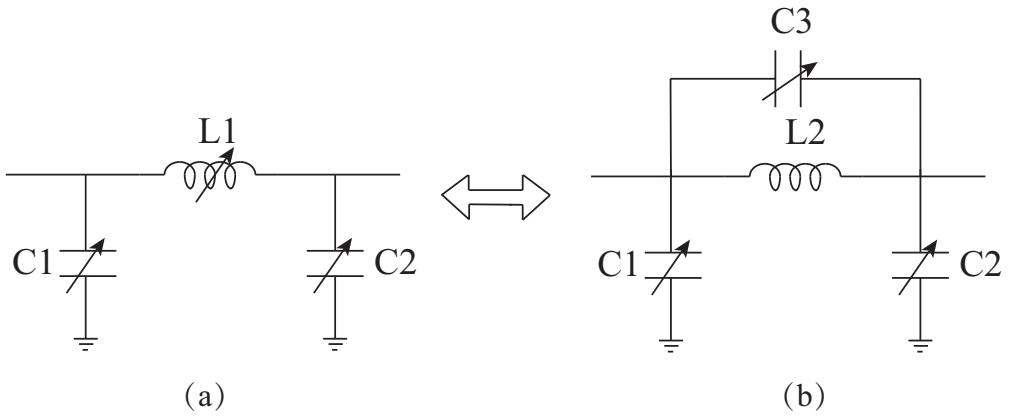

Figure 5.4: The block diagram of the tunable matching network.

Using this impedance matching network, it is possible in principle to convert any impedance to any other impedance. In practice, however, the range of impedances that can be matched to a desired value is limited by the tuning range of the tunable components used in the impedance matching network. In this case, since high-quality tunable inductors are not available, a fixed inductor is used in parallel with a tunable capacitor to change the effective inductance value in the series branch. A practical π-network tuner consisting of tunable capacitors may be implemented as shown in Fig. 5.4(b). As a result, the series equivalent inductance value is determined by:

$$L_1 = \frac{L_2}{1 - \omega^2 L_2 C_3}. \tag{5.4}$$

L_1 represents the equivalent inductor of the parallel combination of L_2 and C_3. To obtain a desired equivalent L_1 inductance for a fixed L_2 at a given frequency ω, the required C_3 can be derived from (4) as:

$$C_3 = \frac{L_1 - L_2}{\omega^2 L_1 L_2}. \tag{5.5}$$

After the tuning network, the S-matrix of the two-element antenna array will be symmetric at the intended operating frequency. Then we connect a fixed (no-tunable) network

to match and decouple the system as shown in Fig. 5.1. For synthesizing the fixed external decoupling network, we will use the method that we demonstrated in Chap 3. The network is designed to transform the load impedances to conjugate match the impedances of the antenna array in the common and differential modes of excitation. To synthesize the fixed decoupling network, we use the same as we shown in Chap 3. We first formulate and derive a 4×4 S-matrix which can decoupled the two ports after the tunable matching network at the intended operating frequency. Subsequently, we will use one of the implementations of a lossless, symmetric, and reciprocal four-port decoupling networks in Fig. 3.3 to synthesize the desired S-matrix. Then, we will present an analytic method for determining the values of the reactive elements constituting each network.

5.3 Implementation of Prototype ADMN System

As shown in Figs. 5.2 and 5.3, the impedance sensing system consists of capacitive voltage dividers, phase and gain detectors (PGD), two capacitors (C1 and C2) and a mircocontroller connecting to the computer. The composite input impedance of the log amplifiers must be high enough to limit power losses at the input and output ports of the matching network relative to the power in the main transmission path. This is implemented by using or a high impedance passive divider. The dividers consist of two capacitors with values of 1 pF and 6 pF in our prototype. Three AD8302 PGDs from Analog Devices are chosen with a 60 dB input power dynamic range from 60 to 0 dBm. The accurate gain and phase measurement scaling are 0.5 dB and 1°, respectively. Six analog to digital converter (ADC) channels of a STM32F407 high-performance microcontrollers from STMicroelectronics are used for the magnitude and phase digitization.

The tunable matching network as shown in Fig. 5.4(b) consists of a 10 nH series inductor (L2) and three tunable capacitors (C1, C2, and C3). The digitally tunable capacitors chosen in this design are PE64102 from pSemi, which offer a linear capacitance change versus

tuning state from 1.88 pF to 14.0 pF in discrete 391 fF steps. The values of the PE64102 are controlled through the SPI compatible 8-bit serial interface generated by the microcontroller.

The fabricated board showing the complete system is shown in Fig. 5.5 and the circuit diagram of that is shown in Fig. 5.6. The layout of the board is designed by Altium Designer and implemented on an FR4 substrate with a permittivity of 4.7, loss tangent of 0.018, and a thickness of 0.6 mm.

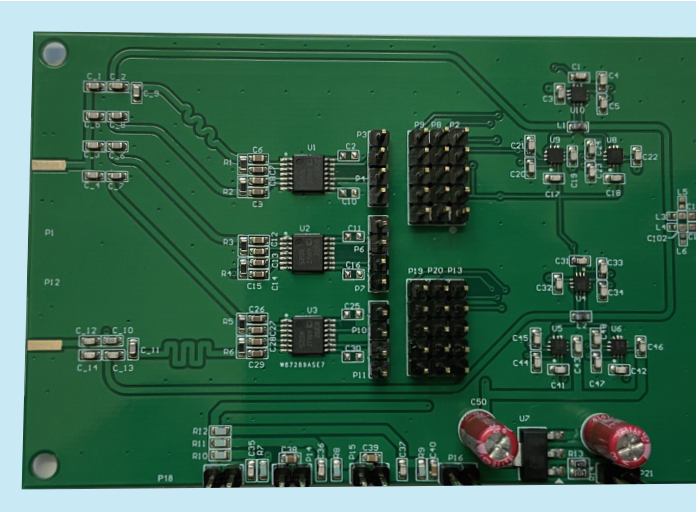

Figure 5.5: Photograph of the fabricated board.

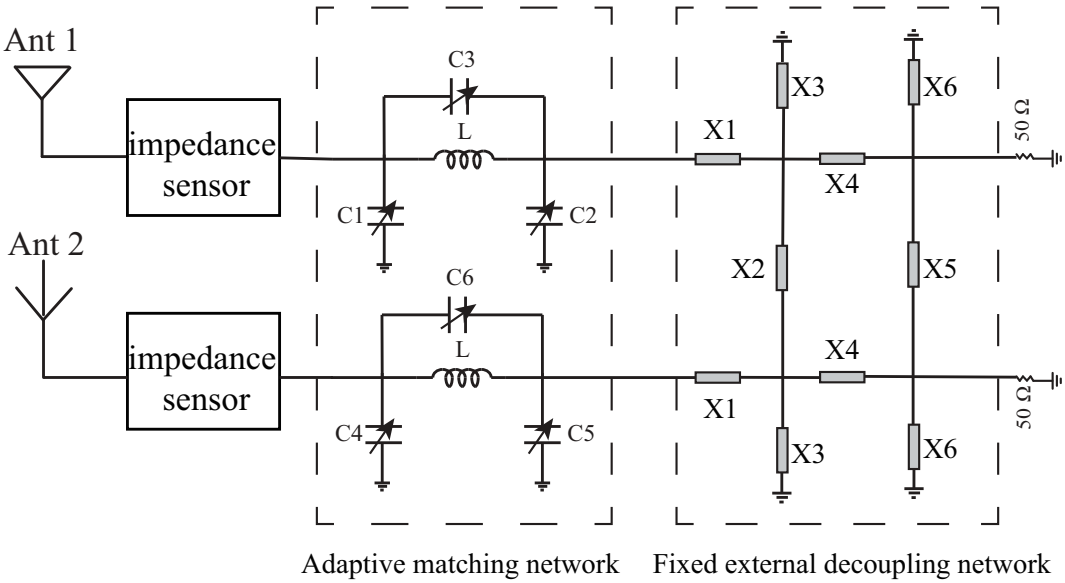

Figure 5.6: Circuit diagram of the fabricated board.

5.4 Experiments and Measurement Results

We examine the system with an asymmetric two-element antenna array as shown in Fig. 5.7. The array consists of one monopole antenna with a length 225 mm and a top-hat loaded monopole antenna. The dimensions for the diameter of the top hat and height of the monopole are 30 mm and 140 mm, respectively. The two antennas are separated by 20 cm, and placed above a ground plane with an area of 60 cm $\times$ 60 cm. The changing in the environment is mimicked by two copper blocks. Block 1 has a dimension of 200 $\times$ 50 $\times$ 150 mm and Block 2 has a dimension of 500 $\times$ 50 $\times$ 100 mm. The antenna array and the blocks are shown in Fig. 5.7.

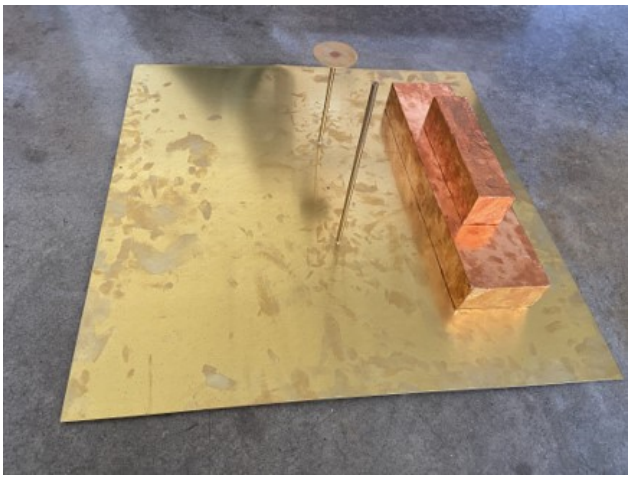

Figure 5.7: Photographs of the fabricated antenna array and the blocks.

In order to calculate the elements' values in the fix decoupling network before fabrication, we need to measure the S-parameters of the fabricated antenna array and have the full-wave simulation results of the board by using ADS Momentum. The S-matrix of the two-element antenna array was measured by using a vector network analyzer (Agilent N5225A). We observed that the resonant frequency of the antennas in the array is around 300 MHz and extracted the S-matrix of the array at this frequency to design the following networks. The S-matrix is:

$$[S] = \begin{bmatrix} 0.148 - j0.272 & 0.121 - j0.308 \\ 0.119 - j0.308 & 0.209 - j0.426 \end{bmatrix}. \tag{5.6}$$

We combined the S-matrix of the antenna array with only the simulated impedance sensing sub-system of the board in ADS to get the new S-matrix of the system before the tunable matching network. The new S-matrix before the adaptive matching network is:

$$[S_{new}] = \begin{bmatrix} -0.211 + j0.512 & -0.034 + j0.287 \\ -0.033 + j0.288 & -0.311 + j0.395 \end{bmatrix}. \tag{5.7}$$

The next step is to find the values of the digitally tuned capacitors to make the two-port network seen at the output of the adaptive tuning section symmetric at 300 MHz. We chose the median value of the capacitor 7.745 pF to be the original values of capacitors connecting Antenna 1 (C1, C2 and C3) and only tuned the values of the other three (C4, C5 and C6). By tuning the values of C4, C5, and C6, the two-port network before the fixed decoupling network was symmetric. The new symmetric Z-matrix at 300 MHz is:

$$[Z] = \begin{bmatrix} 26.9227 - j58.9722 & 8.1424 + j6.3115 \\ 8.1424 + j6.3115 & 26.9227 - j58.9722 \end{bmatrix} \Omega. \tag{5.8}$$

The elements' values of X1 to X6 in the fixed decoupling network were calculated according to this Z-matrix using the approach discussed in Chapter 3. The reactance values for the components are shown in Table 5.1.

Table 5.1: Reactance values for the components of the fixed external coupling network shown in Fig. 5.6 (in Ω).

X_1	-0.791
X_2	9.637
X_3	35.636
X_4	15.788
X_5	58.486
X_6	19.916

The performance of the system was evaluated by placing block 2 around the antenna array to mimic the changing in the environment. The S-parameters of the system before and after the changing are shown in Fig. 5.8. The S-parameters of the antenna array at 300 MHz before and after the changing were automatically calculated by the impedance sensing system. The values of the digitally tuned capacitor were updated by the microcontroller after calculating from the computer. The detailed calculating steps can be seen in Appendix F. The values of the capacitors in the adaptive matching networks before and after the changing of environment are shown in Table 5.2.

Table 5.2: Values of the tunable capacitors in the adaptive network before and after the change in antenna system in pF

Capacitor	Before	After
C_1	7.745	3.835
C_2	7.745	10.091
C_3	7.745	9.700
C_4	9.309	5.399
C_5	7.354	8.136
C_6	12.046	1.880

From Fig. 5.8, we can see the system is matched and decoupled at its original state when there is no block around the antenna array as shown in both simulated and measured results in (a) and (b). When we put block 2 near to the antenna array, output reflection coefficients of the system changes, which Antenna 1 is not matched at 300 MHz any more in (c) simulated and (d) measured results. Besides, in the measurement results as shown in (d), the isolation between the two antennas reduces to around 19 dB, which is 26 dB previously. Afterwards, the system adaptively changes the digital tunable capacitors values according to the newly calculated Z-matrix of the antenna array by the impedance sensor unit. As shown in both (e) and (f), the system returns to a matched and decoupled condition.

There are several reasons contribute to the mismatches between simulation and measurements results. These include fabrication tolerances of the lumped elements, the SMA connectors and the cables connecting the antenna array to the board. Another issue is the

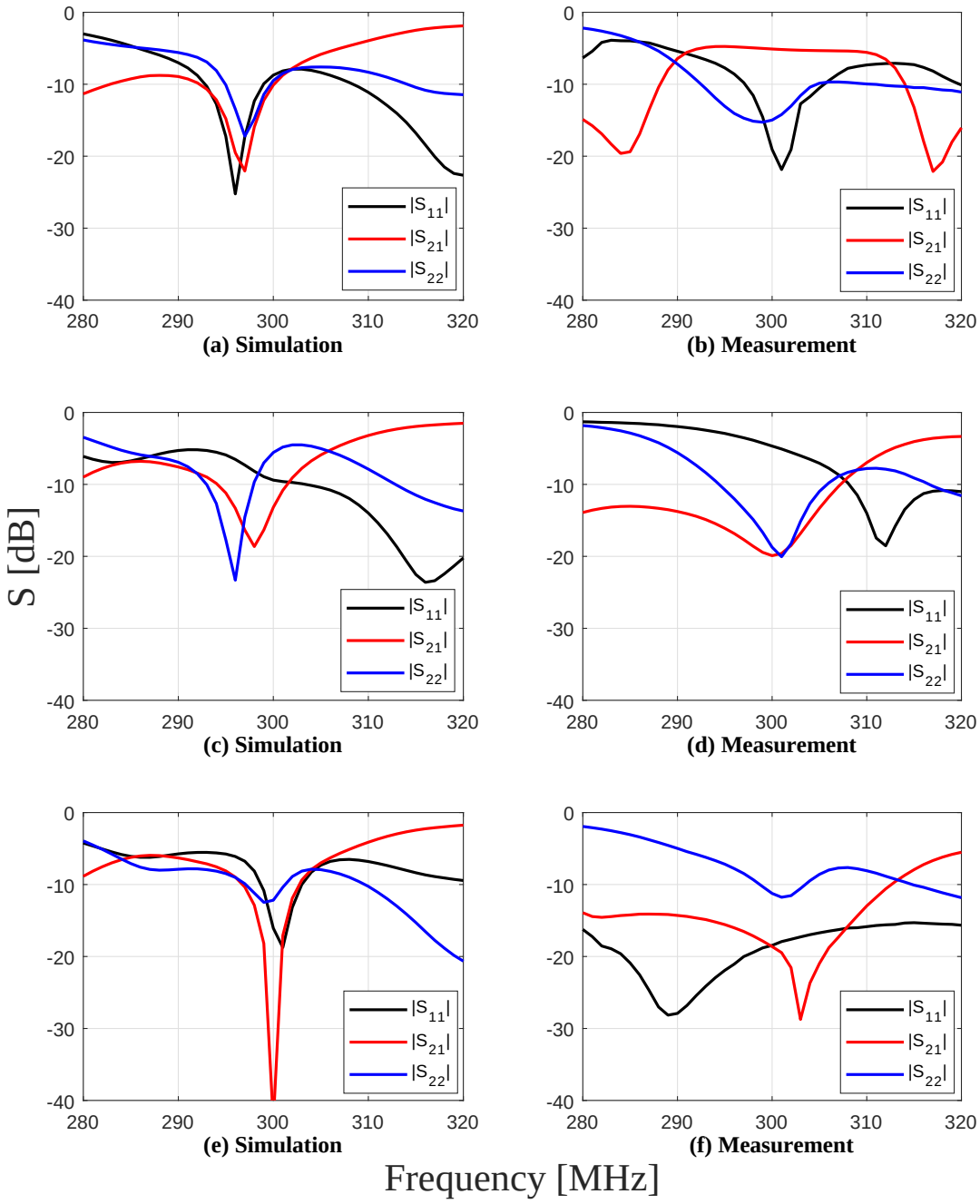

Figure 5.8: Simulated and measured S-parameters of the adaptive matching system in different conditions. (a-b) Original state first matched and decoupled. (c-d) Environment changes. (e-f) Matched and decoupled after tuning.

error of the impedance sensing unit, the accuracy of the phase/gain detector is 0.5 dB and 1°, any value smaller than these will be nonlinear and not accurate. Additionally, the short transmission line sections that connect the lumped elements of the coupling networks and the voltage dividers were not fully considered in calculating the elements' values. Besides, the digital capacitor is optimized for shunt configuration, when it is used in series configuration (C2 and C5), the value will be slightly different due to its equivalent circuit model. Despite these frequency shifts and slightly mismatch, the measured results agree well with the predicted results in the simulations.

5.5 Conclusions

In this chapter, we present a new method for designing adaptive matching and decoupling networks for a two-element antenna array. The proposed adaptive matching and decoupling network includes an impedance sensing system, a tunable matching network and a fixed decoupling network. The impedance sensing subsystem tracks the antenna impedance variations. The tunable matching network changes and adapts the element values to convert the the input impedance of each antenna port to the same fixed impedance at a single frequency. This way, a fixed impedance matching and decoupling network can be used to match the overall system impedance to 50 Ω and decouple the two antenna ports. A topology of the adaptive MDN was simulated and fabricated with the two-element asymmetric antenna array. The performance of the system was evaluated by both simulations and measurements. Measurement results confirmed the results obtained from simulations and verified the validity of the proposed synthesis technique.

Chapter 6

Summary and Future Work

6.1 Summary

In this dissertation, we discuss array decoupling and self-interference reduction technique that are particularly relevant to low-frequency RF and microwave applications. These include developing simultaneous transmit and receive antennas and external decoupling networks.

In the designing of simultaneous transmit and receive antennas, the goal was to sign a compact and low-profile STAR antenna with a monopole-like radiation characteristics. The proposed STAR antenna in this dissertation consists of transmit (TX) and a receive (RX) antennas whose phase centers are collocated. The STAR antenna was designed for operation in the 2.45 GHz ISM band with electrical dimensions of $D \times H = 0.44\lambda \times 0.15\lambda$ (diameter $\times$ height). The theoretical analysis and experiments show that this STAR antenna produce an omnidirectional radiation pattern and high isolation level better than 38dB between the two ports.

For developing external decoupling networks, the first two goals were to propose analytic techniques for synthesizing the decoupling and matching networks for two- and three- element antenna arrays. The procedure we proposed starts with determining the S-matrix of the DMN. Subsequently, we identify lumped-element networks implementation and present an analytic method for determining their element values from the DMNs' S-matrix. The performance of the networks were evaluated by both simulations and measurements and verified the validity of the proposed synthesis techniques.

The third goal was to design an adaptive matching and decoupling network (MDN) for a two-element antenna array. The proposed adaptive matching and decoupling network includes a tunable matching network and a fixed decoupling network. The tunable matching network sub-system tracks the antenna impedance variations, and changes and adapts its elements' values. Then, the input impedance of each antenna port remains to the same fixed impedance at a single frequency. Afterwards, a fixed DMN can be used to match the overall system impedance to 50 Ω and decouple the two antenna ports. Such a system

can successfully perform the tasks of impedance matching and decoupling of a two-element antenna system over a narrow bandwidth.

6.2 Future Research Directions

We conclude this thesis by suggesting some future research directions.

Finish the implementation of the DMN for linear three-element antenna array. Although we have discussed a method to decouple the linear three-element antenna array, but the proposed method only show in simulation and the network topology presented is not ready to fabricate. A comprehensive and better performed fabrication process still need to be developed based on our approach.

Design a wide-band or dual-band decoupling network. At this stage, we synthesize the decoupling network at the center frequency. The impedance matching and isolation is over a narrow bandwidth. Expand our approach to a wideband or dual-band decoupling network with a improved performance is desirable and can find more applications in the wireless communication systems.

Appendices

Appendix A

The detailed steps for calculating the remaining four scattering parameters (S_{13}, S_{14}, S_{33}, and S_{34}) of the DMN are presented. Using the lossless condition of the network ($[S][S^H] = [I]$), we have:

$$S_{11}S_{12}^* + S_{12}S_{11}^* + S_{13}S_{14}^* + S_{14}S_{13}^* = 0, \tag{A.1}$$

$$S_{13}S_{14}^* + S_{14}S_{13}^* + S_{33}S_{34}^* + S_{34}S_{33}^* = 0, \tag{A.2}$$

$$S_{11}S_{13}^* + S_{12}S_{14}^* + S_{13}S_{33}^* + S_{14}S_{34}^* = 0, \tag{A.3}$$

$$S_{11}S_{14}^* + S_{12}S_{13}^* + S_{13}S_{34}^* + S_{14}S_{33}^* = 0, \tag{A.4}$$

$$|S_{11}|^2 + |S_{12}|^2 + |S_{13}|^2 + |S_{14}|^2 = 1, \tag{A.5}$$

$$|S_{13}|^2 + |S_{14}|^2 + |S_{33}|^2 + |S_{34}|^2 = 1. \tag{A.6}$$

The left sides of equations (A.1), (A.2), (A.5), and (A.6) only contain the real parts of the S-parameters while the left sides of equations (A.3) and (A.4) include both the real and the imaginary parts of the associated S-parameters. Therefore, equations (A.1)-(A.6) appear to provide eight equations relating the remaining unknown S-parameters. However, further examination of this system of eight non-linear equations reveals that the eight equations are not independent. We found that six out of these eight equations should be chosen and used along with two additional equations (e.g, equations (A.11) and (A.13)), which will be introduced later, in order to solve for the S-parameters of the DMN. For example, six equations including (A.1), (A.2), (A.5), and (A.6), and the real parts of the left-hand sides

of (A.3) and (A.4) being equal to 0 were chosen for solving the S-parameters of the DMNs in Sections II, III, and IV.

Afterwards, we can calculate the output voltages in the common and different modes (V_{oc} and V_{od}, respectively) using the following equations (the voltages are assumed to be RMS):

$$V_{oc} = \frac{\sqrt{Z_0}(S_{13} + S_{14})(Z_{in,c} + Z_0)}{\sqrt{Z_0 R_{in,c}}}, \tag{A.7}$$

$$V_{od} = \frac{\sqrt{Z_0}(S_{13} - S_{14})(Z_{in,d} + Z_0)}{\sqrt{Z_0 R_{in,d}}}, \tag{A.8}$$

where, $R_{in,c}$ and $R_{in,d}$ are the real part of $Z_{in,c}$ and $Z_{in,d}$, respectively. Thus, the added condition for the phase difference of the output voltages in the common and differential modes can be expressed as:

$$|\angle V_{oc} - \angle V_{od}| = 90^\circ. \tag{A.9}$$

Equations (A.1)-(A.6) and (A.9) yield seven independent equations for solving the eight unknowns (the real and imaginary parts of S_{13}, S_{14}, S_{33}, and S_{34}). Therefore, in order to have a solution for the eight unknowns, we need to add another constraint to provide another independent equation relating the unknown scattering parameters. In section IV, we mentioned two different conditions for this added constraint that result in two different S-matrices. The first S-matrix was calculated by adding the constraint that $\angle S_{21} = 90^\circ$ in the common mode. We can calculate the input voltage ($V_{in,c}$) in the common mode by:

$$V_{in,c} = \frac{\sqrt{Z_0}(1 + S_{11} + S_{12})(Z_{in,c} + Z_0)}{\sqrt{Z_0 R_{in,c}}}. \tag{A.10}$$

Thus, the added constraint for S-matrix 1 can be written as:

$$|\angle V_{oc} - \angle V_{in,c}| = 90^\circ. \tag{A.11}$$

The second constraint was determined by minimizing the variance of the absolute value of the derivative of the output reactances in the differential mode with respect to frequency from 605 to 615 MHz. First, we fitted frequency-dependent impedances of the two-element antenna array to fourth-order polynomial functions over the frequency range from 500 to 700 MHz. Using the fitted polynomials, we can derive the functions of the output impedance seen at the output of the equivalent circuit of the antenna array with the DMN in the differential mode (see Fig. 3.5(b)) with respect to frequency:

$$Z_{out,d} = \frac{Z'_{22} - Z'_{12}Z'_{21}}{Z'_{11} + Z_d}, \tag{A.12}$$

where Z'_{11}, Z'_{12}, Z'_{21} and Z'_{22} are the Z-parameters of the equivalent circuit of the DMN in the differential mode, which are derived from the S-matrix. Z_d is the impedance of the two-element antenna array in the differential mode and is equal to Z_{11} - Z_{12} from (2). Therefore the added constraint for calculating S-matrix 2 can be expressed as:

$$g = \min\left(\frac{\int_{f_1=605}^{f_2=615}\left(\left|\frac{d(X_{out,d})}{df}\right| - \left|\overline{\frac{d(X_{out,d})}{df}}\right|\right)^2 df}{f_2 - f_1}\right), \tag{A.13}$$

where $X_{out,d}$ is the output reactance of the equivalent circuit model of the antenna array with the DMN in the differential mode and f represents the frequency (in MHz).

Appendix B

Justification of Rule 1

We will illustrate this rule by examining a counter example where we choose positions 2 and 8 without choosing 1 or 10. For the example, we consider the network with elements in positions 2, 3, 4, 6, 7, and 8. The equivalent circuit of the network in the common mode, with the transmission matrix $[T_{comm}]$, contains elements 3, 4, 6, and 7. The transmission

matrix for the network in the differential mode can be expressed as:

$$\begin{aligned}[T_{diff}] &= [T_2] \times [T_{comm}] \times [T_8] \\ &= \begin{bmatrix} 1 & 0 \\ Y_2 & 1 \end{bmatrix} \times \begin{bmatrix} A & B \\ C & D \end{bmatrix} \times \begin{bmatrix} 1 & 0 \\ Y_8 & 1 \end{bmatrix} \\ &= \begin{bmatrix} A + BY_8 & B \\ AY_2 + C + BY_2Y_8 + DY_8 & BY_2 + D \end{bmatrix},\end{aligned} \tag{B.1}$$

where $[T_2]$ and $[T_8]$ are the transmission matrices for elements 2 and 8, respectively and Y_2 and Y_8 are the admittances for elements 2 and 8, respectively. We can see that $[T_{comm}(1,2)]$ is the same as $[T_{diff}(1,2)]$, imposing a specific constraint that generally cannot be satisfied by the transmission matrices derived from the predetermined S-matrix.

Justification of Rule 2

We begin with an assumption that we pick only one position from 2, 5, and 8. We denote this element by the letter X for convenience. We separate the differential-mode circuit of the network into three cascaded parts with the corresponding transmission matrices of $[T_1]$, $[T]$, and $[T_2]$. $[T]$ is the transmission matrix of the element X (with admittance value of Y), while $[T_1]$ and $[T_2]$ are the transmission matrices of the parts on the left- and right-hand sides of this element, respectively. The total transmission matrix of the network in the differential mode is:

$$[T_{diff}] = [T_1] \times [T] \times [T_2] = \begin{bmatrix} A_1 & B_1 \\ C_1 & D_1 \end{bmatrix} \times \begin{bmatrix} 1 & 0 \\ Y & 1 \end{bmatrix} \times \begin{bmatrix} A_2 & B_2 \\ C_2 & D_2 \end{bmatrix}. \tag{B.2}$$

In the common mode, element X is absent and the transmission matrix of the network is written as:

$$[T_{comm}] = [T_1] \times [T_2] = \begin{bmatrix} A_1 & B_1 \\ C_1 & D_1 \end{bmatrix} \times \begin{bmatrix} A_2 & B_2 \\ C_2 & D_2 \end{bmatrix}. \tag{B.3}$$

The difference between the two transmission matrices is:

$$[T_{diff}] - [T_{comm}] = [Y] \begin{bmatrix} B_1A_2 & B_1D_2 \\ D_1A_2 & D_1D_2 \end{bmatrix}. \tag{B.4}$$

If we want to have analytic solutions for the reactive elements of the network, (B.4) must be satisfied. This mandates that the ratio of the two elements in the first column equals that of the two elements in the second column. It will introduce a specific constraint that the given S-matrix cannot satisfy. Therefore, we need to pick at least two positions from position 2, 5, and 8 to avoid this situation.

Justification of Rule 3

This rule is quite obvious, since two series/parallel reactance can be combined and treated as one single reactive element. This rule ensures that the six elements we pick are separate and independent.

Justification of Rule 4

An example of picking positions 1, 4, 7, and 10 is shown that the equivalent circuit of the network in the common mode must include a section that is a π network or T network. The transmission matrix of the network in the common mode will be:

$$[T_{comm}] = \begin{bmatrix} 1 & Z_{1,4,7,10} \\ 0 & 1 \end{bmatrix}, \tag{B.5}$$

where $Z_{1,4,7,10}$ is the total impedance of the four series elements. This transmission matrix will not match the one transferred from the given S-matrix in the common mode. Besides, if the differential-mode network is an L-network, e.g, for the case where we pick positions 1,

4, 7, and 9, the transmission matrix in the common mode will have the following form:

$$[T_{comm}] = \begin{bmatrix} 1 & Z_{1,4,7} \\ 0 & 1 \end{bmatrix} \times \begin{bmatrix} 1 & 0 \\ Y_9 & 1 \end{bmatrix} = \begin{bmatrix} 1+ZY & Z \\ Y & 1 \end{bmatrix}, \tag{B.6}$$

where $Z_{1,4,7}$ is the total impedance of three series elements 1, 4, and 7 and Y_9 is the admittance of the shunt element 9. Again, $[T_{comm}(2,2)]$ is equal to 1, resulting in no solutions for element values to match the parameters of the transmission matrix derived from the predetermined S-matrix.

Justification of Rule 5

If either position 8 or 9 is picked without position 7, it can be combined with position 5 or 6, respectively, to act as a single element. As a result, the network topology in such case is not unique. For example, it is the same as a network composed from 5 and/or 6 as a replacement for 8 and/or 9. Additionally, if we choose position 10 without choosing positions 8 and 9, position 10 will behave as position 7. This also does not guarantee the uniqueness of the network topology of these choices.

Appendix C

To demonstrate the detailed procedure for calculating the reactive element values of the coupling DMN, we take Topology 12 as an example as in Section 3.3. We can calculate the transmission matrices for both modes of excitation using the equivalent circuit models shown in Fig. 3.5. The transmission matrices in the common and differential modes are:

$$\begin{aligned} [T_{comm}] &= [T_1] \times [T_4] \times [T_6] \times [T_7] \\ &= \left[\begin{smallmatrix} 1 & jX_1 \\ 0 & 1 \end{smallmatrix}\right] \times \left[\begin{smallmatrix} 1 & jX_4 \\ 0 & 1 \end{smallmatrix}\right] \times \left[\begin{smallmatrix} 1 & 0 \\ 1/(jX_6) & 1 \end{smallmatrix}\right] \times \left[\begin{smallmatrix} 1 & jX_7 \\ 0 & 1 \end{smallmatrix}\right], \end{aligned} \tag{C.1}$$

$$
\begin{aligned}
[T_{diff}] &= [T_1] \times [T_2] \times [T_4] \times [T_6] \times [T_7] \times [T_8] \\
&= \left[\begin{smallmatrix} 1 & jX_1 \\ 0 & 1 \end{smallmatrix}\right] \times \left[\begin{smallmatrix} 1 & 0 \\ 2/(jX_2) & 1 \end{smallmatrix}\right] \times \left[\begin{smallmatrix} 1 & jX_4 \\ 0 & 1 \end{smallmatrix}\right] \\
&\times \left[\begin{smallmatrix} 1 & 0 \\ 1/(jX_6) & 1 \end{smallmatrix}\right] \times \left[\begin{smallmatrix} 1 & jX_7 \\ 0 & 1 \end{smallmatrix}\right] \times \left[\begin{smallmatrix} 1 & 0 \\ 2/(jX_8) & 1 \end{smallmatrix}\right],
\end{aligned} \tag{C.2}
$$

where $[T_1]$, $[T_2]$, $[T_4]$, $[T_6]$, $[T_7]$, and $[T_8]$ are the transmission matrices for components 1, 2, 4, 6, 7, and 8, respectively. Subsequently, we equate the transmission matrices shown in (C.1) and (C.2) to the ones shown in (3.13) and (3.14):

$$[T_{comm}] = [ABCD_{comm}], \tag{C.3}$$

$$[T_{diff}] = [ABCD_{diff}]. \tag{C.4}$$

Each equation system of (C.3) and (C.4) generates four equations for matching the elements of the two corresponding 2×2 matrices. We can solve the reactance values for the DMN (X_1, X_2, X_4, X_6, X_7 and X_8) by picking six (out of eight) equations:

$$jX_1 + jX_4 + jX_7[(\frac{X_1 + X_4}{X_6}) + 1] = -j58.190, \tag{C.5}$$

$$-\frac{j}{X_6} = -j0.0172, \tag{C.6}$$

$$\frac{X_7}{X_6} + 1 = 0.256, \tag{C.7}$$

$$jX_1 + jX_7[\frac{2X_1}{X_2} + \frac{X_1 + X_4(\frac{2X_1}{X_2} + 1)}{X_6} + 1] + jX_4(\frac{2X_1}{X_2} + 1) = j44.170, \tag{C.8}$$

$$-\frac{2j}{X_8}[\frac{2X_4}{X_2} + \frac{2X_7}{X_2} + \frac{X_7}{X_6}(\frac{2X_4}{X_2} + 1) + 1] - \frac{2j}{X_2} - \frac{j(\frac{2X_4}{X_2} + 1)}{X_6} = -j0.025, \tag{C.9}$$

$$\frac{2X_4}{X_2} - \frac{2X_7}{X_2} - \frac{X_7}{X_6}(\frac{2X_4}{X_2} + 1) + 1 = 4.659. \tag{C.10}$$

Appendix D

The detailed steps for calculating the remaining four scattering parameters (S_{13}, S_{14}, S_{33}, and S_{34}) of the DMN are presented. Using the lossless condition of the network ($[S][S]^H = [I]$), we have:

$$S_{11}S_{12}^* + S_{12}S_{11}^* + |S_{12}|^2 + S_{14}S_{15}^* + S_{15}S_{14}^* + |S_{15}|^2 = 0, \tag{D.1}$$

$$S_{14}S_{15}^* + S_{15}S_{14}^* + |S_{15}|^2 + S_{44}S_{45}^* + S_{45}S_{44}^* + |S_{45}|^2 = 0 \tag{D.2}$$

$$S_{11}S_{14}^* + 2S_{12}S_{15}^* + S_{14}S_{44}^* + 2S_{15}S_{45}^* = 0, \tag{D.3}$$

$$S_{11}S_{15}^* + S_{12}S_{14}^* + S_{12}S_{15}^* + S_{14}S_{45}^* + S_{15}S_{44}^* + S_{15}S_{45}^* = 0, \tag{D.4}$$

$$|S_{11}|^2 + 2|S_{12}|^2 + |S_{14}|^2 + 2|S_{15}|^2 = 1, \tag{D.5}$$

$$|S_{14}|^2 + 2|S_{15}|^2 + |S_{44}|^2 + 2|S_{45}|^2 = 1. \tag{D.6}$$

The left sides of equations (D.1), (D.2), (D.5), and (D.6) only contain the real parts of the S-parameters while the left sides of equations (D.3) and (D.4) include both the real and the imaginary parts of the associated S-parameters. Therefore, equations (D.1)-(D.6) appear to provide eight equations relating the remaining unknown S-parameters. However, further examination of this system of eight non-linear equations reveals that the eight equations are not independent. We found that seven out of these eight equations should be chosen and used along with one additional equation (e.g, equations (D.9)), which will be introduced later, in order to solve for the S-parameters of the DMN. For example, seven equations including (D.1), (D.2), (D.3), (D.5), (D.6), and the real parts of the left-hand sides of (D.4) being equal to 0 were chosen for solving the S-parameters of the DMN.

Afterwards, we we introduce an additional condition that the output voltages in Modes A and B (V_{oa} and V_{ob}) have a 45° phase difference. The voltages can be calculated using the following equations (the voltages are assumed to be RMS):

$$V_{oa} = \frac{\sqrt{Z_0}(S_{14} + 2S_{15})(Z_{in,a} + Z_0)}{\sqrt{Z_0 R_{in,a}}}, \tag{D.7}$$

$$V_{ob} = \frac{\sqrt{Z_0}(S_{14} - S_{15})(Z_{in,d} + Z_0)}{\sqrt{Z_0 R_{in,b}}}, \tag{D.8}$$

where, $R_{in,a}$ and $R_{in,b}$ are the real parts of $Z_{in,a}$ and $Z_{in,b}$, respectively. Thus, the additional condition can be expressed as:

$$|\angle V_{oa} - \angle V_{ob}| = 45°. \tag{D.9}$$

Appendix E

To demonstrate the detailed procedure for calculating the reactive elements values of the decoupling network, we take Topology 2 as an example as in Section 4.2.3. We can calculate the transmission matrices for Mode A and Mode B using the equivalent circuit models shown in Fig. 4.6 with the consideration of the connecting transmission lines. The dielectric constant of the board is $\epsilon_r = 4.4$ and the height of the board is 0.6 mm. The effective wavelength is 238.37 mm at 600 MHz. The equivalent series inductance and the shunt capacitance of the transmission lines are calculated by using the microstrip lines model. The inductance is $L = 0.5945$ nH per millimeter and the capacitance is $C = 0.05412$ pF per millimeter. Thus the impedance of the inductor and the admittance of the capacitor can be calculated by :

$$\begin{aligned} Z_L &= j \times 2\pi \times \text{freq} \times \text{L} = \text{j} \times 2\pi \times 600 \times 10^6 \times 0.5945 \times 10^{-9} = \text{j}2.24\ \Omega, \\ Y_C &= j \times 2\pi \times \text{freq} \times \text{C} = \text{j} \times 2\pi \times 600 \times 10^6 \times 0.05412 \times 10^{-12} = \text{j}2.04 \times 10^{-4}\ \text{S}. \end{aligned} \tag{E.1}$$

For l_1, the characteristics impedance is 100 Ω and the length is 6 mm, we treat the transmission line as a two-port network and calculate its transmission matrix $L1$ as:

$$\begin{aligned} [L1] &= \begin{bmatrix} \cos(\beta l) & jZ_0 \sin(\beta l) \\ jY_0 \sin(\beta l) & \cos(\beta l) \end{bmatrix} \\ &= \begin{bmatrix} \cos(12\pi/233.13 & j100 \times \sin(12\pi/233.13) \\ j/100 \times \sin(12\pi/233.13) & \cos(12\pi/233.13) \end{bmatrix}. \end{aligned} \tag{E.2}$$

For the other transmission lines, we consider that the series inductor and shunt capacitor are connected directly to the lumped elements. The transmission matrices for components 1, 2, 3, 4, 5, and 7 are calculated as $[T_1]$, $[T_2]$, $[T_3]$, $[T_4]$, $[T_5]$, and $[T_7]$, respectively.

The short transmission line connecting component 1 is 2 mm, the transmission matrix is:

$$[T_1] = \begin{bmatrix} 1 & jX1 + 2Z_L \\ 0 & 1 \end{bmatrix} \times \begin{bmatrix} 1 & 0 \\ 2Y_C & 1 \end{bmatrix}. \tag{E.3}$$

The transmission lines connecting component 2 shown as l_2 is 10.76 mm each side, thus the transmission matrix is:

$$[T_2] = \begin{bmatrix} 1 & 0 \\ 2Y_C \times 10.76 + 3/(2Z_L \times 10.76 + jX2) & 1 \end{bmatrix}. \tag{E.4}$$

The short transmission line connecting component 3 is 2 mm each side, the transmission matrix is:

$$[T_3] = \begin{bmatrix} 1 & 0 \\ 1/(4Z_l + jX3) & 1 \end{bmatrix} \times \begin{bmatrix} 1 & 0 \\ 2Y_C & 1 \end{bmatrix}. \tag{E.5}$$

The short transmission line connecting component 4 are 2 mm and 3 mm for two different sides, the transmission matrix is:

$$[T_4] = \begin{bmatrix} 1 & 0 \\ 2Y_C & 1 \end{bmatrix} \times \begin{bmatrix} 1 & jX4 + 5Z_L \\ 0 & 1 \end{bmatrix} \times \begin{bmatrix} 1 & 0 \\ 3Y_C & 1 \end{bmatrix}. \tag{E.6}$$

The transmission lines connecting component 2 shown as l_3 is 6.43 mm each side, thus the transmission matrix is:

$$[T_5] = \begin{bmatrix} 1 & 0 \\ 2Y_C \times 6.43 + 3/(2Z_L \times 6.43 + jX5) & 1 \end{bmatrix}. \tag{E.7}$$

The short transmission line connecting component 7 is 2 mm each side, the transmission

matrix is:

$$[T_7] = \begin{bmatrix} 1 & 0 \\ 4Y_C & 1 \end{bmatrix} \times \begin{bmatrix} 1 & jX7 + 4Z_L \\ 0 & 1 \end{bmatrix}. \tag{E.8}$$

The total transmission matrices in the Mode A and B are:

$$\begin{aligned} [T_{mode,A}] &= [T_1] \times [T_3] \times [T_4] \times [T_7], \\ [T_{mode,B}] &= [T_1] \times [T_{2]} \times [T_3] \times [T_4] \times [T_5] \times [T_7] \end{aligned} \tag{E.9}$$

Subsequently, we equate the transmission matrices shown in (E.9) to the ones shown in (4.15) and (4.16):

$$[T_{comm}] = [ABCD_{comm}], \tag{E.10}$$

$$[T_{diff}] = [ABCD_{diff}]. \tag{E.11}$$

Each equation system of (E.10) and (E.11) generates four equations for matching the elements of the two corresponding 2×2 matrices. We can solve the reactance values for the coupling networks (X_1, X_2, X_3, X_4, X_5 and X_7) by picking six (out of eight) equations.

Appendix F

To demonstrate the detailed procedure for calculating the values of the digitally tuned capacitors, we expressed the transmission matrix of the changed antenna system before the adaptive matching network as:

$$[T_{new}] = \begin{bmatrix} A & B \\ C & D \end{bmatrix}. \tag{F.1}$$

which the transmission matrix is calculated by the previous impedance sensing system. The adaptive matching network was designed to convert the the input impedance of the new

system to the same fixed input impedance Z_{11} and Z_{22} at 300 MHz as shown in (5.8). The impedance matrix after the adaptive matching network can be transformed from its transmission matrix. The transmission matrix can be expressed by combining the transmission matrix T in (F.1) and the two transmission matrices of the tunable matching network as shown in Fig. 5.6. The transmission matrices of the networks can be written as functions of six digitally tuned capacitors reactive values with the two series inductors. The transmission matrices of parallel capacitors C1, C2, C4, and C5 can be written as:

$$[T_{1,2,4,5}] = \begin{bmatrix} 1 & 0 \\ 1/(jX_{1,2,4,5}) & 1 \end{bmatrix}. \tag{F.2}$$

where $X_{1,2,4,5}$ are the reactance values of the capacitors directly. The transmission matrices of the series capacitors C3 and C6 can be calculated by treating them as series inductors L1 shown in Fig. 5.4(a) as:

$$[T_{3,6}] = \begin{bmatrix} 1 & jX_{3,6} \\ 0 & 1 \end{bmatrix}, \tag{F.3}$$

where $X_{3,6}$ are reactance values of the equivalent inductors. Then, the new transmission matrix of the system before the fixed decoupling network can be expressed as:

$$[T_{total}] = [T_2] \times [T_3] \times [T_1] \times [T_{new}] \times [T_4] \times [T_6] \times [T_5]. \tag{F.4}$$

Subsequently, we transformed the new Z-matrix of the system from (5.14) as:

$$[Z_{new}] = \begin{bmatrix} Z_{11,new} & Z_{12,new} \\ Z_{21,new} & Z_{22,new} \end{bmatrix}. \tag{F.5}$$

In order to make the the input impedance to the same fixed values, we should have:

$$Z_{11,new} = 26.9227 - j58.9722\ \Omega,$$
$$Z_{22,new} = 26.9227 - j58.9722\ \Omega. \tag{F.6}$$

Both impedances have the real and the imaginary parts, which will lead to four different equations. However, we have six digitally tuned capacitors values as unknowns. The system can not be solved with more unknowns than equations. Thus, we pre-assigned the values of C3 and C6 from 1.88 pF to 14 pF by its discrete steps 0.391 pF and reduced the number of unknown capacitors to four. We solved these equations by using the equations and systems solver in MATLAB and this method will provide us with several sets of solutions of the other four capacitors. By comparing different solutions, we choose the one with minimum variation in $Z_{12,new}$ compared to the value of $8.1424 + j6.3115$ as shown in (5.8). The solution chosen will lead to a better performance in isolation between the two ports.

References

[1] H. E. King, "Mutual impendence of unequal length antennas in echelon", *IRE Trans. Antennas and Propagation*, vol. 5, no. 3, pp. 306−313, Jul 1957.

[2] M. Duarte, A. Sabharwal, V. Aggarwal, R. Jana, K. K. Ramakrishnan, C. W. Rice and N. K. Shankaranarayanan, "Design and characterization of a full-duplex multi-antenna system for WiFi network," *IEEE Transactions on Vehicular Technology*, vol. 63, issue. 3, pp. 1160−1177, November 2013.

[3] D. Bharadia, E. McMilin, and S. Katti, "Full duplex radios," *ACM SIGCOMM Conf.*, 2013, pp. 375−386.

[4] K. L. Scherer et al., "Simultaneous transmit and receive system architecture with four stages of cancellation," *IEEE Int. Symp. Antennas Propag. USNC/URSI Nat. Radio Sci. Meeting*, pp. 520−521, Jul. 2015.

[5] E. Everett, A. Sahai, and A. Sabharwal, "Passive self-interference suppression for full-duplex infrastructure nodes," *IEEE Trans. Wireless Commun.*, vol. 13, no. 2, pp. 680−694, Feb. 2014.

[6] A. Sahai, G. Patel, C. Dick, and A. Sabharwal, "On the impact of phase noise on active cancelation in wireless full-duplex," *IEEE Trans. Veh. Technol.*, vol. 62, no. 9, pp. 4494−4510, Nov. 2013.

[7] E. Ahmed, A. M. Eltawil, and A. Sabharwal, "Rate gain region and design tradeoffs for full-duplex wireless communications," *IEEE Trans. Wireless Commun.*, vol. 12, no. 7, pp. 3556−3565, Jul. 2013.

[8] H. Thomsen, D. M. Kim, P. Popovski, N. K. Pratas, and E. de Carvalho, "Full duplex emulation via spatial separation of half duplex nodes in a planar cellular network," *IEEE 17th Int. Workshop Signal Process. Adv. Wireless Commun.*, Jul. 2016, pp. 1−5.

[9] O. N. Alrabadi, A. D. Tatomirescu, M. B. Knudsen, P. Pelosi, and G. F. Pedersen, "Breaking the transmitterCreceiver isolation barrier in mobile handsets with spatial duplexing," *IEEE Trans. Antennas Propag.*, vol. 61, no. 4, pp. 2241−2251, Apr. 2013.

[10] J. Wu, Y. J. Cheng, and Y. Fan, "Wide-band dual-polarized planar array antenna

for K/Ka-band wireless communication," *Microw. Opt. Technol. Lett.*, vol. 58, no. 10, pp. 2377−2381, Oct. 2016.

[11] H. Wong, K.−L. Lau, and K.−M. Luk, Design of dual-polarized L-probe patch antenna arrays with high isolation, *IEEE Trans. Antennas Propag.*, vol. 52, no. 1, pp. 45−52, Jan. 2004.

[12] S. Gao and A. Sambell, "Dual-polarized broad-band microstrip antennas fed by proximity coupling," *IEEE Trans. Antennas Propag.*, vol. 53, no. 1, pp. 526C530, Jan. 2005.

[13] Y. Li, Z. Zhang, W. Chen, Z. Feng, and M. F. Iskander, "A dualpolarization slot antenna using a compact CPW feeding structure," *IEEE Antennas Wireless Propag. Lett.*, vol. 9, pp. 191−194, 2010.

[14] S.−G. Zhou, G.−L. Huang, T.−H. Chio, J.−J. Yang, and G. Wei, "Design of a wide-band dual-polarization full-corporate waveguide feed antenna array," *IEEE Trans. Antennas Propag.*, vol. 63, no. 11, pp. 4775−4782, Nov. 2015.

[15] C. Kumar, V. V. Srinivasan, V. K. Lakshmeesha, and S. Pal, "Novel dual circularly polarized radiating element for spherical phasedarray application," *IEEE Antennas Wireless Propag. Lett.*, vol. 8, pp. 826−829, 2009.

[16] Y. Z. Shen, S.−G. Zhou, G.−L. Huang, and T.−H. Chio, "A compact dual circularly polarized microstrip patch array with interlaced sequentially rotated feed," *IEEE Trans. Antennas Propag.*, vol. 64, no. 11, pp. 4933−4936, Nov. 2016.

[17] D. S. Chandu and S. S. Karthikeyan, "A novel broadband dual circularly polarized microstrip-fed monopole antenna," *IEEE Trans. Antennas Propag.*, vol. 65, no. 3, pp. 1410−1415, Mar. 2017.

[18] J. Wu, Y. J. Cheng, H. B. Wang, Y. C. Zhong, D. Ma, and Y. Fan, "A wideband dual circularly polarized full-corporate waveguide array antenna fed by triple-resonant cavities," *IEEE Trans. Antennas Propag.*, vol. 65, no. 4, pp. 2135−2139, Apr. 2017.

[19] J. L. Young, R. S. Adams, B. ONeil, and C. M. Johnson, "Bandwidth optimization of

an integrated microstrip circulator and antenna assembly: Part 1," *IEEE Antennas Propag. Mag.*, vol. 48, no. 6, pp. 47−56, Dec. 2006.

[20] H. Dong, J. R. Smith, and J. L. Young, "A wide-band, high isolation UHF lumped-element ferrite circulator," *IEEE Microw. Wireless Compon. Lett.*, vol. 23, no. 6, pp. 294−296, Jun. 2013.

[21] S. Yang, D. Vincent, J. R. Bray, and L. Roy, "Study of a ferrite LTCC multifunctional circulator with integrated winding," *IEEE Trans. Compon., Packag., Manuf. Technol.*, vol. 5, no. 7, pp. 879−886, Jul. 2015.

[22] S. K. Cheung, T. P. Halloran, W. H. Weedon, and C. P. Caldwell, "MMIC-based quadrature hybrid quasi-circulators for simultaneous transmit and receive," *IEEE Trans. Microw. Theory Techn.*, vol. 58, no. 3, pp. 489−497, Mar. 2010.

[23] C.−H. Chang, Y.−T. Lo, and J.-F. Kiang, "A 30 GHz active quasicirculator with current-reuse technique in 0.18 m CMOS technology," *IEEE Microw. Wireless Compon. Lett.*, vol. 20, no. 12, pp. 693−695, Dec. 2010.

[24] D. Ghosh and G. Kumar, "A broadband active quasi circulator for UHF and L band applications," *IEEE Microw. Wireless Compon. Lett.*, vol. 26, no. 8, pp. 601−603, Aug. 2016.

[25] S. W. Y. Mung and W. S. Chan, "Active three-way circulator using transistor feedback network," *IEEE Microw. Wireless Compon. Lett.*, vol. 27, no. 5, pp. 476−478, May 2017.

[26] K. E. Kolodziej, P. T. Hurst, A. J. Fenn, and L. I. Parad, "Ring array antenna with optimized beamformer for simultaneous transmit and receive," in Proc. *IEEE Antennas Propag. Soc. Int. Symp.*, Jul. 2012, pp. 1−2.

[27] E. A. Etellisi, M. A. Elmansouri, and D. S. Filipovic, "Wideband simultaneous transmit and receive (STAR) antenna," *IEEE Trans. Antennas Propag.*, vol. 64, no. 1, pp. 6−15, Jan. 2016.

[28] E. Yetisir, C.−C. Chen, and J. L. Volakis, "Wideband low profile multiport antenna

with omnidirectional pattern and high isolation," *IEEE Trans. Antennas Propag.*, vol. 64, no. 9, pp. 3777−3786, Sep. 2016.

[29] M. A. Elmansouri, A. J. Kee, and D. S. Filipovic, "Wideband antenna array for simultaneous transmit and receive (STAR) applications," *IEEE Antennas Wireless Propag. Lett,* vol. 16, pp. 1277−1280, 2017.

[30] R. Lian, T.−Y. Shih, Y. Yin, and N. Behdad, "A high-isolation, UWB simultaneous transmit and receive antenna with monopole-like radiation characteristics," *IEEE Trans. Antennas Propag.*, vol. 66, no. 2, pp. 1002−1007, Feb. 2018

[31] J. Ha, M. A. Elmansouri, P. V. Prasannakumar, and D. S. Filipovic, "Monostatic co-polarized full-duplex antenna with left- of right-hand circular polarization," *IEEE Trans. Antennas Propag.*, vol. 65, no. 10, pp. 5103−5111, Oct. 2017.

[32] Z. Zhou, Y. Li, J. Hu, Y. He, Z. Zhang, and P.-Y. Chen, "Monostatic copolarized simultaneous transmit and receive (STAR) antenna by integrated single-layer design," *IEEE Antennas Wireless Propag. Lett.*, vol. 18, no. 3, pp. 472−476, Mar. 2019

[33] E. A. Etellisi, M. A. Elmansouri, and D. S. Filipovic, "Wideband multimode monostatic spiral antenna STAR subsystem," *IEEE Trans. Antennas Propag.*, vol. 65, no. 4, pp. 1845−1854, Apr. 2017.

[34] F. Yang and Y. Rahmat-Samii, "Microstrip antennas integrated with electromagnetic band-gap (EBG) structures: A low mutual coupling design for array applications," *IEEE Trans. Antennas Propag.*, vol. 51, no. 10, pp. 2936−2946, Oct. 2003.

[35] S. D. Assimonis, T. V. Yioultsis, and C. S. Antonopoulos, "Design and optimization of uniplanar EBG structures for low profile antenna applications and mutual coupling reduction," *IEEE Trans. Antennas Propag.*, vol. 60, no. 10, pp. 4944−4949, Oct. 2012.

[36] N. Kumar and U. K. Kommuri, "MIMO antenna mutual coupling reduction for wlan using spiro meander line UC-EBG," *Prog. Electromagn. Res.*, vol. 80, pp. 65−77, 2018.

[37] C.−Y. Chiu, C.H. Cheng, R. D. Murch, and C. R. Rowell, "Reduction of mutual coupling between closely-packed antenna elements," *IEEE Trans. Antennas Propag.*, vol.

55, no. 6, pp. 1732−1738, Jun. 2007.

[38] C. Kumar, M. I. Pasha, and D. Guha, "Defected ground structure integrated microstrip array antenna for improved radiation properties," *IEEE Antennas Wireless Propag. Lett.*, vol. 16, pp. 310−312, 2016.

[39] X.−J. Zou, G.−M. Wang, and Y.−W. Wang, "A novel combined structure for decoupling E/H-plane microstrip antenna array," *Int. J. RF Microw. Comput.-Aided Eng.*, vol. 28, no. 5, Jun. 2018, Art. no. e21244.

[40] H.−X. Xu, G.−M. Wang, M.−Q. Qi, and H.−-Y. Zeng, "Ultra-small singlenegative electric metamaterials for electromagnetic coupling reduction of microstrip antenna array," *Opt. Express,* vol. 20, no. 20, pp. 21968−21976, 2012.

[41] T. Cai, G.−M. Wang, J.−G. Liang, and Y.−Q. Zhuang, "Application of ultracompact single negative waveguide metamaterials for a low mutual coupling patch antenna array design," *Chin. Phys. Lett.*, vol. 31, no. 8, Aug. 2014, Art. no. 084101.

[42] S. Zhang and G. F. Pedersen, "Mutual coupling reduction for UWB MIMO antennas with a wideband neutralization line," *IEEE Antennas Wireless Propag. Lett.*, vol. 15, pp. 166−169, 2016.

[43] K.−L. Wu, C. Wei, X. Mei, and Z.−Y. Zhang, "Array-antenna decoupling surface," *IEEE Trans. Antennas Propag.*, vol. 65, no. 12, pp. 6728−6738, Dec. 2017.

[44] S.−C. Chen, Y.−S. Wang, and S.−J. Chung, "A decoupling technique for increasing the port isolation between two strongly coupled antennas," *IEEE Trans. Antennas Propag.*, vol. 56, no. 12, pp. 3650−3658, Dec. 2008.

[45] R.−L. Xia and S.−W. Qu, "A wideband wide-angle scanning 1-D microstrip patch array," *Proc. 11th Eur. Conf. Antennas Propag.*, Paris, France, Mar. 2017, pp. 1079−1082.

[46] L. Zhao and K.−L. Wu, "A broadband coupled resonator decoupling network for a three-element compact array," *Int. Microw. Symp. Dig.*, Seattle WA, USA, pp. 1−3, Jun. 2013.

[47] Y.−F. Cheng and K.−K. M. Cheng, "A novel and simple decoupling method for

a three-element antenna array," *IEEE Antennas Wireless Propag. Lett.*, vol. 16, pp. 1072−1075, 2017.

[48] J. B. Anderson and H. H. Rasmussen, "Decoupling and descattering networks for antennas," *IEEE Trans. Antennas Propag.*, vol. AP−24, no. 6, pp. 841−846, Nov. 1976.

[49] P. T. Chua and J. C. Coetzee, "Microstrip decoupling networks for low-order multi-port arrays with reduced element spacing," *Microw. Opt. Technol. Lett.*, vol. 46, no. 6, pp. 592−597, Sep. 2005.

[50] J. C. Coetzee and Y. Yu, "An alternative approach to decoupling of arrays with reduced element spacing," *ISAP 2006*, Singapore,Nov. 2006.

[51] C. Volmer, J. Weber, R. Stephan, K. Blau, and M. A. Hein, "Decoupling and matching network for miniaturised 3-port antenna arrays based on 180 couplers," *Int. ITG Conf.*, Munich, Germany, pp. 63−66, Mar. 2007.

[52] C. Volmer, J. Weber, R. Stephan, K. Blau, and M. A. Hein, "An eigenanalysis of compact antenna arrays and its application to port decoupling," *IEEE Trans. Antennas Propag.*, vol. 56, no. 2, pp. 360C370, Feb. 2008.

[53] J. C. Coetzee and Y. Yu, "Port decoupling for small arrays by means of an eigenmode feed network," *IEEE Trans. Antennas Propag.*, vol. 56, no. 6, pp. 1587−1593, Jun. 2008

[54] O. Sung−hoon, H. Song, J. T. Aberle, B. Bakkaloglu, and C. Chakrabarti, "Automatic antenna tuning unit for software-defined and cognitive radio," *IEEE Int. AP-S Symp.*, pp. 85−88, 2007.

[55] J. S. Fu, X. A. Zhu, J. D. Phillips, and A. Mortazawi, "A ferroelectricbased impedance tuner for adaptive matching applications," *IEEE MTT-S Int. Microw. Symp. Dig.*, pp. 955−958, 2008.

[56] K. B. deBrito andR. N. de Lima, b"Impedance network for an automatic impedance-matching system", *AsiaCPacificMicrow. Conf.*, pp. 1−4, 2007.

[57] J. de Mingo, A. Valdovinos, A. Crespo, D. Navarro, and P. Garcia, "An RF electronically controlled impedance tuning network design and its application to an antenna input

impedance automatic matching system," *IEEE Trans. Microw. Theory Techn.*, vol. 52, no. 2, pp. 489−497, Feb. 2004.

[58] A. Bezooijen, M.A. de Jongh, F. van Straten, R. Mahmoudi, and A. van Roermund, "Adaptive impedance matching techniques for controlling L-networks," *IEEE Trans. Circuits Syst. I, Reg. Papers*, vol. 57, no. 2, pp. 495−505, Feb. 2010.

[59] A. Sabharwal, P. Schniter, D. Guo, D. W. Bliss, S. Rangarajan, and R. Wichman, "In-band full-duplex wireless: challenges and opportunities," *IEEE J. Sel. Areas Commun.*, vol. 32, no. 9, pp. 1637−1652, Sep. 2014.

[60] J. I. Choi, M. Jain, K. Srinivasan, P. Levis, and S. Katti, "Achieving single channel full duplex wireless communication," *Proc. 2010 ACM MobiCom.*, pp. 1−12.

[61] R. Lian, Z. Wang, Y. Yin, J. Wu and X. Song, "Design of a low-profile dual-polarized stepped slot antenna array for base station," *IEEE Antennas Wireless Propag. Lett.*, vol. 15, pp. 362−365, 2016.

[62] H. Nawaz, I. Tekin, "Dual-polarized, differential fed microstrip patch antennas with very high interport isolation for full-duplex communication," *IEEE Trans. Antennas Propag.*, vol. 65, no. 12, pp. 7355−7360, Dec. 2017.

[63] A. T. Wegener, W. J. Chappell, "Simultaneous transmit and receive with a small planar array," *IEEE/MTT-S International Microwave Symposium Digest*, Montreal, QC, 2012, pp. 1−3.

[64] A. T. Wegener, "Broadband near-field filters for simultaneous transmit and receive in a small two-dimensional array," *IEEE MTT-S International Microwave Symposium (IMS2014)*, Tampa, FL, 2014, pp. 1−3.

[65] D. Wu, S. W. Cheung, Q. L. Li and T. I. Yuk, "Decoupling using diamond-shaped patterned ground resonator for small MIMO antennas," *IET Microwaves, Antennas Propag.*, vol. 11, no. 2, pp. 177−183, 2017.

[66] A. J. Fenn, P. T. Hurst, J. S. Herd, K. E. Kolodziej, L. I. Parad, and H. Steyskal, "Simultaneous transmit and receive antenna system," U.S.

[67] H. Yang, "A road to future broadband wireless access: MIMO-OFDM-based air interface," *IEEE Commun. Mag.*, vol. 43, no. 1, pp. 53−60, Jan 2005

[68] T. Svantesson and A. Ranheim, "Mutual coupling effects on the capacity of multi-element antenna systems," *Proc. IEEE Int. Conf. Acoustics, Speach, and Signal Processing (ICASSP01)*, vol. 4, pp. 2485−2488, May 2001.

[69] J. Weber, C. Volmer, K. Blau, R. Stephan, and M. A. Hein, "Miniaturized antenna arrays using decoupling networks with realistic elements," *IEEE Trans. Microw. Theory Tech.*, vol. 54, no. 6, pp. 2733−2740, Jun 2006.

[70] C. Volmer, M. Sengul, J. Weber, R. Stephan, and M. A. Hein, "Broadband decoupling and matching of a superdirective two-port antenna array," *IEEE Antennas Wireless Propag. Lett.*, vol. 7, pp. 613−616, 2008.

[71] J. Winters, "On the capacity of radio communication systems with diversity in a rayleigh fading environment," *IEEE J. Sel. Areas Commun.*, vol. 5, no. 5, pp. 871−878, Jun 1995.

[72] J. W. Wallace and M. A. Jensen, "Mutual coupling in mimo wireless systems: A rigorous network theory analysis," *IEEE Trans. Wireless Commun.*, vol. 3, no. 4, pp. 1317−1325, Jul 2004.

[73] M. R. Nikkhah, M. A. Panahi, H. Luyen, H. Bahrami, and N. Behdad, "Capacity-enhancement in MIMO system using biomimetic electrically-small antenna arrays," *IET Microwaves, Antennas & Propagation*, vol. 12, no. 13, pp. 2001−2006, 2018.

[74] G. J. Foschini and M. J. Gans, "On limits of wireless communications in a fading environment when using multiple antennas," *Wireless Personal Commun.*, vol. 6, no. 3, pp. 311−335, Mar 1998.

[75] K. F. Warnick and M. A.Jensen, "Optimal noise matching for mutually coupled arrays," *IEEE Trans. Antennas Propag.*, vol. 55, no. 6, pp. 1726−1731, Jun 2007.

[76] N. Behdad, M. A. Al−Joumayly, and M. Li, "Biomimetic electrically small antennas," *Electron. Lett.*, vol. 46, no. 25, pp. 1650−1651, Dec 2010.

[77] N. Behdad, M. A. Al−Joumayly, and M. Li, "Biologically inspired electrically small antenna arrays with enhanced directional sensitivity," *IEEE Antennas Wireless Propag. Lett.*, vol. 10, pp. 361−364, 2011.

[78] P. Grüner, T. Chaloun, and C. Waldschmidt, "Towards a mm-wave planar biomimetic antenna array with enhanced phase sensitivitym," *IEEE 10th European Conference on Antennas and Propagation (EuCAP)*, pp. 1−5, 2016.

[79] A. M. Elfrgani and R. G. Rojas, "Biomimetic antenna array using non-Foster network to enhance directional sensitivity over broad frequency band," *IEEE Trans. Antennas Propag.*, vol. 64, no. 10, pp. 4297−4305, Oct. 2016.

[80] P. Grüner, T. Chaloun, and C. Waldschmidt, "A Generalized Model for Two-Element Biomimetic Antenna Array," *IEEE Trans. Antennas Propag.*, vol. 67, no. 3, pp. 1630−1639, Mar 2019.

[81] A. R. Masoumi, K. Ghaemi, and N. Behdad, "A two-element biomimetic antenna array with enhanced angular resolution and optimized power extraction," *IEEE Trans. Antennas Propag.*, vol. 63, no. 3, pp. 1059−1066, Mar 2015.

[82] D. Nie, B. M. Hochwald, and E. Stauffer, "Systematic design of large-scale multiport decoupling networks," *IEEE Trans. Circuits Syst. I*, vol. 61, no. 7, pp. 2172−2181, Jul 2014.

[83] J. C. Coetzee and Y. Yu, "Closed-form design equations for decoupling networks of small arrays," *Electron Lett.*, vol. 44, no. 25, pp. 1441-1442, Dec 2008.

[84] K. C. Lin, C. −H. Wu, C. −H. Lai, and T. −G. Ma, "Novel dual-band decoupling network for two-element closely spaced array using synthesized microstrip lines," *IEEE Trans. Antennas Propag.*, vol. 60, no. 11, pp. 5118−5128, Nov 2012.

[85] D. Youla, "Direct single frequency synthesis from a prescribed scattering matrix," *IRE Trans. Circuit Theory.*, vol. 6, no. 4, pp. 340−344, Dec 1959.

[86] A. Kummert, "Synthesis of two-dimensional losslessm-ports with prescribed scattering matrix," *Circuits, Syst., Signal Proces.*, vol. 8, no. 1, pp. 97−119, Mar 1989.

[87] D. M. Pozar, *Microwave Engineering, 4*th ed., New York, NY: Wiley, 2009.

[88] M. A. Jensen and J. W. Wallace, "Areview of antennas and propagation for MIMO wireless communications," *IEEE Trans. Antennas Propag.*, vol. 52, no. 11, pp. 2810−2824, Nov. 2004.

[89] C. Y. Chiu, C. H. Cheng, R. D. Murch, and C. R. Rowell, "Reduction of mutual coupling between closely-packed antenna element," *IEEE Trans. Antennas Propag.*, vol. 55, no. 6, pp. 1732−1738, Jun. 2007.

[90] H. Li, J. Xiong, and S. He, "Acompact planar MIMO antenna system of four elements with similar radiation characteristics and isolation structure," *IEEE Antennas Wireless Propag. Lett.*, vol. 8, pp. 1107−1110, 2009.

[91] L. K. Yeung and Y. E. Wang, "Mode-based beamforming arrays for miniaturized platforms," *IEEE Trans. Microw. Theory Tech.*, vol. 57, no. 1, pp. 45−52, Jan. 2009.

[92] J. C. Coetzee and Y. Yu, "New modal feed network for a compact monopole array with isolated ports," *IEEE Trans. Antennas Propag.*, vol. 56, no. 12, pp. 3872−3875, Dec. 2008.

[93] H. J. Chaloupka, X. Wang, and J. C. Coetzee, "A superdirective 3-element array for adaptive beamforming," *Microwave and Optical Technology Letters* vol. 36, no. 6, pp. 425−430, Mar. 2003.

[94] H.J. Chaloupka, X. Wang and J.C. Coetzee, "Performance enhancement of smart antennas with reduced element spacing," *Wireless Communications and Networking, IEEE Conf.*, vol. 1, pp. 425−430, Mar. 2003.

[95] J. W. Wallace and M. A. Jensen, "Termination-dependent diversity performance of coupled antennas: Network theory analysis", *IEEE Trans. Antennas Propagat.*, vol. 52, no. 1, pp. 98−105, Jan. 2004.

[96] D. A. Frickey, "Conversions between S, Z, Y, H, ABCD, and T parameters which are valid for complex source and load impedances, *IEEE Trans. Microw. Theory Techn.*, vol. 42, no. 2, pp. 205−211, February 1994.

[97] T. Reveyrand, "Multiport conversions between S, Z, Y, h, ABCD, and T parameters," *IEEE INMMIC*, pp. 1−3, Jul. 2018.

[98] H. W. Ott, Electromagnetic Compatibility Engineering. New York, NY, USA: Wiley, 2011.

[99] W. P. Kodali, Engineering Electromagnetic Compatibility. New York, NY, USA: Wiley, 2001.

[100] M. M. B. Suwailam, M. S. Boybay, and O. M. Ramahi, Mutual coupling reduction in MIMO antennas using artificial magnetic materials," *Proc. 13th Int. Symp. Antenna Technol. Appl. Electromagn. Can. Radio Sci. Meeting (ANTEM/URSI)*, Feb. 2009, pp. 1−4.

[101] L. Inclan-Sanchez, J.−L. Vaquez-Roy, and E. Rajo−Iglesias, "High isolation proximity coupled multilayer patch antenna for dualfrequency operation," *IEEE Trans. Antennas Propag.*, vol. 56, no. 4, pp. 1180−1183, Apr. 2008.

[102] X. Tang, K. Mouthaan, and J. C. Coetzee, "Flexible design of decoupling and matching networks for two strongly coupled antennas," *Electron. Lett.*, vol. 49, no. 8, pp. 521−522, Apr. 2013.

[103] C. H. Niow, Y. T. Yu, and H. T. Hui, "Compensate for the coupled radiation patterns of compact transmitting antenna arrays," *IET Microw., Antennas Propag.*, vol. 5, no. 6, pp. 699−704, Apr. 2011.

[104] S. C. Chen, Y. S. Wang, and S. J. Chung, "A decoupling technique for increasing the port isolation between two strongly coupled antennas," *IEEE Trans. Antennas Propag.*, vol. 56, no. 12, pp. 3650−3658, Dec. 2008

[105] L. Yang, M. Fan, F. Chen, J. She, and Z. Feng, "A novel compact electromagnetic-bandgap (EBG) structure and its applications for microwave circuits," *IEEE Trans. Microw. Theory Techn.*, vol. 53, no. 1, pp. 183−190, Jan. 2005.

[106] M. M. Bait−Suwailam, M. S. Boybay, and O. M. Ramahi, "Electromagnetic coupling reduction in high-profile monopole antennas using single-negative magnetic meta-

materials for MIMO applications," *IEEE Trans. Antennas Propag.*, vol. 58, no. 9, pp. 2894−2902, Sep. 2010.

[107] J. D. Fredrick, Y. Wang, and T. Itoh, "Smart antennas based on spatial multiplexing of local elements (SMILE) for mutual coupling reduction," *IEEE Trans. Antennas Propag.*, vol. 52, no. 1, pp. 106−114, Jan. 2004.

[108] K. B. deBrito, R. N. de Lima, "Impedance network for an automatic impedance-matching system", *AsiaCPacificMicrow. Conf.*, pp. 1−4, 2007.

[109] Y. Cai and Y. Jay Guo, "A reconfigurable decoupling and matching network for a frequency agile compact array",*Proceedings of the 5th European Conference on Antennas and Propagation (EUCAP)*, Rome, Italy, 2011, pp. 896−899.

[110] C. Wilson, J. Dean and B. A. Floyd, "Mixer-First MIMO Receiver With Reconfigurable Multi-Port Decoupling and Matching,"*IEEE Journal of Solid-State Circuits*, vol. 55, no. 5, pp. 1401−1410, May 2020.

[111] X. Tang, K. Mouthaan and J. C. Coetzee, "Tunable Decoupling and Matching Network for Diversity Enhancement of Closely Spaced Antennas," *IEEE Antennas and Wireless Propagation Letters*, vol. 11, pp. 268−271, 2012.

[112] Jia-Shiang Fu, X. A. Zhu, J. D. Phillips and A. Mortazawi, "A ferroelectric-based impedance tuner for adaptive matching applications,"*IEEE MTT-S International Microwave Symposium Digest*, Atlanta, GA, USA, 2008, pp. 955−958.